Navigating Earthquake Physics with High-Resolution Array Back-Projection

Thesis by

Lingsen Meng

In Partial Fulfillment of the Requirements for the Degree

of

Doctor of Philosophy

CALIFORNIA INSTITUTE OF TECHNOLOGY

Pasadena, California

2013

(Defended August 20, 2012)

ACKNOWLEDGEMENTS

First of all, I own my most sincere gratitude to Professor Jean-Paul Ampuero, who is not only an amazing advisor but also a true and valuable friend. I appreciate his encouragement when I feel frustrated on research, his excellent way of explaining complicated physics, his thorough and insightful advice on my thesis projects, and his accessibility whenever I needed his help. His guidance inspired my scientific thinking and showed me the path to become a real scientist. I consider myself very fortunate to be his first graduate student, and I am most grateful for the fruitful collaborations we have developed over the past years.

My gratitude also goes to the other faculty members in the Seismo Lab. I thank Rob Clayton and Jean-Philippe Avouac who turned me into a geophysicist during an amazing enrichment trip to Tien-Shan in 2006 where I first met Caltech GPS people. I thank my advisors of my oral propositions, Rob Clayton and Joann Stock, who helped and trained me through my first years at Seismo Lab. I thank my academic advisors, Rob Clayton and Jennifer Jackson who are always available for the issues I came up with. I appreciated the inspiring classes lead by Rob Clayton and Don Helmberger from whom I learned most of my seismology. I also want to thank Hiroo Kanamori, Jean-Philippe Avouac, Victor Tsai, Mark Simons, and Nadia Lapusta for their valuable discussions on my thesis research.

I have appreciated both my academic and social interactions with the current and previous graduate students and postdocs at Caltech. I am grateful to the other members in our research group, Asaf Inbal, Yingdi Luo, and Yihe Huang for the interesting discussions, exchanging research experience and the rewarding teamwork. I own my thanks to more senior Seismo Lab members, Dr. Carl Tape (his wife Elizabeth Nadin), Dr. Lijun Liu (his wife Yun Li), Dr. Daoyuan Sun, Dr. Younghee Kim, Dr. Yoshi Kaneko, Dr. Ravi Kanda, Dr. Sarah Minson, Dr. Enseo Choi, Dr. Chris DiCaprio, Dr.

Shengji Wei, Dr. Risheng Chu , Dr. Fanchi Lin, and Dr. Wenzheng Yang for their advice and help both with questions in my research and life around Caltech. Carl and Lijun set the standard of successful Caltech graduates that I will aim to emulate. I also enjoyed socializing with Dongzhou, Xi Zhang, Da Yang, Dan Bower, Caitlin Murphy, Laura Alisic, Nina Lin, Yu Wang, Ting Chen, Zhongwen Zhan, Nneka Williams, Francisco Ortega, Xiangyan Tian, Yiran Ma, Dunzhu Li, and many other students, and I cherish their friendship. I am thankful to the helpful and friendly staff, Julia Zuckerman, Viola Carter, Dian Buchness, and Donna Mireles, who has been heroes behind the success of every Seismo Lab researcher.

I thank Anthony Sladen, Herbert Redon, Wenbo Wu, Sidao Ni, Morgan Page, Ken Hudnut, and Zach Duputel who has been very dedicated and responsive during our collaborations. I also thank my colleagues working on earthquake source imaging, Miyaki Ishii, Alex Hukto, Huajian Yao, Peter Shearer, Thorne Lay, and Keith Koper who had very interesting discussions with me at various conferences.

Finally, I thank my dad Xiangshun, my mom Li and my lovely girlfriend Jingshu.

ABSTRACT

Understanding earthquake source dynamics is a fundamental goal of geophysics. Progress toward this goal has been slow due to the gap between state-of-art earthquake simulations and the limited source imaging techniques based on conventional low-frequency finite fault inversions. Seismic array processing is an alternative source imaging technique that employs the higher frequency content of the earthquakes and provides finer detail of the source process with few prior assumptions. While the back-projection provides key observations of previous large earthquakes, the standard beamforming back-projection suffers from low resolution and severe artifacts. This thesis introduces the MUSIC technique, a high-resolution array processing method that aims to narrow the gap between the seismic observations and earthquake simulations.

The MUSIC is a high-resolution method taking advantage of the higher order signal statistics. The method has not been widely used in seismology yet because of the nonstationary and incoherent nature of the seismic signal. We adapt MUSIC to transient seismic signal by incorporating the Multitaper cross-spectrum estimates. We also adopt a "reference window" strategy that mitigates the "swimming artifact," a systematic drift effect in back projection. The improved MUSIC back projections allow the imaging of recent large earthquakes in finer details which give rise to new perspectives on dynamic simulations. In the 2011 Tohoku-Oki earthquake, we observe frequency-dependent rupture behaviors which relate to the material variation along the dip of the subduction interface. In the 2012 off-Sumatra earthquake, we image the complicated ruptures involving orthogonal fault system and an usual branching direction. This result along with our complementary dynamic simulations probes the pressure-insensitive strength of the deep oceanic lithosphere. In another example, back projection is applied to the 2010 M7 Haiti earthquake recorded at regional distance. The high-frequency subevents are located at the edges of geodetic slip regions, which are

correlated to the stopping phases associated with rupture speed reduction when the earthquake arrests.

TABLE OF CONTENTS

LIST OF ILLUSTRATIONS

LIST OF TABLES

C h a p t e r 1

INTRODUCTION

Earthquakes are among the most important of the unsolved natural mysteries. The "abruptness" of earthquakes both in space and time makes it difficult to study them. The earthquake source refers to the shear slip on a fault which generates seismic waves. Understanding the earthquake source process is not only a fundamental physical problem but also is important for earthquake hazard assessment and other related fields such as structure of subduction zones, evolution of regional tectonics and rheology of the lithosphere.

The first effort to characterize the earthquake source with seismic observations started with Nakano in 1923. He used a simple exploration source to explain the observed seismic field. Since then the efforts in various disciplines have led to an unprecedented level of knowledge of earthquake physics. The techniques to do so comprise: laboratory experiments on rock samples, field surveys of paleoseismic events, study of historical reports and recordings, analysis of seismic record and geodetic measurement. The seismic approach is the most direct among them and the only one providing constraint on the dynamic rupture behavior. The standard technique to image the earthquake source is finite fault inversion, which represents the rupture history with the spatial and temporal slip distribution in a parametric model. Nowadays, finite fault models are done routinely to compute Coulomb stress changes, infer earthquake source physics and model ground motion. However, just like other inverse problems in geophysics, source inversions suffer from being ill-posed and underdetermined [*Ide et al.* 2009]. To reduce the non-uniqueness of the models, assumptions of the Green's function, fault geometry, rupture speed, and rise time have to be made, which often result in incomplete and partial results. Particularly, the requirement of deterministic Green's function

limits the approach to relatively low frequency (f < 0.1 Hz) in which the crustal structure is roughly known. On the other hand, theoretical earthquake source studies, especially dynamic simulations, have reached a high degree of sophistication, which is driven by the rapid development of the computational power and numerical methods. Earthquakes formerly simulated with conceptual and analytical models are now modeled with complicated constitutive laws, multiple fault planes, and 3D fault zone structures. The complex rupture patterns that emerge in these dynamic simulations, such as variable rupture speed, isolated rupture front, and frequency dependent behavior require finer details of the source process that hide in the high frequency (f > 1 Hz) contents hard to retrieve in conventional source inversions (figure 1.1).

Seismic array processing is an emerging technique to study the earthquake source [*Rost and Thomas* 2002]. Source imaging by back-tracing of seismic waves recorded by dense arrays allows us to track the areas of strongest high-frequency radiation (figure 1.3). This approach constrains the spatiotemporal properties of the rupture (length, direction, speed, segmentation) based solely on the phase of coherent seismic array signals. Thus, it does not rely on detailed knowledge of Green's functions and fault geometry, on restrictive parameterizations of the rupture kinematics, nor on additional smoothing. The high-frequency aspects imaged by array processing reveal finer details of the rupture process that are crucial to discriminate complicated physical models in theoretical earthquake source studies.

Over the last two decades, the development of large scale dense seismic networks have enabled progress in many fields of earth sciences, such as images of deep earth discontinuities, high resolution surface wave tomography, temporal velocity variations and site quantification for engineering purposes. These large-aperture arrays such as USArray, ORFEUS array (European network) and Hi-net (Japanese network) also permit fine imaging of large earthquakes based on relatively coher-

ent p-wave arrivals recorded at teleseismic distance. The approach explores the concept of "relative relocation" by aligning the waveforms with the initial p-arrival which is assumed to originate from the hypocenter. This "hypocenter alignment" minimizes the travel time errors due to 3d velocity structures. This particular version of seismic array processing is also referred as "back-projection", which was introduced by Ishii et al. (2005) for the 2004 Sumatra earthquake. It proves to provide robust imaging of the recent large earthquakes, such as the 2010 Chilean earthquake [*Kiser and Ishii* 2011; *Koper et al.* 2012], the 2011 Tohoku-Oki earthquake [*Meng et al.* 2011; *Zhang et al.* 2011] and the 2012 off-Sumatra earthquake [*Meng, Ampuero, Stock et al.* 2012; *Satriano et al.* 2012].

The standard processing of back projection is beamforming, which searches the maximum sum of recorded seismograms along different travel time curves of trial source locations. As intuitive as the method is, it suffers from low resolution especially when simultaneously emitting sources are present. On the other hand, since the array processing is used in a variety of military and civilian source tracking applications, many sophisticated techniques with high resolution have been proposed [*Krim et al.* 1998]. However, because these methods usually utilize higher order statistical estimates which require relatively coherent and stationary recordings, they are seldom applied to seismic signals that are transient and incoherent due to scattering in random earth media.

In this thesis, I successfully introduced a sophisticated MUlitiple SIgnal Classification (MUSIC) [*Schmidt et al.* 1982; *Therrien* 1992; *Chandran* 2006] algorithm into the back projection and improved its practical applicability to nonstationary seismic signals by incorporating the multitaper cross spectrum estimates (The principles of MUSIC are summarized in Appendix A.2). This technique provides superior resolution over the standard beamforming. By developing a "reference window" strategy, I have also modified the approach to mitigate the commonly seen "swimming

artifact". These improvements reveal finer details of earthquake source process and provide new perspective on the dynamic earthquake simulations. In Chapter 2, by comparing the back projection result with the geodetic and teleseismic slip model of the Tohoku-Oki earthquake, we first demonstrate that the peak low-frequency slip is up-dip from the hypocenter and the high-frequency radiation was generated in the deeper portion of the megathrust [*Simons et al.* 2011]. We further quantified the high-frequency energy ratio between the up-dip and down-dip region [*Huang et al.* 2012]. We relate the deep high frequency burst to small brittle asperities embedded in the ductile matrix at the root of the seismogenic zone [*Meng et al.* 2011]. This concept is now demonstrated by our physical models of earthquake rupture [*Huang et al.* 2012].

In Chapter 3, back-projection source imaging indicates that the rupture of the 2012 Off-Sumatra earthquake occurs on distinct planes in an orthogonal conjugate fault system. The rupture branched twice into a fault where dynamic stresses were compressional, challenging our conventional view of the dynamic clamping effect [*Meng Ampuero Stock et al.* 2012]. In Chapter 4, we develop dynamic rupture simulations to offer a mechanical interpretation for this puzzling observation. We find that the compressional branching can only occur under slow rupture speed and a low apparent friction coefficient, possibly aided by the poroelastic effect [*Meng and Ampuero* 2012].

While the array-process provides insight on the earthquake physics, the conventional teleseismic back projection only works on large earthquakes with M > 8.0 due to limited resolution. In Chapter 5, back projection is extended to earthquakes recorded at regional distance which enables the imagery of moderate M ~ 7 events. For instance, we image the 2010 Haiti earthquake with the Venezuela seismic network. We observe two high frequency subevents at the terminal end of the major geodetic slip regions, which can be interpreted as stopping phases associated with abrupt rupture speed reduction at the edge of the slip area [*Meng, Ampuero, Sladen et al.* 2012].

Besides these applications, this thesis also studied the reliability of the back projection to avoid misinterpretation of the potential artifact. Motivated by the gap between the low frequency geodetic model and high frequency back projection of the Tohoku-Oki earthquake, some low frequency (~ 0.1 Hz) back-projections indicate that the progressive transition of frequency-dependent rupture properties is observable [*Koper, Hutko, Lay* 2011; *Yao et al.* 2011; *Lay et al.* 2012]. In Chapter 6, however, we demonstrate that the "swimming effect," a systematic drift resulting from signal non-stationarity, induces significant bias on beamforming back-projection at low frequencies, resulting in the apparent frequency-dependent slip behavior [*Meng, Ampuero, Luo et al.* 2012]. On the other hand, I introduced a "reference window strategy" into the multitaper-MUSIC back-projection technique, which significantly mitigates the "swimming artifact". These concerns of potential artifacts demonstrate the need to perform more rigorous synthetic tests involving more realistic rupture scenarios and crustal velocity models, which could be addressed in future work beyond the scope of this thesis.

This thesis marks the beginning of an endeavor into earthquake physics using advanced array processing techniques. Future work will undoubtedly involve case studies of other earthquakes addressing open questions of source dynamics. Furthermore, I expect more efforts in developing dynamic earthquake models that assimilate the new seismological observations and their uncertainties. Looking forward, I also anticipate progress in the following aspects of earthquake source imaging.

One of the advantages of back-projection over conventional source inversion is the minimal prior assumption of fault geometry and Green's functions. This leads to the idea of automated rapid earthquake source imaging aimed to provide key parameters like the rupture extent and speed, and the distribution of source power and subevent locations. The system can be designed to monitor

major subduction zones and strike-slip systems such as the San Andreas fault with preselected stations, frequency bands, and so on. These parameters can be obtained from analysis of previous earthquakes or synthetic tests of hypothetical rupture scenarios. For the regional back projection, the required hypocentral location and the focal strike can be acquired from automated moment tensor solutions. A pilot program could start with the Venezuela seismic network which has the capability to monitor the major Caribbean fault system, a place vulnerable to seismic hazard due to lack of coverage.

The fact that back-projection and finite source inversion work at different frequency ranges gives rise to an interesting question: How can back projection be used to constrain the finite fault inversion? As a starting point, one can use the rupture speed and timing acquired from back-projections to constrain the finite fault models [*Lay et al.* 2010]. A more thorough approach is to add a metric of the back projection misfit into the cost function of the source inversion. To first order, the metric can be the mismatch of the peak location of the back projection image at each time frame. Assuming the finite fault inversion is solved by a iterative method, a computationally efficient back projection implementation needs to be performed at each iteration. A parallel implementation of the MUSIC back projection code is under development for this purpose. The ultimate goal is to construct unified source models to satisfy the observations at both low and high frequencies and understand the frequency-dependent behaviors.

This thesis focused on back projection at teleseismic and regional distances. Another important set of data, the local strong motion recordings, has been less explored for earthquake source imaging. By exploring the concept of multiple seismic antennas made of clustered low-cost accelerometers, I anticipate more breakthroughs in earthquake early warning research (EEW). The current EEW algorithms are mainly based on the scaling relation of magnitude and frequency content which satu-

rates for earthquakes (M > 7) because of the finite source effect. The array processing at local distances can be potentially applied to track the movement of the rupture front in real time, which provides an estimate of rupture size and hence the magnitude (figure 1.3). The challenges of such ideas mainly involve the mixture of different phases and imperfect waveform coherency, which may require integrative efforts on both seismic array processing and wave propagation in random media.

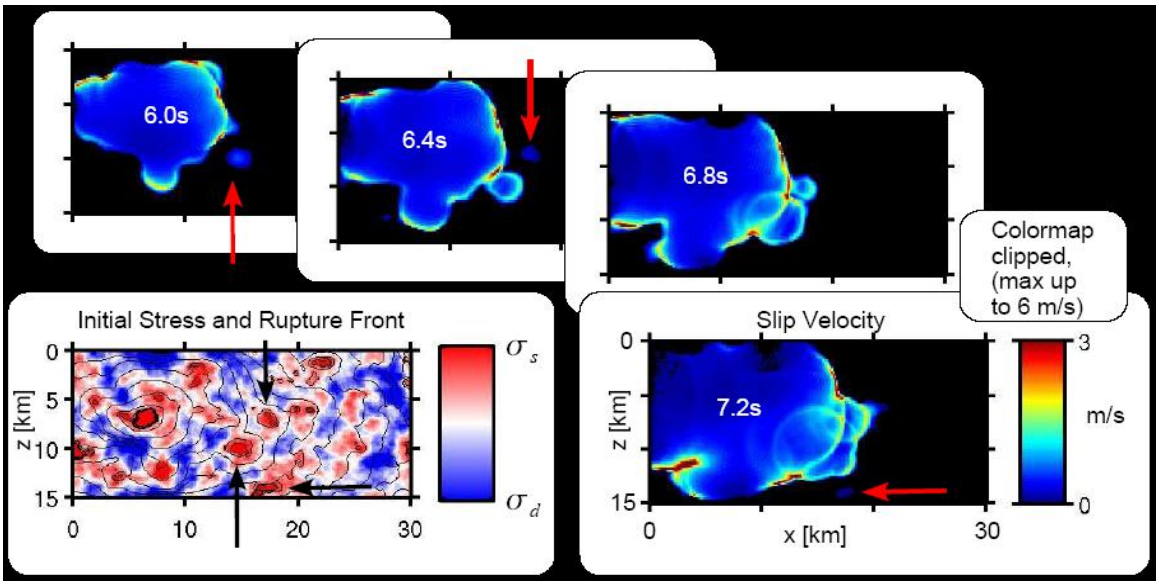

Figure 1.1. A dynamic rupture model with heterogeneous initial stresses [*Ripperger et al.* 2008]. The color plots show the fault plane view of slip rate in different snapshots. Red arrows indicate a secondary isolated rupture front. The bottom left plot shows the spatial setup of initial fault stresses. The black arrows indicate regions of high stress concentration that lead to secondary ruptures. The interaction between the primary and secondary fronts generates high-frequency bursts that cannot be resolved by conventional low-frequency source inversions.

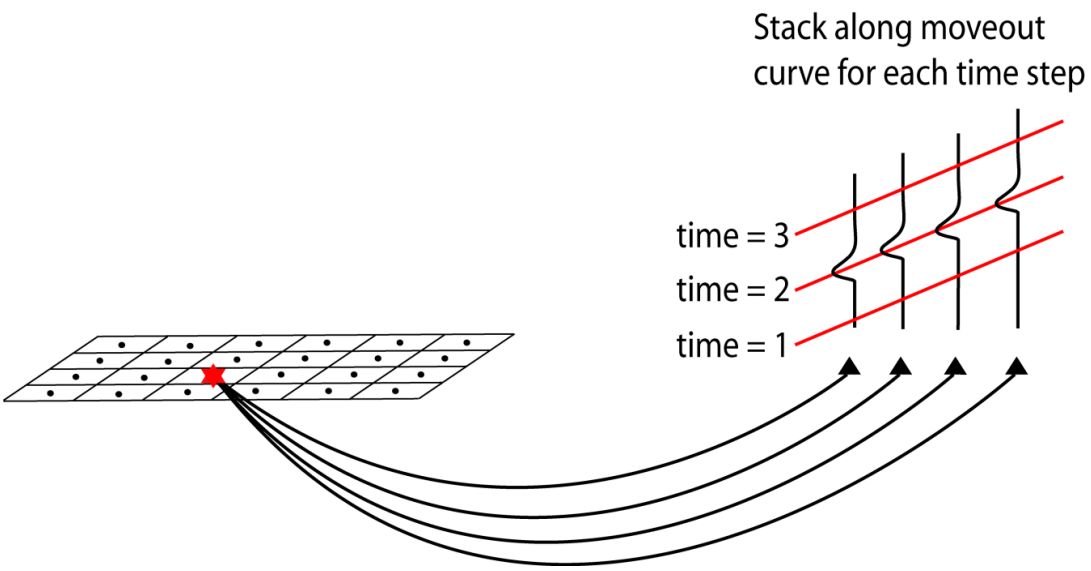

Figure 1.2. Sketch of beamforming back-projection (figure adopted from Alex Hutko's 2009 AGU talk). The black dots in the center of the rectangular grids indicate the location of testing sources. The true source location (red star) is connected to the receivers (black triangles) through ray theory. The black curves above the receivers denote the recorded seismograms. In principle, the moveout of true source locations (red lines) brings the seismograms in phase, thus the stack along the moveout reaches the maximum.

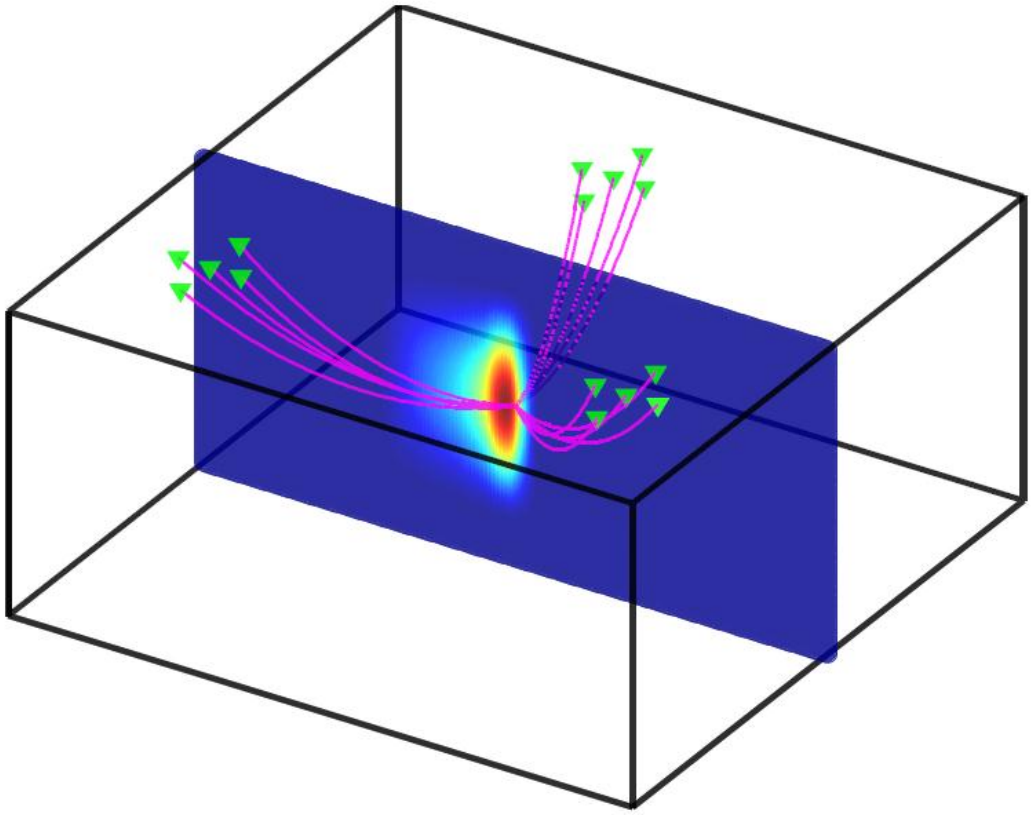

Figure 1.3. Sketch of back-projection applied to earthquake early warning. The color plots show the slip velocity of a propagating rupture front on a vertical strike slip fault. The high frequency signals generated by the rupture fronts are recorded by the network of seismic antennas composed of clustered low-cost accelerometers (green triangles). The system can track the growth of earthquake size in real time.

Chapter 2

A WINDOW INTO THE COMPLEXITY OF THE DYNAMIC RUPTURE OF THE 2011 MW 9 TOHOKU-OKI EARTHQUAKE

Originally published in L. Meng, A. Inbal and J.-P. Ampuero (2011), A window into the complexity of the dynamic rupture of the 2011 Mw 9 Tohoku-Oki earthquake. *Geophys. Res. Let.*, 38, L00G07, doi:10.1029/2011GL048118.

Note: the supplementary materials are included in Appendix A.

2.1. Abstract

The 2011 Mw 9 Tohoku-Oki earthquake, recorded by over 1000 near-field stations and multiple large-aperture arrays, is by far the best recorded earthquake in the history of seismology and provides unique opportunities to address fundamental issues in earthquake source dynamics. Here we conduct a high resolution array analysis based on recordings from the USarray and the European network. The mutually consistent results from both arrays reveal rupture complexity with unprecedented resolution, involving phases of diverse rupture speed and intermittent high frequency bursts within slow speed phases, which suggests spatially heterogeneous material properties. The earthquake initially propagates down-dip, with a slow initiation phase followed by sustained propagation at speeds of 3 km/s. The rupture then slows down to 1.5 km/s for 60 seconds. A rich sequence of bursts is generated along the down-dip rim of this slow and roughly circular rupture front. Before the end of the slow phase an extremely fast rupture front detaches at about 5 km/s towards the north. Finally a rupture front propagates toward the south running at about 2.5 km/s for over 100

km. Key features of the rupture process are confirmed by the strong motion data recorded by K-net and KIK-net. The energetic high frequency radiation episodes within a slow rupture phase suggests a patchy image of the brittle-ductile transition zone, composed of discrete brittle asperities within a ductile matrix. The high frequency is generated mainly at the down-dip edge of the principal slip regions constrained by geodesy, suggesting a variation along dip of the mechanical properties of the mega thrust fault or their spatial heterogeneity that affects rise time.

2.2. Introduction

The Mw 9 earthquake that occurred off-shore Tohoku, Japan, on March 11, 2011 is by far the best recorded earthquake in the history of seismology and will undoubtedly spawn a broad range of studies that will deeply transform earthquake science. In particular, this event provides a unique opportunity to address, through high resolution and robust observations, fundamental questions about the physics of dynamic earthquake rupture, including the initiation of rupture, the complexity of its propagation and its arrest. Here we focus on key direct observations of the spatiotemporal evolution of the rupture process of the Tohoku earthquake. We analyze seismic data available soon after the event using source imaging methods that are weakly dependent on model assumptions. We back-projected teleseismic waveforms applying high-resolution array processing techniques to obtain a high-frequency image of the rupture process of this megaearthquake. We then identified prominent features of the local strong-motion recordings that we associate to the main phases of the rupture process. Our results reveal, with unprecedented detail, rich patterns of high frequency radiation from the deep portions of the seismogenic zone. Our observations open a direct window into the complexity of dynamic rupture, including phases of slow and extremely fast rupture, and its relation to the heterogeneous nature of the subduction interface.

Back-projection of high-frequency (HF) seismic waves recorded by dense arrays [*Fletcher et al.* 2006; *Ishii et al.* 2005] delivers unique insights on earthquake rupture processes that are complementary to traditional finite source inversions. Array back-projection aims at tracking the areas of the source that generate the strongest high frequency radiation based solely on the phase and the coherency of seismic array signals. This provides robust constraints on the spatiotemporal evolution of the earthquake rupture, without relying on assumed Green's functions nor on restrictive parameterizations of the rupture kinematics. We back-projected P wave seismic waveforms recorded by two large arrays at teleseismic distances, the USArray and the European network, that illuminate the fault from two orthogonal directions (figure 2.1). We causally filtered the waveforms from 0.5 to 1 Hz, the highest band in which the initial arrivals are coherent to be aligned robustly. We then applied three different array processing techniques: cubic-root stacking [*Rost and Thomas* 2002], a classical beamforming technique; Multiple Signal Classification (MUSIC) [*Goldstein and Archuleta* 1991; *Schmidt* 1986], a high-resolution technique designed to resolve closely spaced simultaneous sources; and correlation stacking [*Borcea et al.* 2005; *Fletcher et al.* 2006], a technique known to improve robustness in the presence of scattering. The detailed descriptions of the techniques are included in the chapter A. Our results based on these three techniques are mutually consistent (figures 2.1, 2.1, A.1 and A.2). Nevertheless, we found that MUSIC consistently yields a sharper image of secondary features of the rupture process. We back-projected the estimated directions of arrival onto the source region using differential travel times relative to the hypocentral travel time, based on the IASP91 Earth model. Due to the lack of sensitivity of differential travel times to source depth, we project the array images at an arbitrary reference depth of 15 km. We focus on features of the rupture process that are consistently imaged by both arrays. Remaining differences can be attributed to directivity effects, to interference patterns between direct and depth phases and to geometrical properties of the isochrones [*Bernard and Madariaga* 1984; *Spudich and Frazer*,1984]. Owing to its larger aperture, the European array provides a sharper image of the rupture

process. Our synthetic tests based on empirical Green's functions (Figures S4-S7) show that our back-projection imaging can capture the key features of the rupture process of the Tohoku-Oki earthquake highlighted next.

2.3. High Resolution Array Analysis Using USarray and European Network

Figure 2.1-a shows the location of the regions of strongest HF radiation within 10 seconds long sliding windows. Secondary sources are often visible in our back-projection images, for instance in figure 2.3 between 60 and 90 seconds. However, our focus here is on first order features that we can reliably identify by tracking the most coherent phase within each time window. The HF radiation area extends bilaterally over 300 km along strike, roughly one third to the NNW direction and two thirds to the SSE. It bridges over the rupture area of several historical earthquakes off-shore Miyagi and Fukushima that were previously thought to define the segmentation of this subduction interface. The HF rupture is mostly located landwards of the hypocenter, near the down-dip end of the seismogenic zone of the megathrust interface determined from the spatial distribution of megathrust seismicity in the last decades [*Igarashi et al.* 2001]. Figure 2.1-a also shows the spatial distribution of coseismic slip averaged over a large collection of possible models constrained by geodetic (GPS) and tsunami (DART buoy) data in a Bayesian framework [*Simons et al.* 2011]. The locations of HF sources correlate with the down-dip edge of the main slip area. While coseismic slip inversions produced by different teams differ significantly, the spatial complementarity between low and high frequency slip is a common feature well illustrated by this particular slip model. Kinematic source inversions constrained by global teleseismic data, which are dominated by frequencies lower than 0.1 Hz for this earthquake, also place most of the low frequency (LF) slip updip from the hypocenter [*Shao et al.* 2011]. This observation is not affected by the uncertainty in the hypocenter location. We found no secondary HF source between the trench and the hypocenter. Moreover, our back-

projection analysis at lower frequencies, down to 0.125 Hz (figure A.8), the minimum frequency that allows reasonable temporal resolution, does not show a conclusive trend toward shallower slip. This suggests that slip in the shallower regions of the megathrust interface generated much weaker seismic wave radiation at periods shorter than 10 s.

2.4. The Spatiotemporal Evolution of the Tohoku Earthquake

The spatiotemporal evolution of the strongest HF radiations is indicated in Figure 2.1-a. Sustained and energetic HF radiation is reliably imaged by our array back-projections during the first 150 seconds of the rupture. The overall extent of HF rupture size during this period indicates a low average rupture speed. However, rupture speed was highly variable, with several stages of slow, fast and extremely fast rupture. A summary plot of rupture time as a function of epicentral distance, shown in Figure 2.2 and Figure A.8 (plotted along dip and strike), provides a more quantitative appreciation of the rupture speed and allows the identification of several distinct stages of the rupture process. Finer details can be observed in the back-projection imaging snapshots (Figure 2.3) and movies (Animation A.1 and A.2), including simultaneous but weaker HF sources. The HF rupture initially propagates down-dip for about 100 seconds, and then splits up into bilateral rupture along strike. The down-dip propagation stage starts with a slow phase: the centroid of HF radiation stalls in a confined area and the source power increases gradually for about 10 seconds (phase 1 indicated in Figure 2.2). This initiation culminates in a definite change of rupture speed. In the subsequent stage (phase 2) the rupture propagates towards the West at usual speeds of order 3 km/s for about 20 seconds. The rupture then slows down to less than 1 km/s or even ceases for about one minute (phase 3). In Figure 2.2 the HF source positions show wide azimuthal fluctuations but very slow advance in epicentral distance during this phase. The complex structure of this slow stage is most clearly visualized in the back-projection movies derived from the European array (Animation S2).

Figure 2.3 shows two simultaneous HF sources active at t = 55, 75 and 85 s that delineate an arcuate shaped front. The rupture appears as a rich sequence of bursts generated along the rim of a slowly expanding circular front. The slow front is centered significantly down-dip from the hypocenter, which produces episodes of apparent back-propagation. On the other hand, most low frequency slip occurs in the same stage but mainly located up-dip direction from the hypocenter [*Shao et al.* 2011]. By the end of the slow stage, at about 80 seconds, an extremely fast rupture detaches towards the north, with apparent supershear speed of order 5 km/s (phase 4), given the local crust S wave velocity is 3.42 - 4.5 km/s [*Takahashi et al.* 2004]. Finally a fast rupture front propagates toward the south running at speeds of order 2.5 km/s for more than 100 km (phase 5).

2.5. Signatures of the Rupture Process in the Strong Motion Data

We inspected the near-source ground motions recorded by dense strong motion networks in Japan to identify the local signature of the fepatures we observed at teleseismic distances. We analyzed recordings of 64 surface and 42 borehole accelerometers located along the northeastern coast of Honshu. We band-pass filtered the traces in various frequency bands, integrated to velocity and computed smoothed S wave energy envelopes (Figure A.9). Figure 2.4 shows 5 - 10 Hz envelopes as a function of station latitude. Amplitudes are normalized to emphasize the arrival time moveout of the main strong motion phases. Three episodes are prominent, two in the north, consistent with sources near the hypocentral latitude, and one far south near the end of the rupture. We trace rays from the HF source locations determined by the back-projection analysis to the strong motion stations, using a 1D velocity model derived from local seismic profiles [*Takahashi et al.* 2004]. The three prominent bursts are thus associated to HF phases observed at teleseismic distances. The colored vertical short bars in Figure 2.4 indicate the S-wave arrival times from locations that ruptured

33, 85 and 140 seconds after the mainshock origin time. These correspond, respectively, to the end of the first fast rupture stage, the beginning of the extremely fast northwards rupture and the approach to the southern end of the rupture. The strong motions are intermittent in Miyagi and more sustained along Fukushima, reflecting the contrasted character of these two portions of the rupture process (phase 3 and 5, respectively).

2.6. Discussion

We inspected the near-source ground motions recorded by dense strong motion networks in Japan Our results highlight the spatial complementarity between low and high frequency source properties of the Tohoku earthquake, as also discussed elsewhere [*Simons et al.* 2011]. This phenomenon has been reported for several other earthquakes, although not systematically [*Nakahara* 2008]. High frequency is radiated by fast changes in rupture speed or in slip. These changes can be due to the presence of frictional heterogeneities in the brittle-ductile transitional regions at the base of the seismogenic zone, stopping phases radiated from abrupt rupture arrest, strong phases radiated when the rupture front encounters residual stress concentrations left by previous earthquakes [*Madariaga* 1983] and dynamic triggering of crustal faults above the megathrust. A natural generalization of this HF/LF complementarity to intermediate frequencies poses a cautionary note for source inversion studies that combine geodetic and seismological data, which are sensitive to different frequencies. The relation between HF and LF source radiation also provides an observational constraint on kinematic source models for broadband ground motion prediction and urges for the integration of physics-based rupture models into those methodologies [*Pulido and Dalgue* 2009].

Our analysis reveals the seismic signature of a slow initiation of the Tohoku-Oki earthquake rupture. We used only the European data to resolve this initiation phase, since the USarray is at a P nodal direction and dominated by the sP phase which complicated the initial waveforms. Back-

projection of the initial portions of the waveforms was done with short (5 s long) sliding windows. Extrapolating in figure 2.2 the moveout of the HF sources during "phase 2" down to zero distance unambiguously reveals an initial rupture delay longer than the analysis window. Local strong motion recordings are deficient in high frequency content during the first 10 s [*Hoshiba and Kazuhiro* 2011], independently implying a slow initiation. A progressive transition to dynamic rupture has been observed in laboratory experiments [*Nielsen et al.* 2010; *Ohnaka and Kuwahara* 1990; *Okubo and Dieterich* 1984] and predicted by theoretical models [*Ampuero and Rubin* 2008; *Dieterich* 1992; *Lapusta and Rice* 2003], but has eluded unambiguous seismological observations at natural scales. Whether this initiation stage is subtended by an aseismic nucleation process or results from a cascade of triggering between seismic subevents [*Ellsworth and Beroza* 1995] cannot be resolved by our analysis. The duration of the observed slow initiation stage (less than 10 s) is consistent with the empirical scaling relation between nucleation phase duration and seismic moment proposed by Ellsworth and Beroza (1995), although somewhat shorter suggesting a break in scaling at very large magnitudes possibly due to saturation of the seismogenic depth. Further studies of the nucleation of the Tohoku earthquake are warranted, including imaging of its early stages based on empirical Green's functions [*Shibazaki et al.* 2002; *Uchide and Ide* 2007] and analysis of its foreshock sequence [*Bouchon et al.* 2011].

During the second slow rupture stage of the Tohoku earthquake (phase 3 in figure 2.2), the macroscopic rupture front almost comes to a halt and then restarts. This stage provides another potential window into the factors controlling earthquake nucleation and arrest, especially under transient stressing conditions. A similar slow rupture stage with apparent speed of order 1 km/s was inferred between two main asperities during the 2007 Pisco earthquake, off-shore Peru [*Perfettini et al.* 2010]. However, the scarcity of data recorded for that event did not allow resolving whether the long delay between the two main subevents was due to a slow rupture or to a delayed triggering

process. For the Tohoku earthquake the migration pattern of the HF radiation during the slow stage is consistent with triggering along the rim of a slow rupture front. This slow stage could be related to propagation over a transition region between brittle and ductile fault behavior that separates the hypocentral region from the slip regions of the 1978 and 2005 Miyagi-Oki earthquakes. We picture this as a rheologically heterogeneous region made of a ductile fault matrix interspersed with compact brittle asperities capable of generating HF radiation. This patchy view of the brittle-ductile transition zone is consistent with the observation of clusters of repeating earthquake in Tohoku [*Igarashi et al.* 2001], and is analogous to a current interpretation of the environment where coupled slow slip and tremor processes occur [*Ito et al.* 2007]. Moreover, throughout the rest of the rupture the HF sources coincide with the down-dip end of the background interplate seismicity [*Igarashi et al.* 2001]. In an alternative interpretation, the rupture slowed down as it propagated over regions of low stress within the slip area of the 1978 and 2005 Miyagi earthquakes, but radiated HF as it hit the stress concentrations left at the edges of those same events. Similarly, the final rupture stage towards the South delineates the bottom edge of historical earthquakes off-Fukushima. Yet another possibility is that the dynamic stress transfer from a slow megathrust rupture (deficient in HF) triggered brittle rupture (rich in HF) on faults in the overriding plate. A finer resolution study of the depth and focal mechanism of the HF sources, aftershocks and repeating earthquakes might help discriminating these interpretations.

The stage of extremely fast rupture toward the north is most clearly visible by the European array, which has better resolution in the along-strike direction. This stage could correspond to a supershear rupture front. Its speed is comparable to $\sqrt{\mathbf{2}}$ times the S wave speed, a stable speed in dynamic models of supershear rupture [*Rosakis* 2002]. A subshear front hitting obliquely into a barrier is an alternative interpretation, but that would generate an apparent speed in the observed range only under very restrictive conditions. Alternatively, dynamic triggering would create an apparent su-

pershear phenomena, since the back-projection tends to image apparent secondary sources with small power connecting true sources (Figure A.7). This artifact is unlikely for the Tohoku-Oki earthquake, since the power is almost uniform during the supershear stage. However, the very fast front propagates mainly along strike and existing theoretical models do not allow supershear ruptures in mode III. Along-strike supershear rupture in subduction earthquakes requires a significant along-strike slip component or yet unexplored mode coupling processes that efficiently break the mode III symmetries. While the second strong phase observed in the strong motion data can be associated to the HF radiation found in dynamic rupture models during the transition to supershear speeds, this is not a unique interpretation. Further signatures of supershear propagation might be found in the local strong motion data if there is significant Mach cone radiation towards the land. Ocean bottom pressure gauges that recorded HF acoustic signals, especially stations TM1 and TM2, could also provide precious insight into this question.

Our observations provide an overview of the complicated rupture process of the Tohoku-Oki earthquake and virtually constitute, in a single event, a catalog of the broad spectra of earthquake phenomenology. We highlighted here key features of relevance for earthquake dynamics. These are potential targets for further efforts to assimilate the wealth of data related to this megaearthquake, with the ultimate goal of understanding the relations between earthquake complexity and the heterogeneous and multiscale structure of active fault zones.

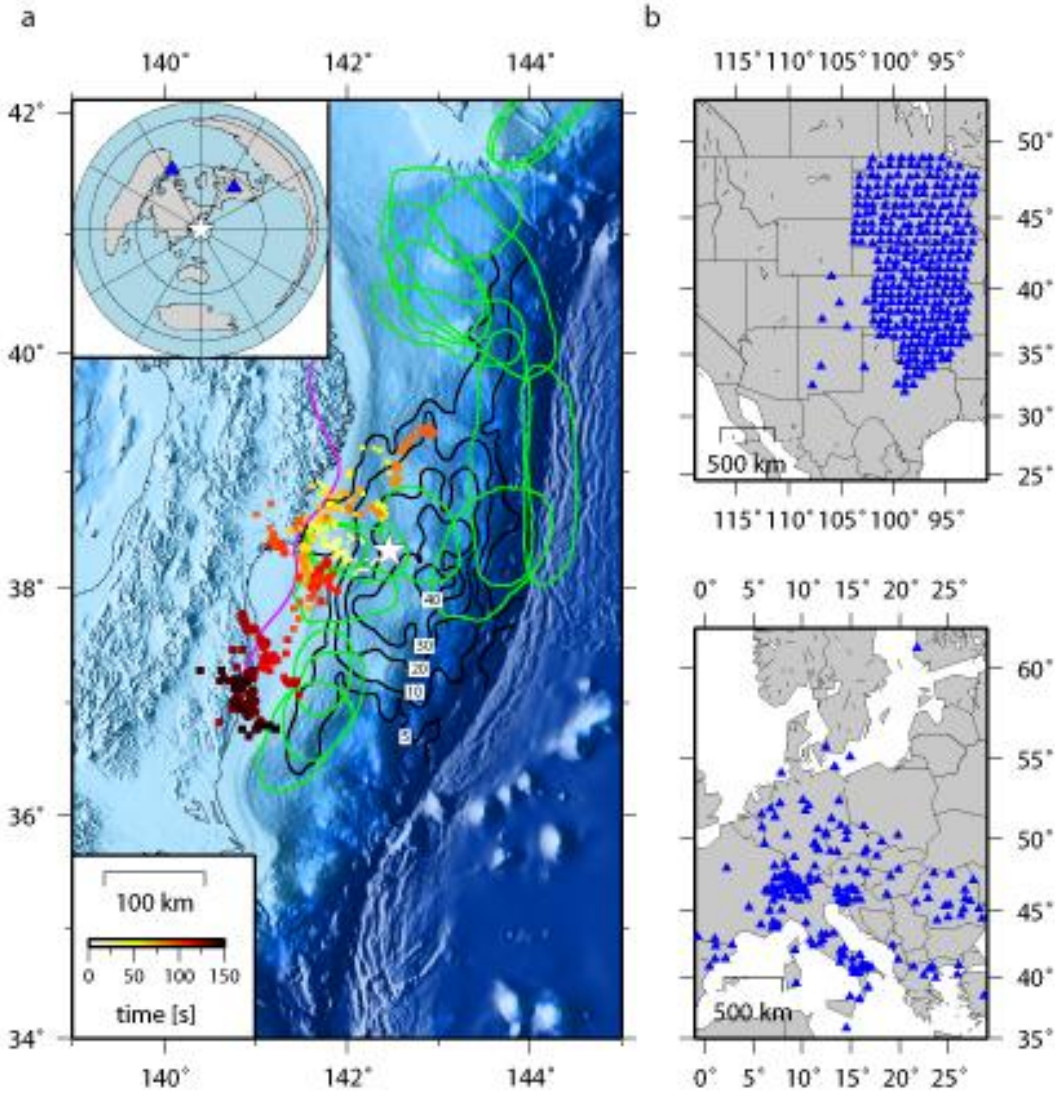

Figure 2.1. Tohoku-Oki earthquake imaged by the USarray and European network. (a) Location of the strongest high frequency radiators of the Tohoku-Oki earthquake, seen by the USarray (squares) and by the European network (circles). The color denotes the timing with respect to the origin time. The size of the symbols denote the relative amplitude of the radiators. The black contours map the average slip distribution constrained by geodetic and tsunami data [*Simons et al*. 2011]. The green ellipses represent the approximate rupture zone of the historical earthquakes. The pink line near the coast indicates the down-dip limit of the megathrust seismicity [*Igarashi et al.* 2001]. The inset map shows the location of the two arrays with respect to Japan. (b) Location of the 291 USarray and 181 European stations selected for our back-projection analysis.

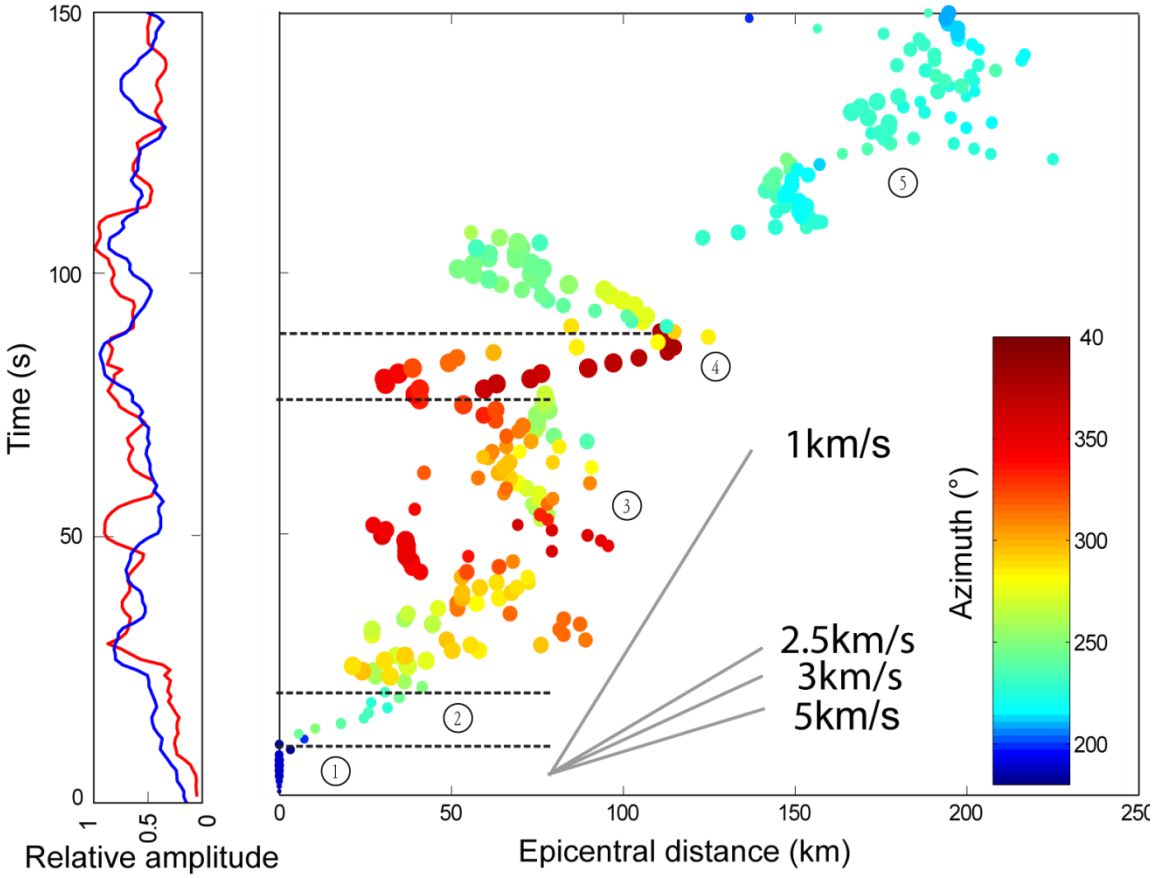

Figure 2.2. Rupture time vs. epicentral distance. The timing of the high frequency radiators seen by both arrays are plotted against their epicentral distance. The color denotes their azimuth with respect to the epicenter and the size of the circles denotes their relative amplitude normalized by the maximum amplitude during the event. The numbers in circles mark the five phases with distinct rupture behavior discussed in section 2.3. The left panel shows the temporal evolution of normalized amplitudes estimated at the USarray (blue) and at the European network (red). The slope of the gray lines indicate rupture speeds of 1 km/s (slow), 2.5 km/s, 3 km/s (regular) and 5 km/s (supershear). For reference, the local crust S wave velocity is 3.42 to 4.5 km/s [*Takahashi et al.* 2004].

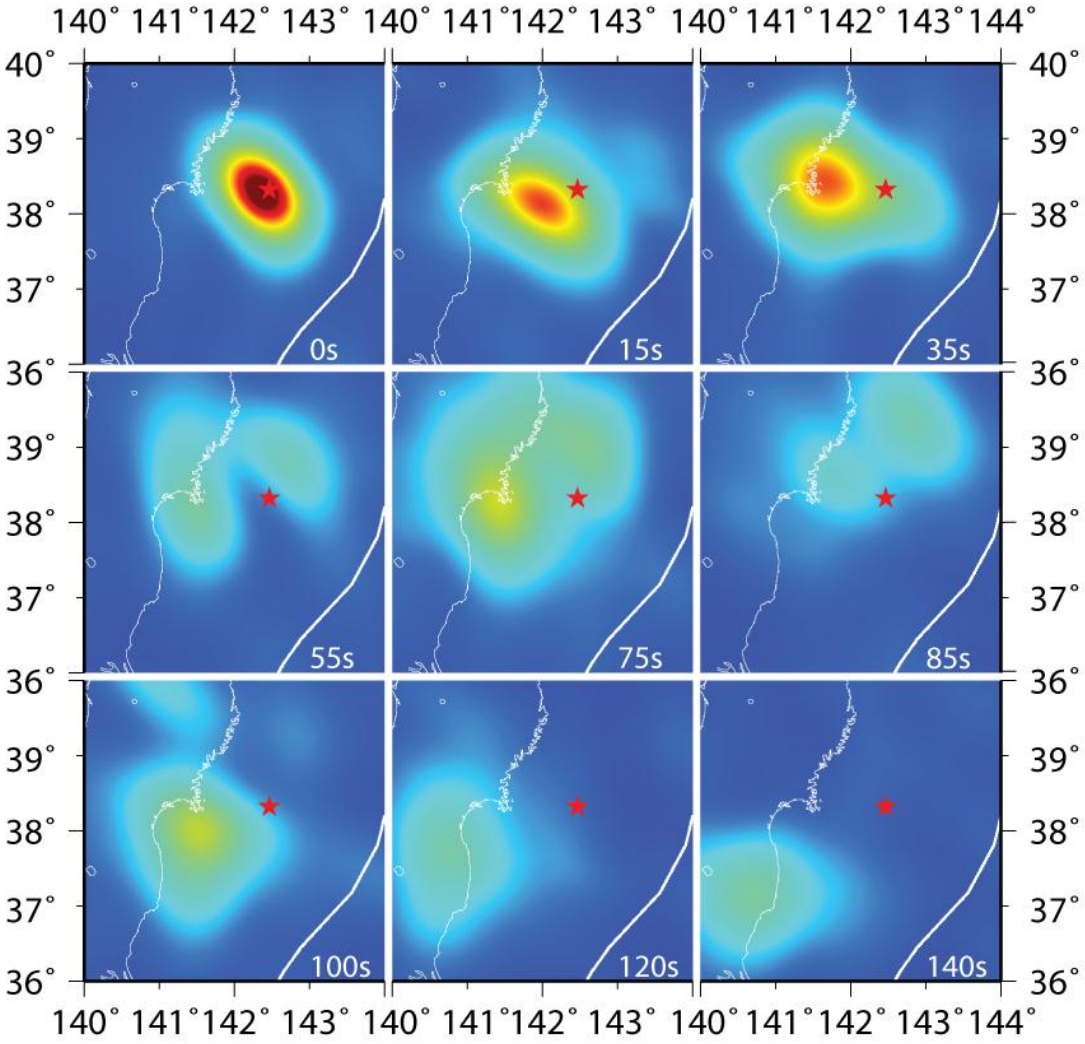

Figure 2.3. Back projection images every 20 seconds. Colors show the amplitude of the MUSIC pseudospectrum. The warmer colors indicate the location of the dominant high frequency radiation sources. The additional snapshot at 90 seconds contains a supershear front to the north. The red star denotes the mainshock epicenter and small white dots the epicenters of aftershocks with magnitude larger than 6 within the first 2 days. The thick white line represents the trench.

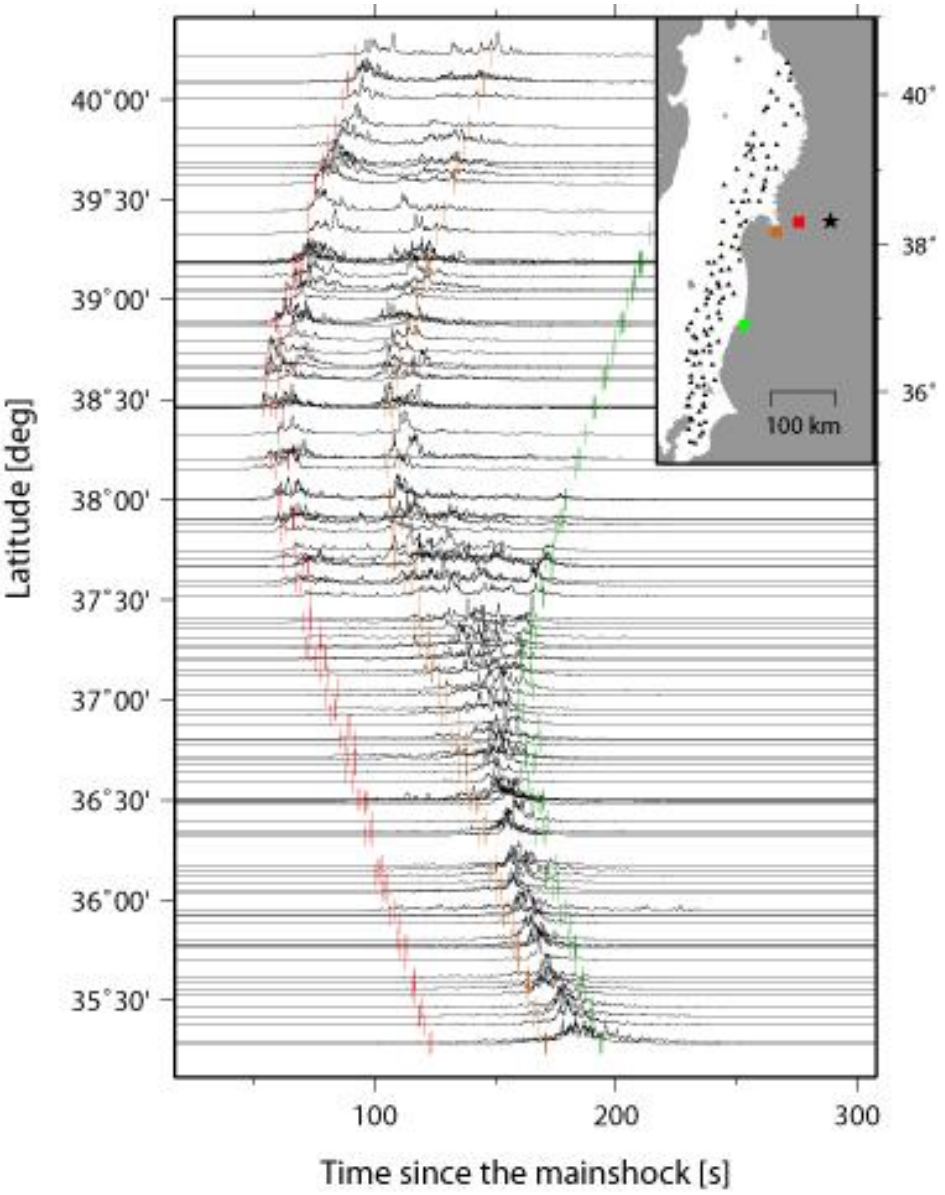

Figure 2.4. Signatures of the rupture process in the near-source strong motion recordings. Smoothed high-frequency (5-10 Hz) horizontal energy envelopes of strong motion data recorded along the northeastern coast of Honshu. The selected stations are shown by triangles in the inset map. Traces are scaled by their maximal amplitude. Red, yellow and green vertical bars along the time series indicate the S-wave travel times from high-frequency sources inferred by the back-projection analysis. These ruptured 33 s, 85 s and 140 s after the mainshock origin time, respectively. Their locations are indicated by squares of the respective color in the inset map. The stars denotes the mainshock epicenter.

Chapter 3

AN EARTHQUAKE IN A MAZE: COMPRESSIONAL RUPTURE BRANCHING DURING THE APRIL 11 2012 M8.6 SUMATRA EARTHQUAKE

Originally published in L. Meng, J.-P. Ampuero, J. Stock, Z. Duputel, Y. Luo and V. C. Tsai (2012). Earthquake in a maze: Compressional rupture branching during the 2012 Mw 8.6 Sumatra earthquake. *Science*, doi:10.1126/science.1224030.

Note: the supplementary materials are included in Appendix B.

3.1. Abstract

Seismological observations of the 2012 Mw 8.6 Sumatra earthquake reveal unprecedented complexity of dynamic rupture. The surprisingly large magnitude results from the combination of deep extent, high stress drop and rupture of multiple faults. Back-projection source imaging indicates that the rupture occurs on distinct planes in an orthogonal conjugate fault system, with relatively slow rupture speed. The ESE-WNW ruptures add a new dimension to the seismotectonics of the Wharton Basin which was previously thought to be controlled by N - S strike-slip faulting. The rupture turns twice into the compressive quadrant, against the preferred branching direction predicted by dynamic coulomb stress calculations. Orthogonal faulting and compressional branching indicate that rupture is controlled by a pressure-insensitive strength of the deep oceanic lithosphere.

3.2. Introduction

The April 11 2012 Mw 8.6 earthquake off-shore Sumatra is a record-breaking event in many respects. It is the largest strike-slip and intraplate earthquake ever recorded and, as shown here, one

of the most complicated ruptures ever imaged by modern seismology. The faulting geometry and the peculiarities of its complex rupture path offer a rare opportunity to probe the mechanics of the oceanic lithosphere.

The earthquake occurred in the diffuse deformation zone between the Indian and Australian plates (inset of Fig. 3.1-left). Its focal mechanism is typical for the region [*Engdahl et al.* 2007], with T-axis normal to the Sumatra subduction trench as observed for intraplate oceanic strike-slip earthquakes elsewhere [*Choy and McGarr* 2002] and consistent with regional stress modeling [*Cloetingh and Wortel* 1986] Rupture initiated in Paleogene oceanic lithosphere formed at the Wharton Basin spreading center, but extended unimpeded into the adjacent oceanic lithosphere affected by later volcanism on the Ninetyeast Ridge (NER).

3.3. Rupture Process of the Off-Sumatra Earthquake

Due to the remote offshore location of this earthquake, geodetic constraints on fault geometry and static slip for teleseismic finite source inversions are unavailable. We imaged the rupture process by back-projection of teleseismic data from European and Japanese seismic networks. We applied the Multitaper-MUSIC array processing technique, which provides higher resolution than conventional beamforming [*Meng et al.* 2011]. We also adopted a "reference window" strategy to avoid the systematic "swimming" artifact [*Meng, Ampuero, Luo et al.* 2012]. High-frequency (HF, 0.5-1 Hz) source radiation is reliably imaged during 160 seconds (movies B.1 and B.2). The methods and their resolution and uncertainty analysis are described in the supplementary materials. The spatiotemporal evolution of the main HF sources (Figs. 3.1 and 3.2) is remarkably complex. The rupture involved at least three different, almost orthogonal, faults. Their strikes are con-

sistent with the conjugate planes of centroid moment tensor (CMT) solutions and with the distribution of aftershocks (Fig. 3.1). The rupture process comprises at least three distinct stages (inset of Fig. 3.1-right) and the rupture length and speed on each fault are shown in Figure 3.2. It started as a bilateral rupture on a fault striking WNW - ESE ("fault A") with rupture length of ~100 km and duration of ~25 s. This stage generated the strongest HF radiation (Fig. B.3). The rupture then branched into an almost orthogonal fault ("fault B") breaking bilaterally for ~60 s over 300 km. The onset of rupture to the NNE on fault B was delayed by ~15 s and then propagated until near the Sumatra trench. Fault B's SSW rupture front branched into a third almost orthogonal fault ("fault C") which ruptured to the NNW for ~100 km. The final rupture stage involved stepping northward from fault C onto a parallel fault ("fault D") that crossed the NER. The total rupture length on faults A, B and C is 500 km, half that obtained by extrapolating empirical scaling relations [*Wells and Coppersmith* 1994]. Two hours later, the largest (M 8.2) aftershock initiated on the SSE continuation of fault C but ruptured bilaterally for ~100 km on an orthogonal fault (also shown in Fig. 3.1-right).

3.4. The Unexpectedly Large Magnitude

The magnitude of this earthquake is surprising in an intraplate environment characterized by relatively short faults with wide stepovers. With hindsight, the large magnitude of the 2012 Sumatra earthquake stems from a conjunction of circumstances: wide depth extent, high stress drop and rupture of multiple faults. Reported centroid depths are below 25 km (USGS CMT/W-phase solution; GCMT). Rupture penetrating into the uppermost mantle is consistent with old, hence thick oceanic lithosphere (~55 Ma, ~35 km, [*Wiens and Stein et al.* 1983]). West of the NER, seismic reflection lines show faults cutting through the Moho discontinuity [*Chamotrooke and Delescluse* 2008]. Considering uniform slip in a 500 km long and 40 km deep rupture, the estimated average

slip is ~15 m and the stress drop is ~15 MPa, high but similar to the stress drop of other large oceanic strike-slip earthquakes [*Robinson et al.* 2001*; Antolik et al.* 2000] and not unusual for intraplate and sub-crustal earthquakes [*Allmann and Shearer.* 2009]. The multi-segment rupture was encouraged by stressing from the M9.1 2004 Sumatra megathrust earthquake, whose southernmost large slip region coincides with the latitude of the 2012 event (Fig. 1-left). Coulomb stress calculations show that thrust faulting favors slip on outer-rise strike-slip faults oblique to the trench [*Rollins and Stein.* 2010].

3.5. The Dominant E-W Rupture

The dominant E-W rupture of faults A, C and D adds a new dimension to the prevailing view of the seismotectonics of this region. These faults are subparallel to long-lived but still active faults on the NER (Figure 3.3; [*Sager et al.* 2010]). The bisecting direction of the conjugate faults is consistent with the orientation of the principal stress inferred from seismic and GPS data [*Delescluse and Chamotrooke.* 2007]. Strike-slip focal mechanisms from the zone east of the NER have previously been attributed to slip on N-S striking faults, such as those imaged in seismic lines south of the equator in the Wharton Basin [*Deplus et al.* 1998]. Active E-W striking faults west of the NER are generally attributed to compressional deformation [*Delescluse and Chamotrooke.* 2008]. The rupture geometry of this earthquake indicates that active E-W right-lateral faults are also an important part of the kinematics of this broad deformation zone.

3.6. The Orthogonally Conjugate Fault System

Back-projection imaging reveals rupture on almost orthogonal faults, as confirmed by back-projection of the M8.2 aftershock. This has been observed in earthquake pairs (e.g., 1987 M6.2 Superstition Hills–M6.7 Elmore Ranch, 1992 M7.3 Landers–M6.5 Big Bear) but only rarely dur-

ing single events, such as in the May 13 1997 M6 Kagoshima earthquake [*Horikawa* 2001] and in the 2000 M7.8 Wharton Basin earthquake [*Robinson et al.* 2001], although orthogonal faulting of the latter is not confirmed by later studies [*Abercrombie et al.* 2003]. A multiple CMT inversion (methods available in the supplementary material) yields two subevents with similar mechanism, the second one ~200 km SW of the hypocenter (Fig. 3.1-left), consistent with rupture on the SSW branch of fault B and on fault C. In the crust, conjugate shear faults intersect at an angle ~60 degrees. The seafloor magnetic patterns (Fig. 3.1-right) rule out reactivation of fossil systems of transform faults and ridges. The wide angle between these faults requires pressure-insensitive strength during their formation (Fig 3.2-inset).

3.7. Two Episodes of Rupture Branching into the Compressional Side

The rupture path of this earthquake is unexpected: in two occasions the rupture branched preferably into the compressive (strengthened) quadrant, with arrest or delay in the alternative branch. The NNW-ward rupture front on the right-lateral fault A first turned left into the SSW segment of fault B. Rupture on the NNE segment of fault B was delayed by ~15 s. This behavior is mirrored by the second branching episode. The SSW-ward rupture front on the left-lateral fault B turned right into the NNW segment of fault C. In both cases, the preferred branching direction is toward the compressive quadrant of the previous segment, opposite to the expectation based on usual values of friction coefficient. Analysis of the dynamic stresses induced near the tip of a right-lateral crack on orthogonal left-lateral faults (Fig. 3.2-right) shows that the observed branching direction requires two circumstances: low rupture speed ($\frac{V_r}{V_s} \sim 0.5$) and low apparent friction coefficient (~0.2), i.e., a small slope of the failure envelope in a shear versus normal stress diagram (Fig. 3.2-inset). The former is robustly supported by our back-projection results: the rupture speed is remarkably steady, ~2.5 km/s on faults A and B (Fig. 3.2-left), not unusual compared to

global average values but significantly slow compared to wave speeds below the oceanic Moho (50%–60 % of S wave speed [*Klingelhoefer et al.* 2010]). The latter implies a pressure-insensitive strength, which is characteristic of ductile materials at depth. An alternative explanation by poroelastic effects [*Cocco and Rice.* 2002] with large Skempton's coefficient requires high fluid pressure inconsistent with the large stress drop.

3.8. Dynamic Weakening Mechanisms at Depths

Sustained seismic rupture also requires a dynamic weakening mechanism. The relatively slow rupture speed suggests scale-dependent energy dissipation by the rupture process. The ductile shear heating instability [*Keleman and Hirth.* 2007; *McGuire and Beroza.* 2012] operates between 600-800 ℃, which is limited to roughly 40 to 60 km depth. Serpentinized peridotite has low pressure sensitivity at confining pressures over few 100 MPa, with apparent friction coefficients as low as 0.15 [*Escartin et al.* 2001], and might dynamically weaken by dehydration embrittlement [*Jung et al.* 2004]. However, the serpentinization reaction is possible only up to 400-500 ℃, which corresponds to about 25 km depth [*Christensen* 2004*; Delescluse and Chamotrooke* 2008]. A single dynamic weakening mechanism that can operate over the whole depth range of slip of this earthquake remains to be identified.

3.9. Implications for Seismic Hazard Assessment

This is not the first time an earthquake has grown larger than expected or has occured where it is least expected. The destructive 2011 M9.0 Tohoku-Oki and M6.3 Christchurch earthquakes illustrate the scientific challenge of estimating the likelihood of extreme events based on a short and incomplete historical record. The 2012 Sumatra earthquake raises the concern of similarly large events in continental strike-slip fault systems, which pose a higher hazard to populations. While

the tectonic setting in an oceanic intraplate zone of high deformation is rare, at least one of the ingredients that made this earthquake big, its large stress drop, is a general feature of other intraplate earthquakes [*Allman and Shearer* 2009]. Its rupture complexity highlights the importance of considering earthquake scenarios with multisegment ruptures. The rupture transition from faults C and D across an offset larger than 20 km is particularly extreme [*Wesnousky* 2006]. The relation to the 2004 Sumatra earthquake suggests that large outer rise events induced by megathrust events, while not producing damaging shaking because of their remote off-shore location, can pose a tsunami hazard if they have a dip component [*Lay et al.* 2011] or displace high topography [*Tanioka and Satake* 1996]. The Gorda plate in the southern Cascadia subduction zone is such an example.

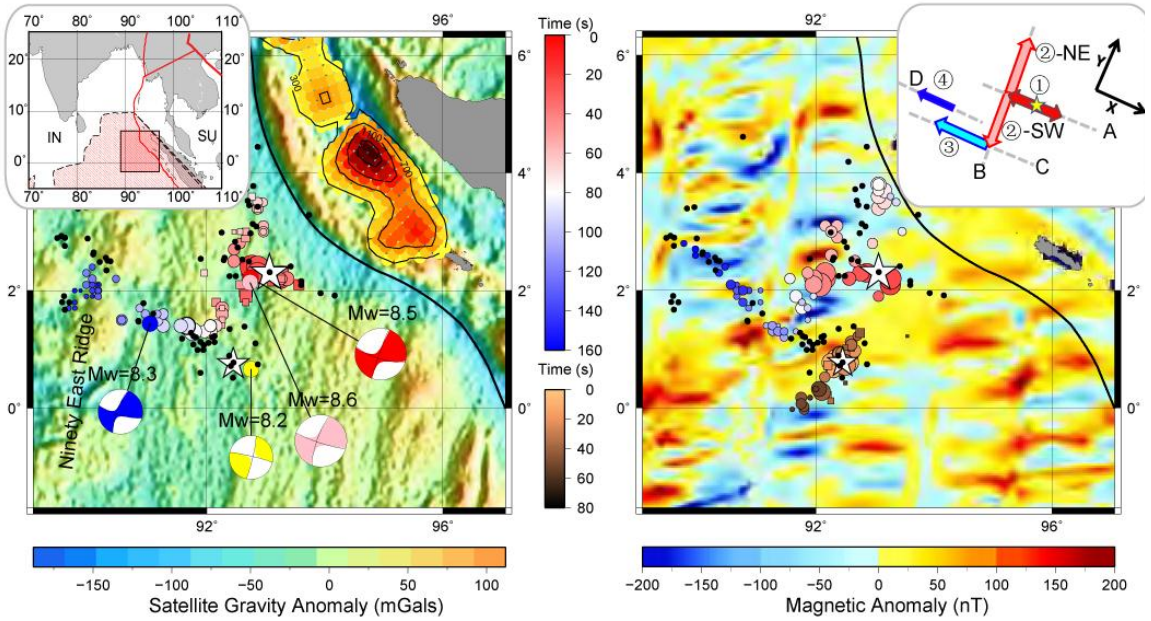

Figure 3.1. Spatiotemporal distribution of high-frequency radiation imaged by the European (left) and Japanese networks (right). Colored circles and squares indicate the positions of primary and secondary peak high-frequency radiation (from movies B.1 and B.2, respectively). Their size is scaled by beamforming amplitude and their color indicates timing relative to hypocentral time (color scale in center). The secondary peaks of the MUSIC pseudospectrum are those at least 50% as large as the main peak in the same frame. The brown shaded circles in the right figure are the high-frequency radiation peaks from the M8.2 aftershock observed from Japan. The colored contours in the Sumatra subduction zone (left) represent the slip model of the 2004 M9.1 Sumatra earthquake [*Chileh et al.* 2007]. The figure background is colored by the satellite gravity anomaly (left) in mGals (color scale on bottom-left) and the magnetic anomaly (right) in nT (color scale on bottom-right). Black dots are the epicenters of the first day of aftershocks from the NEIC catalog. The big and small white stars indicate the hypocenter of the mainshock and M8.2 aftershock. The moment tensors of the M8.6 mainshock, M8.2 aftershock and double CMT solutions of the mainshock are shown as colored pink, yellow, red and blue beach balls. The red line in the top left inset shows the boundary between the India (IN) and Sundaland (SU) plates [*DeMets et al.* 2010]. The patterned pink area is the diffuse deformation zone between the India and Australia plate. The red rectangular zone indicates the study area. The upper right inset shows the interpreted fault planes (grey dashed lines) and rupture directions (colored arrows).

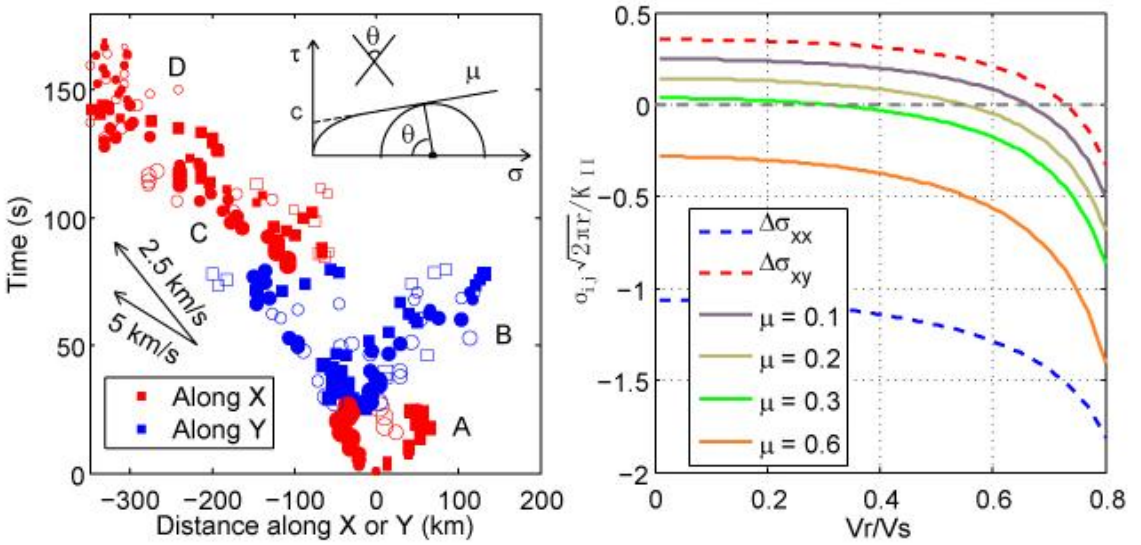

Figure 3.2. Spatiotemporal details of the rupture process. Left: timing and position of the high frequency radiators relative to the hypocenter. The position is reported in alternation along the axes labeled X (red) and Y (blue) in Fig.3.1-inset. Circles and squares are the results of Europe and Japan arrays, respectively. Filled and open symbols indicate principal and secondary high-frequency radiators, respectively. Inset: shear strength (τ) vs. normal stress (σ) diagram of a non-linear strength envelope with small apparent friction coefficient μ (almost pressure-insensitive material) and large cohesion C, resulting in almost orthogonal failure planes (Θ ~ 90 °). Right: dynamic Coulomb stress changes induced near the tip of a right-lateral crack propagating at steady rupture speed, resolved onto orthogonal left-lateral faults in the compressional quadrant as a function of the ratio between rupture speed and shear-wave speed, V_r/V_s [*Poliakov et al.* 2002]. The symbols denote dynamic changes of normal stress ($\Delta\sigma_{xx}$, negative compressive, blue dashed line), shear stress ($\Delta\sigma_{xy}$, positive left-lateral, red dashed line) and Coulomb stress ($\Delta\sigma_{xy} + \mu\Delta\sigma_{xx}$, color solid curves, assuming various apparent friction coefficients μ indicated in the legend). Stresses are normalized based on the Mode II stress intensity factor (K_{II}) and the distance to the crack tip (r). Rupture on the compressive side can be triggered (positive Coulomb stress change) only for low enough apparent friction and rupture speed.

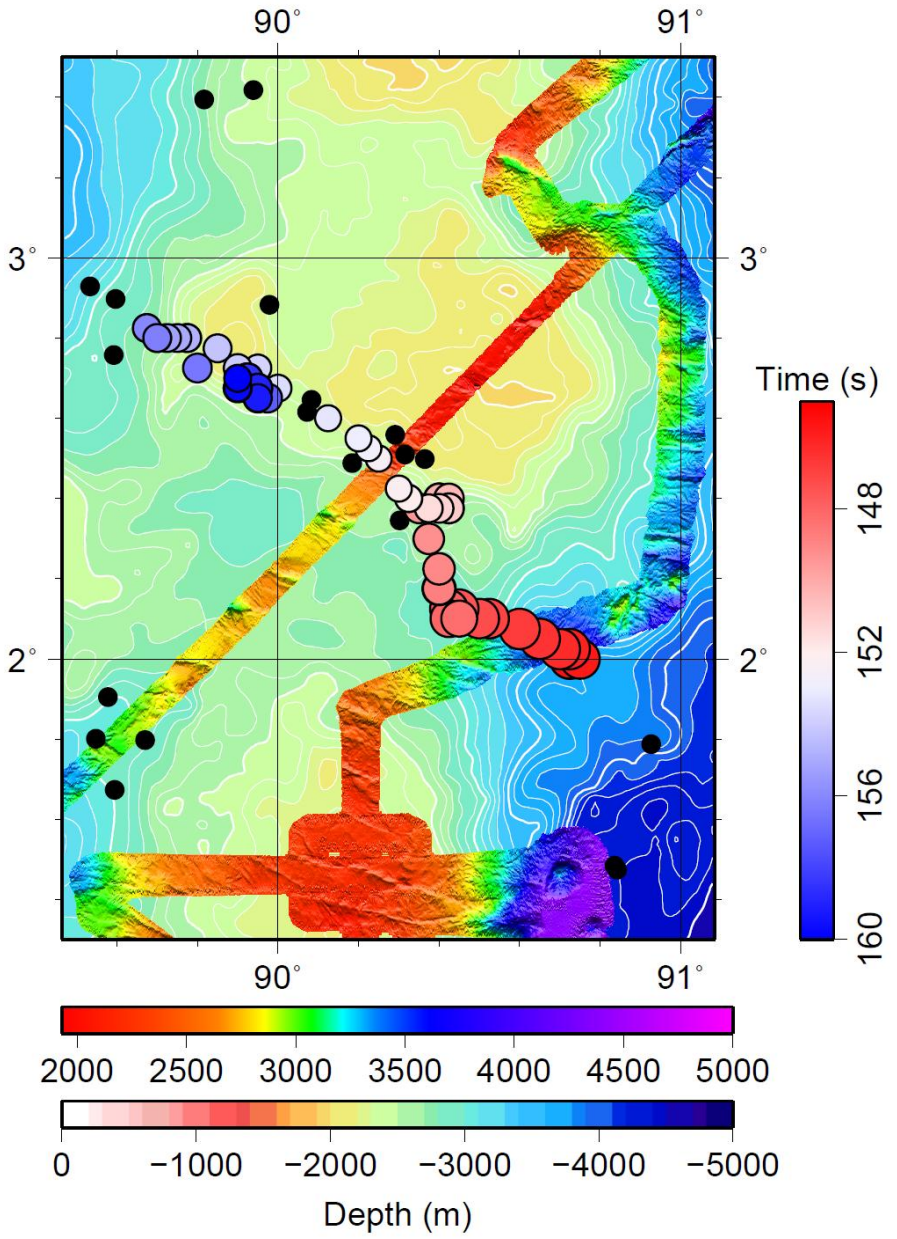

Figure 3.3. Bathymetry where the rupture crosses the Ninetyeast Ridge. Colored background is global bathymetry from SRTM30+ overlain by multibeam bathymetry from cruise KNOX06RR and cruise DYNAMO, respectively. Black dots: aftershocks, circles: HF source radiators. These indicate rupture through the NER during the last 15 s of the earthquake. The rupture plane is consistent with numerous fault scarps visible in the multibeam bathymetry.

Chapter 4

SLOW RUPTURE AND WEAKLY PRESSURE-SENSITIVE STRENGTH ENABLES COMPRESSIONAL BRANCHING: DYNAMIC RUPTURE SIMULATIONS OF THE 2012 OFF-SUMATRA EARTHQUAKE

Paper in preparation. L. Meng and J.-P. Ampuero, Slow rupture and weakly pressure-sensitive strength enables compressional branching: Dynamic rupture simulations of the 2012 Off-Sumatra earthquake.

Note: the supplementary materials are included in Appendix C.

4.1. Abstract

The 2012 M8.6 off-Sumatra earthquake, the largest strike-slip and intraplate earthquake recorded to date, followed an exceptionally tortuous rupture path. It featured two episodes of branching into fault segments that were experiencing increased compressive dynamic stresses, hence increased frictional strength. Meng, Ampuero, Stock et al. (2012) attributed this unexpected compressional branching to slow rupture and weak pressure-sensitivity of the fault strength. Here, by conducting 2D dynamic rupture simulations, we confirm that the compressional branching can only occur under slow rupture speed and low apparent friction coefficient. Poroelastic effects can also contribute by buffering the dynamic clamping. We suggest that serpentinized minerals may provide low friction, fluids and dynamic weakening down to 25 km depth, and ductile shear heating instability may provide a weakening mechanism from 40 to 60 km depth. The absence of known weakening mechanisms in the intermediate depth range suggests that rupture may penetrate over velocity-strengthening regions.

4.2. Introduction

The possibility of an earthquake rupture propagating along multiple distinct branches of a fault system has been the subject of several earthquake dynamic studies. Understanding the mechanics of fault branching, rupture path selection and the connectivity of rupture across multiple fault segments could provide a physical basis to assess the maximum earthquake size in complex fault systems. The basic principles of rupture branching are established based on analytical studies. Poliakov et al. (2002) and Kame et al. (2003) show that fault branching can occur under specific conditions of principal stress orientation, branching angles and rupture speed. On the other hand, rupture branching can be complicated by the interaction with directivity effects [*Fliss et al.* 2005], rupture propagation and arrest [*Bhat et al.* 2005], heterogeneous stress distribution and state in the earthquake cycle [*Duan and Oglesby* 2007]. The 2012 M8.6 off-Sumatra earthquake provides a rare example of large scale branching in a system of almost orthogonal faults [*Meng, Ampuero, Stock et al.* 2012]. Its rupture path showed preferred branching into the compressional side, i.e. into faults that were experiencing increased normal stresses. This challenges the conventional view that clamping increases frictional strength and hence discourages compressional branching [*Oglesby* 2005]. *Meng, Ampuero, Stock et al.* (2012) attributed this puzzling observation to weak pressure sensitivity of fault strength (low apparent friction coefficient) in the deep oceanic lithosphere.

Recent opportunities and advances in observational studies of large megathrust earthquakes, especially the 2011 M9.0 Tohoku-Oki event, based on space-geodesy [*Ozawa et al.* 2011; *Simons et al.* 2011], waveform inversions [*Ide et al.* 2011; *Wei et al.* 2012] and short-period back-projections [*Ishii et al.* 2011; *Koper, Hutko, Lay, Ammon et al.* 2011; *Meng et al.* 2011] have facilitated numerous efforts to understand the underlying earthquake physics through dynamic simulations, assessing

the role of a variety of ingredients, including depth-dependent heterogeneities [*Huang et al.* 2012; *Kato et al.* 2011], plastic dissipation and poroelasticity [*Ma et al.* 2012], subducting seamounts [*Duan et al.* 2012] and shallow velocity-strengthening [*Kozdon and Dunham et al.* 2012]. The unusual complexity of the 2012 off-Sumatra event, the largest strike-slip and intraplate earthquake recorded to date, provides an opportunity to shed light on the dynamics of such extreme events. Here, we conduct dynamic rupture simulations to address the conditions of friction, rupture speed, stress drop and poroelastic properties that allow dynamic branching on an orthogonal segment in a compressional quadrant.

4.3. Observations and their uncertainty

The fault geometry and the rupture process of this event are constrained essentially by teleseismic back-projection studies. Meng, Ampuero, Stock et al. (2012) described its complicated rupture path, involving multiple segments of a network of orthogonal conjugate faults, and branching twice into dynamically clamped fault segments (Figure 4.1). In the first compressional branching episode, when rupture on the right-lateral fault A (NW-SE oriented) reached the orthogonal left-lateral fault B (NE-SW oriented), the SW branch of fault B instantaneously started breaking, while the rupture on the NE branch was delayed by about 15 s. Later, the SW-ward rupture on fault B branched into the NW segment of the orthogonal fault C, which is again in the compressional quadrant. Here, to determine the possible range of the dynamic rupture model parameters, we quantify the uncertainty of the fault bisecting angle, the rupture speed and the mean stress drop.

The aftershocks and back-projection source imaging suggest a system of almost orthogonal faults. The two dominant orientations of the fault system are best delineated by the back-projection results

of the mainshock rupture on fault C and of the M8.2 aftershock rupture (Figure 4.1). By linearly fitting the strike of the corresponding faults, we obtained the bisecting angle of 87 +- 3 °. We also estimate the rupture speed prior to the compressional branching episodes, on the NW branch of fault A and on the SW branch of fault B. The rupture initiates rather slowly on fault A with 29% (25%~33%) of the shear wave speed at the centroid depth of 30 km in the uppermost mantle (4.6 km/s [*Klingelhoefer et al.* 2010]). The SW rupture on fault B propagates with 55% (50%~60%) of the shear wave speed. The stress drop is the quantity least constrained by the current observations, because of large uncertainties on the depth extent of the rupture. The overall mean stress drop can be estimated as $\Delta\tau = M_0 / (\pi W^2 L)$ [*Leonard et al.* 2010] Given the seismic moment of M_0 = 1e22 Nm (USGS) and rupture length L = 400 km (the combined length of faults A and B, where most of the moment was released), the estimated stress drop is $\Delta\tau$ = 2.2 MPa if we assume the depth range W = 60 km, twice the centroid depth [*Duputel et al.* 2012]. If we assume the depth range of significant slip is W = 30 km, half of the above estimate, the resulting stress drop is 8.8 MPa. However, the stress drop can be highly spatially variable. On fault A it can be as large as 17.6 MPa given half of the total moment is released there on a 100 km long rupture.

4.4. Model setup and assumptions

We develop a 2D dynamic rupture model of compressive branching during the off-Sumatra earthquake. The model comprises a T-shaped fault system with an initial fault **a** and an orthogonal fault **b**. The 2D model plane represents a crosssection of the crust at fixed depth. The midpoint of fault **b** is connected with one end of fault **a**. Both faults are 200 km long and embedded in a homogeneous rectangular elastic space with absorbing boundaries. Both faults are optimally oriented with respect to the regional stress (45 ° to the maximum principal stress axis, based on *Delescluse et al.* 2007).

The dynamic rupture simulation is solved with the spectral element code SEM2DPACK (http://www.sourceforge.net/projects/sem2d/). The assumed density, P and S wave velocities are 3000 kg/m^3, 8000 m/s and 4618 m/s, respectively.

The rupture is set to nucleate at the midpoint of fault **a**. The fault is governed by the linear slip-weakening friction law. Based on an analytical solution for the dynamic Coulomb stress at the tip of a propagating crack [*Poliakov et al.* 2002; *Freund* 1998], Meng, Ampuero, Stock et al. (2012) found that compressional branching is permitted only with low rupture speed and low friction coefficient. (We note that low friction, if accompanied by large cohesion, does not imply low absolute strength.) To confirm this interpretation, we model four different situtations: 1: slow and pressure insensitive (zero friction with cohesion and low rupture speed), 2: slow and weakly pressure sensitive (low friction and low rupture speed), 3: fast and weakly pressure sensitive (low friction and high rupture speed), 4: slow and strongly pressure sensitive (high friction and low rupture speed). The pressure sensitivity is controlled by the friction coefficient. The slow rupture speed can result from self-similar energy dissipation, for instance due to nonelastic off-fault deformation [*Andrews* 2005]. In an elastic model, this process can be mimicked by slip-weakening friction by setting a nonuniform critical slip distance *Dc* that grows linearly away from the hypocenter. The rupture speed V_r is related to other model parameters: [*Andrews et al.* 2005; *Kikuchi et al.* 1975]

$$1 - \frac{V_r}{V_R} \sim \frac{G\sigma_n \Delta\mu D_c{}'}{\Delta\tau^2}$$

where V_R is the Rayleigh wave speed, G is shear modulus, $\Delta\tau$ is the stress drop, σ_n is the normal stress, $\Delta\mu$ is the friction drop and *Dc'* is the spatial gradient of *Dc*. The stress drop is set to 13 MPa, the average of our high and low stress drop estimates. The sketch of each model is shown in figure 4.2 and the parameters are listed in table 4.1. In this study, we focus on the failure condition of fault

bc (the compressional branch). Therefore, since fault **bd** (the dilatational branch) is always favored to break by the dynamic Coulomb stress, we lock the fault **bd** to avoid triggering of **bc** by **bd** (figure C.1). We also locked the junction between faults **a** and **b**, since this particular point always has zero dynamic stress for perfectly orthogonal faults. In reality, a slightly oblique angle results in nonzero dynamic stress at the junction. Finally, we lock the last 10 km of fault **a** close to the boundary to avoid the artificial large slip and reflection phase.

4.5. Results

The spatiotemporal distributions of slip rate resulting from our simulations are shown in Figure 4.3. In all the models, the rupture propagated bilaterally along fault **a** and accelerated to steady-state speeds. In the "fast" case with small but nonzero gradient of *Dc* (model 3), the rupture reaches the Rayleigh wave speed (~ 4 km/s). The slip rate function shows cracklike behaviour with peak value closely following the leading rupture front. In contrast, in the "slow" case the relatively large gradient of *Dc* creates self-similar cracks with a large process zone, which broadens with rupture propagation distance. In models 1, 2 and 4, the peak slip velocity, which we associate with the high frequency radiation imaged by our back-projection study, propagates at a significantly slow speed, 55% percent of the shear wave speed (~ 2.5 km/s), similar to the observed value on fault B (Figure 4.1). In all the four models, the rupture reached the junction of faults **a** and **b**. However, the branching behaviors are rather different. Models 1 and 2 are set up with the same rupture speed and static strength through cohesion or low friction (Figure 4.3-inset). Fault **bc** in Model 1 instantaneously breaks when the rupture reaches the junction while the branching in Model 2 is delayed due to nonzero compressional stress. On the other hand, Models 3 and 4 fail to break fault **bc**. The large peak slip velocity due to either large rupture speed or large friction (and proportionally large friction

drop) generates a larger compressional dynamic stress field that prohibits branching. These simulations demonstrate that low rupture speed and low apparent friction are prerequisites for dynamic compressional branching. These results are stable within the range of uncertainty on stress drop and rupture speed. A set of models with slower rupture speed (30% V_s) and larger stress drop (17 Mpa) observed on fault A are shown in Figure C.2.

Another factor that can potentially facilitate compressional branching is the poroelastic effect. In a 2D linear poroelastic medium, the effective normal stress σ_e is

$$\sigma_e = \sigma_n - \sigma_P = \sigma_n - \frac{2B(1+\vartheta)}{3} \cdot \frac{\sigma_{xx} + \sigma_{yy}}{2}$$

where σ_n is the normal stress, σ_P is pore pressure, σ_{xx} and σ_{yy} are the stresses in the 2D x-y plane, ϑ is Poisson's ratio (set to 0.25) and B is the Skempton coefficient, defined as the ratio of pore pressure change to the mean stress change. The above analysis only provides necessary conditions on friction and rupture speed to break fault **bc**, but it does not explain why the preferred branching direction is toward the compressive side. Viesca et al. (2008); Ma (2012) show that if the regional maximum principal stress bisects the fault plane x with a small angle (such as low angle thrust faults), σ_{xx} is much larger than σ_{yy}, the normal stress ($\sim \sigma_{yy}$) is much smaller than the mean stress ($\sigma_{xx} + \sigma_{yy}$)/2, and a large Skempton coefficient results in high pore pressure larger than the normal stress. Therefore the effective normal stress change is negative and failure is promoted on the compressional side (Figure 4 in Viesca et al. 2008). However, in the case of the off-Sumatra earthquake, the maximum principal stress bisects the faults at 45 ° [*Delescluse et al* 2007], which means $\sigma_{xx} \sim \sigma_{yy}$, therefore the mean stress is similar to the normal stress. The effective normal stress remains

positive for reasonable values of the Skempton coefficient $B \sim 0.5$. The poroelastic effect limits the mean stress changes (coulomb stress increases on the compressional side and decreases on the dilatational side) and equalizes the probability of branching on both sides, but it does not favour the compressional branch. The preferred compressional branching might involve geometrical complexities and heterogeneous stress distribution that cannot be resolved by current observations. Nevertheless, even moderate Skempton coefficients ($B \sim 0.5$) relax the requirements for compressional branching by permitting positive coulomb stress changes at larger friction coefficients (Figure 4.3). In laboratory experiments, high Skempton coefficients ($B \sim 1$) are observed at low effective confining stress [*Paterson and Wong* 2005]. Given that the strength drop (the product of effective normal stress and the static to dynamic friction coefficient drop) is greater than the stress drop, $\Delta\mu \cdot \sigma_e > \Delta\tau \sim 13\ MPa,$ the effective normal stress σ_e is larger than 26 MPa even assuming a large friction drop $\Delta\mu = 0.5$. Based on the laboratory data summarized by Paterson and Wong (2005), the corresponding Skempton coefficient is limited to $B \leq 0.5$.

4.6. Discussion

We showed that compressional branching in almost orthogonal conjugate faults requires low friction coefficient and slow rupture speed, and is aided by the presence of fluids (poroelastic effect). However, the origin of low friction and the source of fluids remain to be identified. Meng Ampuero Stock et al. (2012) discussed a possible petrological origin of low friction based on serpentinization in the Indian ocean lithosphere [*Delescluse and Chamotrooke* 2007]. Serpentine is found to have a low friction coefficient in laboratory experiments [*Escartin et al.* 2001]. The dehydration embrittlement of the serpentine minerals due to shear heating can provide fluids and a weakening mechanism at depth [*Jung et al.* 2004]. The serpentine mineral antigorite is stable up to ~720 °C and 2

GPa [*Ulmer and Trommsdorff* 1995], which corresponds to about 40 km depth in our context. However, the serpentinization reaction is possible only up to 400-500 °C, which corresponds to about 25 km depth [*Delescluse and Chamot-Rooke* 2008]. The serpentinization might interact with downward fault growth through multiple earthquake cycles. These earthquakes are further facilitated by serpentinization and also create channels for deeper infiltration of fluids. The fault system is probably systematically activated by the megathrust earthquakes in the Sunda subduction zone, such as the 2004 Sumatra event. The centroid depth of the earthquake is around 30 km, implying that the rupture extends even deeper than 25 km, beyond the maximum depth where the serpentinization reaction is possible. The ductile shear heating instability [*Kelemen and Hirth* 2007; *McGuire and Beroza* 2012] operating between 40 and 60 km depth provides a weakening mechanism to explain the deeper slip. The gap between 25 and 40 km might be a frictionally stable region dragged along by the shallower and/or deeper rupture. Hillers et al. (2006) showed that ruptures can penetrate well beneath the nominal seismogenic layer into velocity-strengthening regions.

Our study highlights that the connectivity of rupture across multiple fault segments is a key factor of earthquake hazard. While the odds of a rupture involving multiple fault segments decreases quickly with the number of segments [*Wesnousky et al.* 2011], these extreme events often surprise us in most unexpected ways and places and cause the most significant damage. More efforts on estimating the possibility of earthquakes connecting segments are certainly needed in places like the San Andreas and New Madrid fault systems. Finally, this work demonstrates the importance of having fine observations to constrain earthquake source dynamics studies. Particularly, back-projection studies of recent large earthquakes demonstrate that large scale-arrays need to be maintained to image future large earthquakes. The Earthscope Global Array of Broad Band Arrays (GABBA) initia-

tive is one such effort to continue the source imaging capability beyond the end of the USArray project.

:

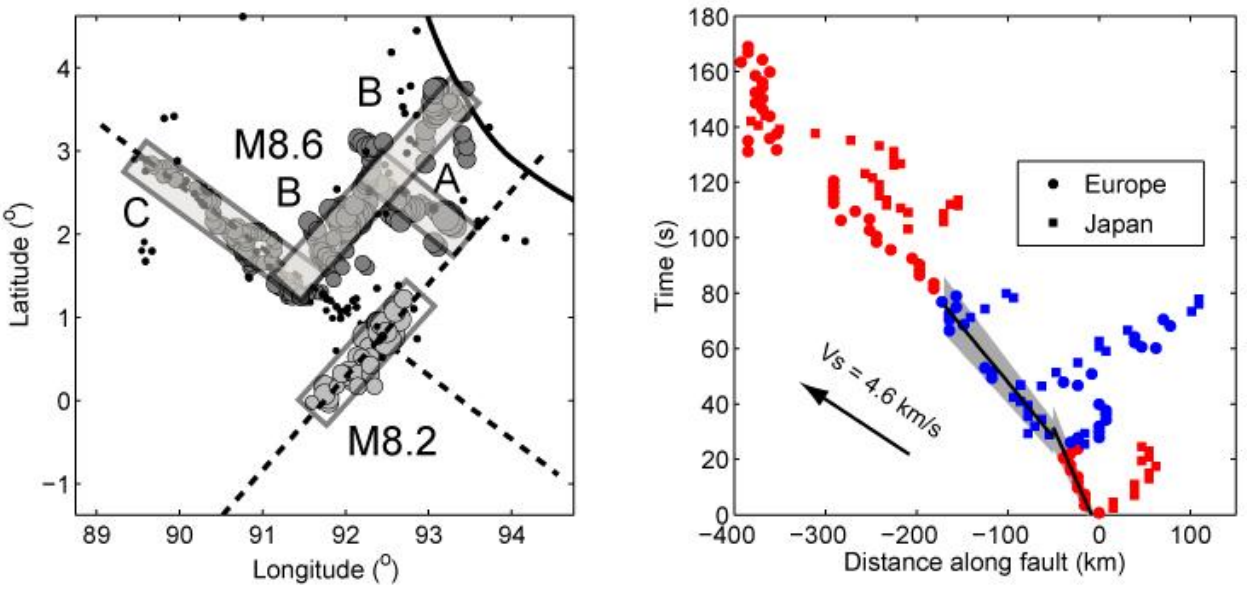

Figure 4.1. Uncertainty of the bisecting angle of the conjugate fault system (left) and the rupture speed (right) inferred from teleseismic back-projection source imaging. Left: the dark grey (mainshock) and light grey (M8.2 aftershock) circles indicate the positions of high-frequency radiation imaged with the Japanese Hi-net network. Their size is scaled by the beamforming amplitude. Black dots are the epicenters of the first day of aftershocks from the NEIC catalog. The black rectangles denote the fault planes A, B and C of the M8.6 mainshock and the fault plane of the M8.2 aftershock. The dashed lines are the linear-fit fault planes of the M8.2 aftershock and the late NW-ward rupture of the mainshock. The bisecting angle is 87°(84°~90°) based on one sigma variance of each fault plane. Right: The high frequency radiators imaged with European (circles) and Japanese (squares) networks as a function of distance along the rupture path (positive NW-ward on faults A and C (red), and SW-ward on fault B (blue)) and rupture time. The ratio of rupture speed to shear wave speed (4.6 km/s) along the NW branch of fault A and SW branch of fault B is 29% (25%~33%) and 55% (50%~60%), respectively.

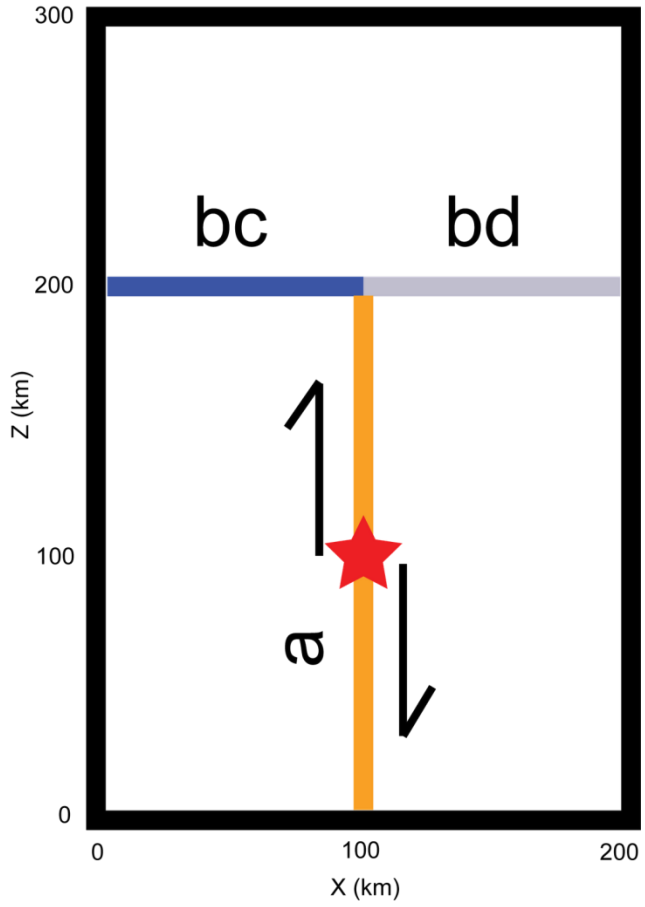

Figure 4.2. Sketch of the simulation setup. The yellow, blue and grey lines denote the initial right lateral fault **a** and the orthogonal branching fault segments **bc** (compressional) and **bd** (dilatational). The faults are embedded in a homogeneous elastic medium surrounded by absorbing boundaries. The red star is the hypocenter.

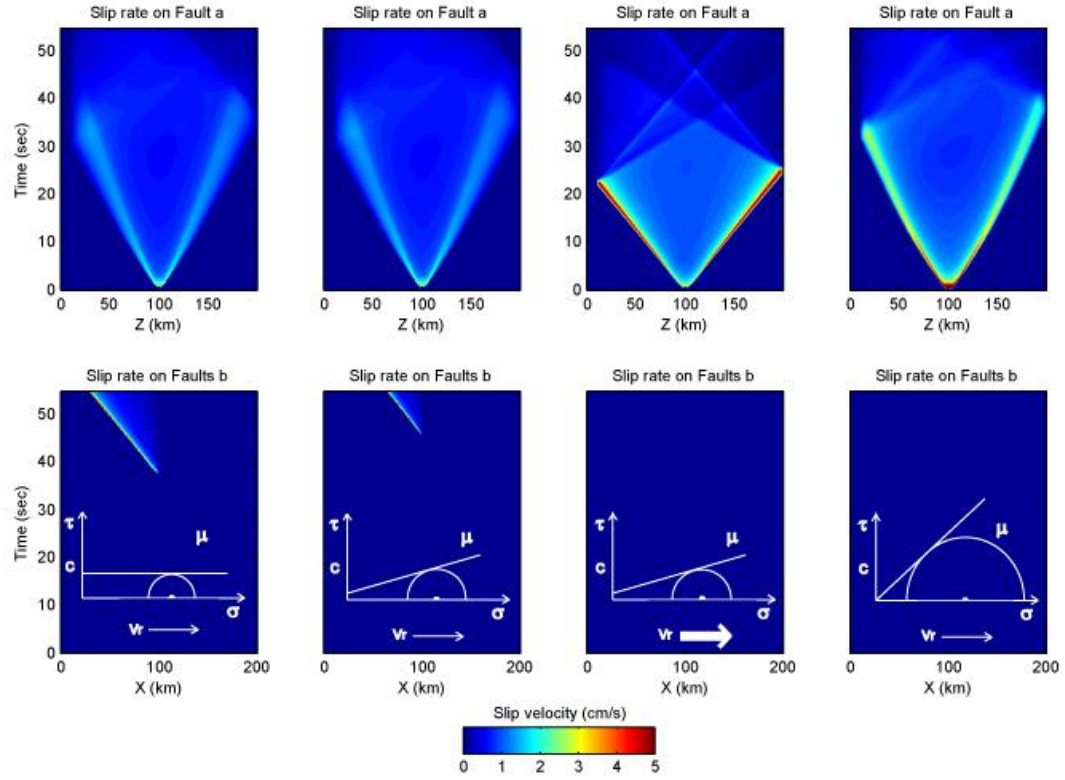

Figure 4.3. Spatiotemporal distribution of slip rate on the initial fault **a** and branching fault **b** for various models. a: slow and pressure insensitive, b: slow and weakly pressure sensitive, c: fast and weakly pressure sensitive, d: slow and strongly pressure sensitive. Insets in bottom plots show the failure envelope in shear strength (τ) vs. normal stress (σ) diagrams of the four models with different friction coefficient μ, cohesion C and rupture speed Vr.

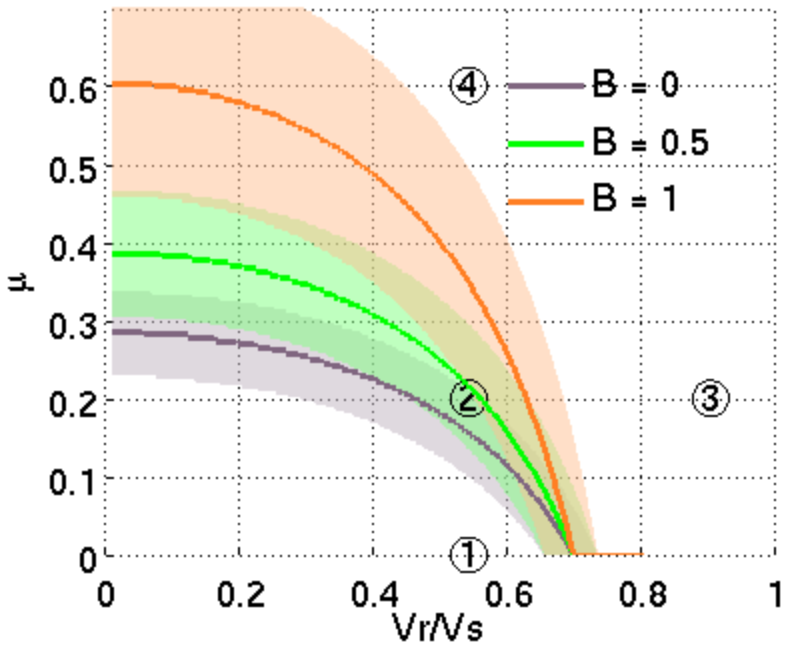

Figure 4.4. Maximum friction coefficient (μ) that allows compressive branching (positive dynamic Coulomb stress change near the rupture tip), as a function of rupture speed (Vr) and for three values of the Skempton coefficient B (see legend). The curves correspond to branching on an orthogonal fault, and the color bands encompass the range of fault orientations within the uncertainty inferred from the back-projection results (Figure 1). This analysis is based on analytical solutions for the dynamic stresses near a propagating rupture front (Poliakov et al. 2002). The numbers in circles indicate the parameters settings of the dynamic rupture models (with B = 0) shown in Figure 4.3, which confirm these analytical arguments.

Model index	μ_s	μ_d	C	σ_0	τ_0	Vr/Vs	$d\tau$	Dc’
1	0	0	38 MPa	250 MPa	38 MPa	0.54	13 MPa	2.2e-3
2	0.2	0.1	0	250 MPa	38 MPa	0.54	13 MPa	2.2e-3
3	0.2	0.1	0	250 MPa	38 MPa	0.89	13 MPa	6e-4
4	0.6	0.4	0	250 MPa	115 MPa	0.54	15 MPa	1.5e-3

Table 4.1. Parameters of the four models shown in figure 4.3

Chapter 5

HIGH-RESOLUTION BACK-PROJECTION AT REGIONAL DISTANCE: APPLICATION TO THE HAITI M7.0 EARTHQUAKE AND COMPARISONS WITH FINITE SOURCE STUDIES

Originally published in L. Meng, J.-P. Ampuero, A. Sladen and H. Rendon (2012), High-resolution back-projection at regional distance: Application to the Haiti M7.0 earthquake and comparisons with finite source studies. *J. Geophys. Res.*, 117, B04313.

Note: the supplementary materials are included in Appendix D.

5.1. Abstract

A catastrophic Mw 7 earthquake ruptured on January 12, 2010 on a complex fault system near Port-au-Prince, Haiti. Offshore rupture is suggested by aftershock locations and marine geophysics studies, but its extent remains difficult to define using geodetic and teleseismic observations. Here we perform the multitaper MUSIC analysis, a high-resolution array technique, at regional distance with recordings from the Venezuela National Seismic Network to resolve high frequency (about 0.4 Hz) aspects of the earthquake process. Our results indicate westward rupture with two subevents, roughly 35 km apart. In comparison, a lower frequency finite source inversion, with fault geometry based on new geologic and aftershock data, shows two slip patches with centroids 21 km apart. Apparent source time functions from USArray further constrain the intersubevent time delay, implying a rup-

ture speed of 3.3 km/s. The tips of the slip zones coincide with subevents imaged by back-projections. The different subevent locations found by back-projection and source inversion suggest spatial complementarity between high and low frequency source radiation, consistent with high frequency radiation originating from rupture arrest phases at the edges of main slip areas. The CMT solution and a geodetic-only inversion have similar moment, indicating most of the moment released is captured by geodetic observations, and no additional rupture is required beyond where it is imaged in our preferred model. Our results demonstrate the contribution of back-projections of regional seismic array data for earthquakes down to M ≈ 7, especially when incomplete coverage of seismic and geodetic data imply large uncertainties in source inversions.

5.2. Introduction

The M7 earthquake that hit Haiti in January 2010 was one of the most devastating natural disasters of the last decades. The disproportionate damage caused by this event and the prospect of future hazards in the region have prompted efforts to better understand its rupture process and the tectonics of the Northeast Caribbean, in particular the Enriquillo-Plantain-Garden Fault (EPGF) and the surrounding fault systems. Nettles and Hjorleifsdottir (2010) found that a composite source model with a strike-slip subevent followed by a smaller thrust subevent was consistent with long-period teleseismic data. Using geodetic data, Calais et al. (2010); Hashimoto et al. (2011) attributed the slip to two asperities on a previously unmapped fault in the Leogane delta, north from the EPGF. Based on the analysis of geodetic, geologic and teleseismic observations, Hayes et al. (2010) also inferred rupture primarily on the blind Leogane fault, with a minor contribution on the EPGF. One possible uncertainty about this event is the extent of its rupture in the offshore areas where it cannot be directly constrained by on-land geodetic data. In particular, this question became more of a concern

after the identification of active offshore deformation by a marine geophysical survey and by the refined location of aftershocks derived from a combined temporary seismic network of 4 land and 21 ocean bottom stations (Haiti-OBS campaign) [*Mercier de L épinay et al*. 2011].

While finite fault inversions provide possible source models, they rely on a priori information about the fault geometry, which is not readily available for the Haiti event due to the geological complexity of the fault system and to the lack of surface rupture [*Prentice et al.* 2010] and strong motion recordings. In addition, the source inversion problem suffers from limited resolution of the spatiotemporal rupture process due to its low frequency band. Source imaging by back-projection of body waves recorded by dense arrays allows tracking the areas of strongest high frequency radiation [*Ishii et al.* 2005; *Fletcher et al.* 2006; *Vallee et al.* 2008]. This technique constrains the spatio-temporal properties of the rupture (length, direction, speed, segmentation) based solely on the phase of coherent seismic array signals. Thus, it does not rely on detailed knowledge of Green's functions and fault geometry, on restrictive parameterizations of the rupture kinematics, nor on additional smoothing. The high frequency aspects of the rupture process imaged by array back-projection are complementary to traditional finite source inversion models based on teleseismic and geodetic data, which are instead sensitive to low frequencies and to the static field.

Conventionally, back-projection is applied to large seismic arrays at teleseismic distances [*Ishii et al.* 2005; *Meng et al.* 2011] or to small aperture strong-motion arrays at local distances [*Spudich and Cranswick* 1984; *Fletcher et al.* 2006]. Seismic arrays at regional distances can provide higher aperture to distance ratio and thus higher resolution. Vallee et al. (2008) exploited surface waves recorded by a regional array to study the 2001 Mw 7.8 Kunlun earthquake over a frequency band (0.04 to 0.1 Hz) adequate to study very long ruptures, but too low to resolve smaller earthquakes. In principle, higher frequency body waves carry higher resolution information. However, the complex-

ity of regional Pn waves has prevented seismologists from fully exploiting this phase for source imaging. Earthquake source studies using regional body wave phases have been mainly limited to inferring macroscopic source properties from recordings at distances up to a few hundred kilometers [*Zhu and Helmberger* 1996; *Mendoza* 2005; *Wei et al.* 2009]. *Guilbert et al.* (2005) imaged the rupture propagation of a very large event, the 2004 Mw 9.0 Sumatra earthquake, by array processing of body waves recorded by the CMAR-seismic array at regional distance. Here, we further show that the relatively sustained character of the Pn phase enables the application of high resolution array processing techniques on moderate earthquakes ($M \approx 7$) to provide complementary constraints on rupture length and locations of high-frequency source radiation. This capability can contribute to rapid hazard and damage assessment for future earthquakes in the Caribbean region.

The rest of this article is organized as follows. In section 2 we describe the data recorded by Venezuela National Seismic Network and argue for the need of high resolution regional array analysis. In section 3 we present a high resolution array source imaging technique adapted to earthquakes recorded at regional distance and quantify the resolution of the technique through extensive synthetic tests. In section 4 we present our results of source imaging of the Haiti earthquake by regional array analysis. In section 5 we integrate these results with independent analysis of apparent source time functions based on USArray data and an improved finite fault model based on teleseismic and geodetic data. In section 6 we discuss the rupture speed, the frequency-dependent source properties, the possibility of offshore coseismic rupture and the potential contribution of regional arrays to earthquake studies.

5.3. VNSN data, preprocessing and selection

Our array back-projection study of the 2010 Haiti event is based on data recorded at regional distance by the Venezuela National Seismic Network (VNSN). The VNSN is composed of 22 broadband stations, oriented mainly East-West, and located approximately 9.5 ºfrom Haiti in the perpendicular direction to the EPGF strike (Fig. 5.1). The VNSN has a suitable geometrical configuration and location to study large earthquake ruptures in the Caribbean region.

Array processing at regional distance aims at estimating the azimuth of arrival and relative timing of the seismic phases radiated from the strongest subevents of the earthquake. The study of the 2010 Haiti earthquake remains challenging because of its compact source size, shorter than 40 km according to previous studies [*Calais et al.* 2010; *Hayes et al.* 2010]. The resolution length scale along the fault that can be achieved with the standard beamforming techniques is evaluated by the array response function [*Rost and Thomas* 2002]. Figure 5.2 shows the array response of the VNSN and the USArray, the nearest array at teleseismic distance. The array responses are back-projected into the hypocentral region of the 2010 Haiti earthquake based on P travel times computed by the Tau-P toolkit and the IASP91 model [*Snoke* 2009]. The array response of VNSN is not isotropic. It has low resolution along the range direction (the source-to-array direction) but adequate cross-range resolution (subparallel to the fault strike in this case). In regional array processing, the range resolution is considerably poorer than the cross-range resolution, due to the small variability of the slowness of Pn waves as a function of epicentral distance. Hence, we compute the maximum of the array analysis result along lines parallel to the major axis of the array response pattern. Then these maxima are mapped onto the fault trace and plotted as a function of along-strike position. The along-strike resolution length achieved by the USArray is approximately twice of that of the VNSN due to its more distant location and its more unfavorable orientation with respect to the fault strike. We note that the array response provides an ideal estimate of the array resolution. In practice, resolution is further affected by waveform incoherence and interference, as discussed through synthetic tests in

section 3.2. Thus, to achieve adequate imaging of the Haiti earthquake the back-projection requires data from an array at regional distance. Moreover, since previous studies [*Hayes et al. 2010; Calais et al. 2010*] indicate that the rupture length of the Haiti earthquake is as compact as 40 km, the analysis requires an array processing technique that can achieve higher resolution than standard beamforming.

The Pn waveforms recorded by the VNSN are filtered between 0.2 and 0.7 Hz. The low frequency cutoff is dictated by a time-frequency trade-off (see section 3.1). The high frequency cutoff is determined by the coherency of the array data, which is ultimately determined by the spacing between stations. The dominant frequency of the Pn waves is about 0.4 Hz. We align the waveforms on their first arrival by multichannel alignment [*Vandecar and Crosson* 1990] based on cross-correlation of 10 seconds long windows containing the first Pn arrivals. This procedure reduces the effect of travel- time errors due to uncertainties in the velocity structure, e.g., Ishii et al. (2005).

Array processing techniques assume coherent signals across the array. We select a subset of 13 stations with adequate waveform coherency by inspecting the array data coherence matrix. This matrix is made of the coherence between all pairs of stations computed during the multi-channel alignment procedure. The indices of the matrix are reordered to group together the most mutually coherent stations (Fig. 5.3). We found a modified k-nearest neighbors clustering algorithm (www.eigenvector.com/MATLAB/Mac_Mfiles/corrmap.m) to be adequate for this purpose. After inspection of the reordered matrix we select a subset of 13 stations that consistently have correlation coefficients larger than 0.8 (Fig. 5.3).

5.4. High Resolution Multitaper/MUSIC Technique for Regional Arrays

5.4.1. Outline of the Method and Parameter Settings

Here, we apply at regional distance a high-resolution array analysis technique originally developed for a teleseismic array study [*Meng et al.* 2011]. The method combines the Multiple Signal Classification (MUSIC) array processing technique [*Schmidt* 1986; *Goldstein and Archuleta* 1991; *Guilbert et al.* 2005] with multitaper cross-spectrum estimation [*Thomson* 1982]. MUSIC was designed for high resolution direction of arrival estimation of long and stationary signals [*Krim and Viberg* 1996]. The Pn phase is relatively stationary. The multi-taper method yields a robust estimate of the data coherence matrix on relatively short time window and thus improves significantly the temporal resolution of MUSIC. Here we only describe the choice of processing parameters for this particular study. More details about the method are described by Meng et al. (2011).

Number of Tapers in Cross-Spectrum Estimation

The multi-taper technique [*Thomson* 1982] averages multiple, almost independent cross-spectral estimates obtained after tapering the data by a sequence of orthogonal functions with optimal temporal and spectral concentration. These Slepian tapers are the set of functions of finite temporal duration T with maximum energy within the band of frequencies lower than the bandwidth W. Given a time window duration T and a frequency bandwidth W, the proper number of tapers is $2 \times T \times W - 1$. As a compromise between useful averaging (large $T \times W$) and adequate temporal resolution (short T) we use here 3 tapers, which implies $T \times W=2$.

Length of Analysis Window

The MUSIC method requires narrow band estimates of cross-spectrum, i.e., the bandwidth W (the frequency smearing of the spectral estimator) has to be small compared to any frequency of analysis, W << f. This implies a trade-off between temporal resolution and frequency localization: $T \times f >> 2$ for 3 tapers. As a compromise here we set T = 30 s, which satisfies $T \times f > 6$ for frequencies higher than 0.2 Hz. At the dominant frequency of our data, $f \approx 0.4$ Hz, we get $T \times f \approx 12$.

Number of Principal Eigenvalues

In MUSIC the signal subspace is defined as the subspace spanned by the distinctly largest eigenvalues of the data covariance matrix. Its complement defines the noise subspace. For stationary signals, the dimension N of the signal subspace is equal to the number of signal sources contributing to the data time window. In the case of transient seismic signals analyzed with relatively short time windows, each covariance matrix estimated with a separate taper tends to have only one nonzero eigenvalue and the associated eigenvectors tend to be independent. Hence, the rank of the covariance matrix obtained by linear combination of the multiple taper estimates tends to be equal to the number of tapers. In particular, the number of significant eigenvalues is at most three when using three tapers. Fig. 5.4 shows results of the MUSIC analysis of the 2010 Haiti earthquake at 0.4 Hz, the dominant frequency of the seismograms, with N ranging from 1 to 4. The MUSIC pseudospectrum, a measure of the orthogonality between the array steering vector associated to a candidate source location and the noise subspace (for details see Meng et al. 2011), is plotted as a function of along-strike position with respect to the hypocenter and as a function of end time of the sliding windows. The MUSIC pseudospectrum is normalized by its maximum in each time window. Its amplitude depends on signal power, coherence and interference but it does not directly represent any physical quantity. Nevertheless, the sharp peaks of the MUSIC pseudospectrum indicate the location of signal sources. In the MUSIC analysis of the Haiti earthquake, two main subevents (black dots in Fig.

5.4b) are visible and their estimated locations are independent of the choice of N. However, when N is too small (N=1) the analysis fails to resolve two simultaneous sources. It only indicates the strongest source in each time window. The results with N=2 or 3 show stable features of the rupture process including simultaneous multiple sources. When N is larger than the number of nonzero eigenvalues (e.g., N=4), the signal subspace is contaminated by noise and the resulting image is not stable. While the spatial location of the subevents is independent of the choice of N, their estimated timing is not. Because we have not developed yet a complete understanding of the effect of N on the timing of subevents, an objective rationale for the choice of N is not available at this time. Here we choose N=2 because it yields the most clear image of the westward rupture front and the resulting rupture speed is within the usual range, consistent with independent observations available for this earthquake, as described in later sections. We note, however, that the temporal details of the back projection images, which depend on N, are not used as additional constraints to infer the rupture speed of this earthquake. Because of the normalization, the MUSIC pseudospectrum in Fig. 5.4 persists for a long time and reflects the sustained Pn phase rather than the source duration.

5.4.2. Resolution Tests

Synthetic Test for an Ideally Coherent Linear Array

Fig. 5.5 compares the resolution of four techniques on synthetic transient signals: and MUSIC, beamforming, cubic root stacking (a popular modification of beamforming, e.g., Rost and Thomas 2002), and correlation stacking. In correlation stacking the normalized cross-correlation coefficients are beamformed instead of the waveforms [*Fletcher et al.* 2006] to improve robustness against scattering, multipathing and contamination by coda waves [*Borcea et al.* 2005]. The color scale in the images by correlation stacking and cubic root stacking indicate beamformed cross-correlation coefficients and beamformed cubic root of the signal amplitude, respectively, evaluated or integrated

over a sliding time window of duration 30 s. The resolution of a method is defined as its ability to separate closely spaced sources. We consider two identical Pn plane waves with dominant frequency of 0.3 Hz impinging simultaneously but with different azimuth on a linear array of 21 sensors regularly spaced at half wavelength. Gaussian white noise is added with a signal to noise ratio of 10 dB. The results as a function of the relative azimuth between the two waves (Fig. 5.5) show that, the minimum azimuthal separation resolvable by MUSIC, beamforming, cubic root stacking, correlation stacking and is approximately 3, 8, 8, and 8 degrees, respectively. This shows that, under perfect waveform coherency, the azimuthal resolution, and hence the spatial resolution in the cross-range direction, achieved by our multitaper MUSIC method outperforms the other methods by at least a factor of two.

Synthetic Test for the VNSN Array Geometry

Fig. 5.6 shows further synthetic tests to understand the performance and potential bias of the back projection of the Haiti earthquake source using the VNSN data. We compute full wave field synthetics (Fig. D.1) using the SPECFEM3D package [*Tromp et al.* 2008] with the 3D crustal velocity model Crust2.0 [*Bassin et al.* 2000]. Our simulations are accurate up to 0.33 Hz. Given the uncertainties in the velocity model, generating higher frequency synthetics is not warranted. Inspired by the final result of the back projection, we test scenarios with a source containing two asperities. The first one is located at the hypocenter of the Haiti earthquake. The second one is located westward along the hypothetical Leogane fault trace [*Hayes et al.* 2010]. We consider either the same slip amplitude for both subevents or a 2:1 ratio based on the source time functions estimated at the USArray (see section 5.1). We explore intersubevent distances up to 50 km, with rupture time delays consistent with a rupture speed of 3 km/s. For both asperities we assume source parameters from the CMT solution (focal mechanism 251/70/28, strike/dip/rake, and centroid depth 12 km) and

a Brune source time function with duration of 3 seconds. In Fig. 5.6, the left two columns show examples of cubic root stacking, correlation stacking and MUSIC pseudospectra. These quantities are back-projected onto the source area based on P travel times computed by the Tau-P toolkit and the IASP91 model [*Snoke* 2009].

We found that all the back-projection methods are modulated by interference between subevents. This introduces an amplitude and location fluctuation that depends periodically on the product of intersubevent time delay and frequency of analysis. At some distance, the second subevent is recovered well, but not at some other distances, depicted as multiple horizontal bars in right two columns of Figure 5.6. Fig. 5.7 shows two examples of interference in the cubic root stacking analysis at 0.3 Hz, with sources separated by 15 and 40 km respectively. The time delay between the wave arrivals from the two asperities varies across the array. Destructive interference occurs at stations where the waves from the two asperities are out of phase with respect to the dominant period (the seismograms of some stations are deficient in low frequencies in Fig. 5.7). This interference results in incorrect imaging of two sources (left columns in Fig. 5.7). This issue might be less severe in practice, since the synthetics are computed from two point sources. In reality, the broader slip region reduces the simultaneous destructive interference.

As expected from the resolution test, MUSIC achieves a smaller resolvable distance than the other two techniques. This difference is particularly prominent when we set a more realistic 2:1 amplitude ratio for the two sources. The left two columns in Figure 5.6 show the two snapshots taken at 30 s long time windows ending at t=15 s and t=30 s when d=30 km. At t=30 s, the window includes the simultaneous signals from both events. While the MUSIC pseudospectrum clearly gives two peaks in the second snapshot, the other two techniques fail to resolve them. Note that the absolute amplitude of the MUSIC pseudo-spectrum, which is modulated by interference patterns, does not directly

represent the signal power and is not used in the analysis. The resolution limit for MUSIC in these synthetic tests is approximately 25 km (the distance beyond which we can separate two sources) with an uncertainty of about 5 km for each subsource. Because the interference effect is less prominent in actual data since they are generated by distributed sources instead of point sources, we consider 25 km and 5 km are safe estimates of the resolution limit and the relative location uncertainty in our analysis.

5.5. Results of Array Analysis of the 2010 Haiti Earthquake at Regional Distance

We first illustrate the accuracy of our method by an analysis of the largest aftershock, a M 5.9 (NEIC) earthquake on January 20, 2010 (waveform shown in Fig. 5.8). The back-projection of the MUSIC pseudospectrum into the source region is shown in map view in Fig. 5.8a and 5.8b for two windows ending at t=15 s and 30 s after the first arrival, respectively. The warmest color indicates the location of the source of the waves arriving at the VNSN within these time windows. As explained in section 2, the back-projected contours are very elongated in the source-array direction. Our analysis provides accurate source location only in the perpendicular direction, which is sub-parallel to the EPGF strike. We hence extract the maximum of the MUSIC pseudospectrum along lines parallel to the source-array direction, then project these maxima onto the EPGF trace. Note that this aftershock has a slightly different strike (N 290 °) than the EPGF (N 255 °) but this difference is minor for this magnitude. Fig. 5.8c shows this quantity as a function of epicentral distance along the EPGF strike and of final time of the sliding window. This result indicates that the aftershock is properly imaged as a compact source of 5 km size near its hypocenter. This distance could either be the dimension of the source [*Wells and Coppersmith* 1994], or the spatial uncertainty of the source location. In either case, it suggests little spatial smearing in our analysis at the 5km scale and warrants imaging of the mainshock, which is possibly composed of multiple subevents.

Fig. 5.9 shows the results of our application of MUSIC to the VNSN recordings of the 2010 Haiti mainshock. We also applied two other popular array techniques, cubic-root stack and correlation stack with the same stations set and frequency band, shown in Figs. 5.9a and 5.9b respectively. Although all these array analysis techniques unambiguously indicate two prominent subevents, our multitaper-MUSIC algorithm provides the images with the sharpest contrast between the subevents and the adjacent areas, as expected from our synthetic tests. Note that the peak locations of the MUSIC imaging are off the fault trace, to the south, due to limited resolution along the source-array direction at regional distance, which highlights the importance in regional array processing of a projection along the source-to-array direction onto the fault trace. The first subevent is located approximately 5.4 km east from the hypocenter. This distance is obtained by fitting a constant location to the peak location of the first event measured after the estimated location is stabilized (t = 15 s) and before the second subvevent becomes dominant (t = 27 s). The second subevent is approximately 35.7 km further west (30.3 km west from the hypocenter) based on the peak locations of the second suvevent measured after t = 27s. This complexity is absent in the results of our analysis of the M5.9 aftershock (Fig. 5.8) and hence is not due to path effects or other phases. The temporal evolution is better imaged by array processing at the peak frequency (0.4 Hz). In Fig. 5.4-b, bilateral propagation is observed starting around t = 10 s, when the last 10 s of the 30 s window contain the signal. The eastward front runs for about 10 km in about 3 s. The westward front shows a weaker MUSIC pseudospectra but its propagation can be consistently tracked over a distance of ~35 km and a duration of about 10 s (until t ≈ 20 s). The rupture speed of both fronts is similar and consistent with usual subshear rupture speeds, given the shear wave speed of 3.65 km/s at 10 km depth in the Haiti region [*Bassin et al.* 2000]. These estimated subevent locations are consistent with the array analysis at the peak frequency of 0.4 Hz (Figure 5.4), although for the sake of robustness, the average over frequency band 0.2 ~ 0.7 Hz (Figure 5.9) is presented as our main result. The observed features

are also compatible with the USArray source time functions and finite fault inversions described in the next section.

5.6. Comparison to Independent Observations

Our study is the first example of earthquake source imaging at regional distance with Pn waves for earthquakes of magnitude as low as 7. To build confidence in our results, we compare them here to other available observations. The complementarity between the different source analysis techniques provides an integrated view of the 2010 Haiti earthquake rupture process.

5.6.1. Source Time Functions at USArray

The temporal separation between the two asperities is independently estimated from apparent source time functions obtained through deconvolution of teleseismic data by theoretical Green's functions (Fig. 5.10) [*Chu et al.* 2009]. We selected USArray stations with epicentral distances greater than 30 degrees to avoid complexities of the P waveform due to triplication in the upper mantle. We computed synthetic Green's function using the generalized ray theory [*Helmberger* 1983], the IASPEI91 1D global velocity model [*Kennett and Engdahl* 1991] with the upper 30 km adjusted to a 4-layer Haiti regional crust model [*Bassin et al.* 2000] and the CMT solution (www.globalcmt.org). The vertical component P waveforms and synthetic Green's functions are filtered from 0.01 to 1Hz and deconvolved in the time domain with the iterative technique of Kikuchi and Kanamori (1982) and with the nonnegative least squares algorithm [*Lawson and Hanson* 1974]. Both deconvolution techniques yield consistent results. To estimate the temporal separation between the subevents and its uncertainty, we considered 1000 stacks of randomly selected subsets containing 90% of the USArray stations. We measured the delay between the two prominent peaks

in the stacked apparent source time functions. We allow a 5 s range when estimating the timing of the second peak. Although some of the individual curves are noisy and bumpy, the bootstrapped stacked curve is smooth and robust. The estimated delays have a Gaussian distribution with mean t_1=5 s and standard deviation 0.02 s (Fig. 5.10). We associate these with the two subevents found by our array analysis. The deconvolution analysis also indicates that the second subevent accounts for approximately one third of the total moment release, consistent with the multiple CMT solution of Nettles and Hjorleifsdottir (2010). Their analysis also indicates that the second subevent has a thrust mechanism, in contrast to the near strike-slip mechanism of the first subevent. Nevertheless, at the azimuth of the USArray both mechanisms produce similar amplitudes and our choice to use the CMT solution to generate the Green's functions does not introduce a significant bias.

5.6.2. Improved Finite Fault Model

To evaluate how the results of the back-projection and USArray analysis of the source time function relate to other data sets and integrate in the global description of the rupture, we perform a joint source inversion based on teleseismic body waves and the various geodetic data available.

As detailed in previous studies [*Calais et al.* 2010; *Hayes et al.* 2010; *Hashimoto et al.* 2011], the campaign GPS measurements and InSAR data provide a very good coverage of the Leogane delta where the rupture started and indicate that the deformation in this area is best explained by a fault segment dipping NNW. In agreement with those studies, we choose a fault strike of 254 °and a dip angle of 55^0. This orientation of the fault plane is also compatible with the alignment of aftershocks along a N75^0 azimuth [*Mercier de Lépinay et al.* 2011]. InSAR fringes (ALOS ascending track 137) and field measurements of the coastal vertical uplift in the area near the town of Petit Goave [*Hayes et al.* 2010] suggest the earthquake also extended west and offshore of the Leogane delta. This hypothesis is supported by the aftershock catalog obtained from the Haiti-OBS local network

of terrestrial and ocean-bottom seismic stations [*Mercier de Lépinay et al.* 2011]. In contrast with previous models, we do not cover this offshore area by simply extending the preferred Leogane fault geometry (i.e., dipping NNW) to the west, but refine the model with a distinct second fault segment dipping 45^0 to the NNE (strike $N275^0$). This NNW to NNE rotation in the fault strike is supported by the moment tensors of the aftershocks [*Nettles and Hjorleifsdottir* 2010] and by the identification of bathymetric features with a similar orientation, such as the Trois Baies fault and the Transhaitian belt [*Mercier de Lépinay et al.* 2011].

The location of the NEIC epicenter is incompatible with our first fault segment as it would imply a very superficial rupture initiation (~2 km), and would not be compatible in terms of depth: the NEIC depth is fixed to 13 km by their location program. Moving the hypocenter in the northeast direction, as suggested by the higher resolution Haiti-OBS aftershocks catalog (when compared to the NEIC catalog) [*Mercier de Lépinay et al*. 2011], brings the rupture initiation closer to the zone of high slip, as we would expect from the hand-picked P wave onset and assuming a standard rupture velocity (~ 3 km/s) at initiation (Fig. D.2). Note that using the hypocenter located by Mercier de Lépinay et al. (2011) (72.499^0 W, 18.517^0 N, 12 km deep) does not affect the array analysis other than by shifting the MUSIC subevents locations by a similar amount.

The finite fault inversion is based on a Monte-Carlo type algorithm [*Ji et al.* 2002] and uses teleseismic data (21 P waves and 13 SH waves band pass filtered between 2 and 100 s), campaign GPS (data processing detailed in Calais et al. 2010) and four InSAR images (data selection and processing detailed in Hayes et al. 2010). We allow the rupture speed to vary from 3.0 to 3.6 km/s, that is +/-0.3 km/s around the rupture velocity inferred from the USArray analysis. We do not apply any minimization criteria on the seismic moment.

We obtain a slip model composed of two high slip patches, a first one centered on the epicenter and a second one with peak slip amplitude 21 km further west, starting 6 s after the onset of rupture (Fig. 5.11). The data misfit in our updated model (Table D.1) is comparable to previous studies [*Calais et al.* 2010; *Hayes et al.* 2010; *Hashimoto et al.* 2011]. While the fit of the InSAR data is excellent (Fig. D.3 and D.4), the fit of the GPS data is of moderate quality (Fig.5.11): this is mainly due to the large misfit at station DFRT which, despite having one of the largest measured displacements (0.7 m measured in the center of the deformation area), cannot be adjusted either in azimuth or amplitude. At the location of station DFRT, ascending and descending InSAR tracks are too decorrelated to do a comparison of the 3D displacement. However, the smooth 3D pattern of deformation inferred from InSAR in the surrounding areas [*Hayes et al*. 2011] suggests that motion at DFRT is indeed affected by localized deformation. Calais et al. (2010) who also used InSAR and GPS data could not fit properly station DRFT. The vertical deformation along the coast was measured using coral data [*Hayes et al*. 2010]. Since most of those measurements are within the area where InSAR coverage allows one to estimate the vertical motion (overlap of ascending and descending tracks) we did not include them in the inversion and only made sure that they are compatible a posteriori. The compatibility is verified for all points (inset in Fig. 5.11) except one subsidence measurement west of the surveyed area and the easternmost point. In the case of the subsidence point, the fact that this point moves down when the surrounding points move up suggests that it represents a local effect, perhaps a local slump similar to what is described by McHugh et al. (2011) and Mercier de L épinay et al. (2011) in the offshore survey of this area. The easternmost surveyed point (inset in Fig. 5.11) is inconsistent with the InSAR data (Fig. 2 in Hayes et al. 2010) and therefore cannot be fit properly. We note however that this area corresponds to the eastern end of the rupture where the uplift pattern decrease rapidly to zero (from +30 to 0 cm in less than 5 km, Fig. D.5) and never goes below -10 cm. Thus, the predicted surface deformation is consistent with the

observation of no vertical motion east of the rupture (0 to -10 cm of subsidence is within the error bar of the coral measurements).

Slip reaches a maximum of 10 meters (Fig. D.6) at the center of the first patch (7 m for the second patch) which concentrates two thirds of the total moment ($3 \times 10^{+19}$ Nm for the first patch, $1.5 \times 10^{+19}$ Nm for the second). This result is similar to our analysis of the USArray data. In term of bulk parameters, we also find that the moment tensor of our solution (Fig. 5.11) and its seismic moment ($4.5 \times 10^{+19}$ N.m) are similar to the CMT analysis [*Nettles and Hjorleifsdottir* 2010]. The teleseismic data bound the duration of the source time function to less than 15 s and indicate that the first patch of slip was more impulsive than the second and smaller slip episode. The oblique rake along the rupture is consistent with the transcompressional regime in this region [*Mercier de Lepinay et al.* 2011] but does not support the hypothesis of a fully partitioned fault system where the EPGF would absorb the entire strike-slip component [*Dixon et al.* 1998; *Calais et al.* 2002].

5.7. Discussion

5.7.1. The Rupture Speed

The rupture speed can be reliably constrained by the apparent subevent delay of t_1=5 s and by the spatial subevent separation of 21 km between the two subevents centroids provided by our geodetic-only slip inversion in Fig. D.7. Considering a bilateral rupture, the real intersubevent time delay is $t_0 = t_1 + \cos\theta\,(L_w - L_e)/c$, where θ is the angle between the fault strike and the source-array direction (40 °), c is the apparent P-wave speed (12 km/s at epicentral distance of 40 degrees), L_w and L_e are the distances of the centroid of the westward and eastward subevents, respectively (L_w = 21 km and L_e = 0 km). This yields a true intersubevent time of 6.3 seconds. The implied rupture speed, 3.3 km/s, is within the usual subshear range. For reference the shear wave speed is 3.65 km/s

at 10 km depth in the Haiti region [*Bassin et al.* 2000]. Although our regional array back-projection analysis currently has large uncertainties on the rupture timing (see section 3.1), our back-projection result at the dominant frequency, 0.4 Hz (Fig. 5.4-b), is consistent with this sub-shear rupture speed.

5.7.2. Spatial Complementarity Between High and Low frequency Source Properties

The primary results from the array analysis, the finite fault inversion and the source time function analysis suggest that the rupture propagates bilaterally with primary westward rupture and minor eastward component, breaking two main slip patches. In the finite fault inversion, dominated by frequencies lower than 0.2 Hz, the first asperity is located near the epicenter and the second one is 21 km west and contributes one third of the total seismic moment. On the other hand, the higher frequency radiators imaged by the array analysis (0.2-0.7 Hz) suggest a distance of 35 km between the two asperities.

Since the back-projection provides subevent locations relative to the hypocenter, the choice of epicenter is essential in interpreting the result of the array processing. Assuming the epicenter given by NEIC, the subevent locations are consistent with the spatial pattern of the aftershocks (NEIC catalog), which cluster into two groups. The eastern group is close to the mainshock epicenter and the second group is located 30 to 40 km west. If we assume the NEIC hypocenter, the western subevent is well beyond the high slip patches derived from the finite fault model, implying possible slip further west offshore, unconstrained by geodesy. However, if we take the hypocenter adjusted by Mercier de Lépinay et al. (2011) using local data instead of the NEIC location, the two HF subevents coincide with the terminal edges of the large slip areas. If we use the original NEIC hypocenter, the

difference of the HF event and the peak slip zone is less obvious for the eastern asperity but still holds for the western asperity. This type of spatial complementarity between high and low frequency source properties was inferred for several other earthquakes, including the 1989 Loma Prieta earthquake, the 1993 Kushiro-Oki earthquake [*Nakahara* 2008] and the 2011 Tohoku-Oki earthquake [*Ide et al.* 2011; *Meng et al.* 2011; *Simons et al.* 2011]. This complementarity can be interpreted as high frequency radiation generated by the stopping phases, associated with abrupt rupture speed reduction at the edge of the slip area. This mechanism of high-frequency radiation was first described in circular crack models [*Madariaga* 1977; 1983] and was explained for general rupture front geometries through isochrone theory [*Bernard and Madariaga* 1984; *Spudich and Frazer*,1984]. This interpretation is also consistent with the aftershock locations clustering at the regions of stress concentration at the edges of the coseismic rupture. Although the "stopping phase" interpretation is plausible for this particular earthquake, the generalization to other earthquakes is not warranted. Regardless of the mechanical origin of the high frequency radiation, the back projection analysis indicates its location. This is of practical importance for earthquake damage assessment. Note that the high frequency radiation is absent at the western end of the first asperity, implying a smoother stopping or rupture transition without stopping between the two asperities.

5.7.3. Extent of the Offshore Rupture

One aspect of the 2010 Haiti earthquake that still remains to be elucidated is the extent to which the rupture propagated offshore. Previous studies did infer offshore faulting [*Calais et al.* 2010; *Hayes et al.* 2010; *Hashimoto et al*. 2011; *Mercier de Lépinay et al*. 2011] but these models did not use all the currently available data sets to constrain the slip extent and/or the fault geometry onto which slip should be projected. Taking into account all these data, we investigate the possibility that the rupture extended further offshore than previously thought. In particular, observations in the offshore

region are suggestive of rupture extending further west than previously published source models. Marine seismic reflection profiles indicate the existence of a large scale active anticline associated with the Trois Baies fault and the Transhaitian belt [*Mercier de Lépinay et al.* 2011]. The aftershock locations derived from the Haiti-OBS campaign are offset by about 20 km NE relative to the NEIC catalog locations [*Mercier de Lépinay et al.* 2011], implying that the western aftershock cluster is not onland but offshore. The Haiti-OBS catalog also confirms the existence of a cluster of aftershocks more than 30 km west of the epicenter, 10-20 km beyond the western end of coseismic slip of previous source models.

While there are no direct offshore geodetic measurements to constrain the western end of the rupture, InSAR and GPS data cannot be properly explained by on-land faulting alone. The displacement vector of GPS station LEOG strongly points offshore and west of the Leogane delta (Fig. 5.11) despite the existence of an asperity east of that point (this asperity is directly visible in the descending InSAR track 447). The dense InSAR fringes of acending track 137 (Fig. D.4) surround the coastline pointing to deformation in the center of the bay.

In our kinematic source inversion based on teleseismic and geodetic data, slip is allowed to spread over more than 45 km west of the hypocenter (= maximum source duration × maximum rupture speed = 15 × 3 km). However, in the resulting model the slip remains confined to less than 22 km west of the epicenter. We obtained a similar slip distribution in a finite fault inversion based only on the static data sets, InSAR and GPS (Fig. D.7 and D.8) without constraint on the seismic moment, with comparable fit to the data (Fig. D.9 and D.10) and with a seismic moment ($5.0 \times 10^{+19}$ Nm) very close to the CMT solution ($4.7 \times 10^{+19}$ Nm). Moreover, the InSAR fringes along the coast (tracks A138a and A447d in Fig. D.10) tend to rotate slightly perpendicular to the western end of our slip model, which suggests that there are no regions with larger slip further west.

In summary, several arguments indicate that our preferred slip model did not miss any significant offshore deformation to the west. This result is consistent with the previously published models even though those models relied on different fault geometries. The spatial resolution of our regional back-projection is too coarse in the source-to-array direction (NNW-SSE) to provide an independent constrain on the distance between the coast and the second high-frequency source. However, the position of this second source along the cross-range direction (subparallel to the EPGF strike) is well constrained and is shown here to be consistent with the western end of offshore slip inferred from static deformation. This supports the idea that back-projection source imaging can identify the end tips of a rupture.

5.7.4. Advantage of Regional Array Back Projection for Earthquake Source Studies

Our study of the 2010 Haiti earthquake demonstrates that back-projection of P-waves recorded at regional distances can reveal the location of high frequency source radiation that is not resolvable by finite source inversions at teleseismic distance, which are now common practice. This new capability, improved by our analysis procedure combining multitaper and MUSIC techniques, allows us to study the rupture of earthquakes with magnitude as low as 7 providing reliable spatial constraints. The approach requires that the approximate strike of the fault is known, but this information can usually be reliably extracted from the focal mechanism of the event. This implies that regional back-projection will be critical in the study of earthquakes when geodetic coverage is incomplete or local seismic networks are lacking, for instance in subduction zones. Moreover, the procedure can be automated for rapid, possibly real-time, earthquake analysis, combining the fault strike information from fast moment tensor inversions. In that sense, the VNSN alone has a great potential for the analysis of earthquake hazard for the whole Caribbean-North America plate boundary. The high frequency aspects of the source process derived from array back-projection are particularly useful to

estimate potential damage in regions where the vulnerable components of the building stock are dominated by low rise (short period) buildings. In a more global perspective, the statistical analysis of the last 120 years of earthquakes demonstrates that most of the devastating earthquakes occur in continental interiors on previously unmapped faults [*England and Jackson* 2011]. Thus, with the ongoing development of regional seismic networks, many of those devastating earthquakes will still happen at regional distance from networks, and require the resolving power of regional back-projection.

5.8. Conclusions

In this study, we developed a back-projection source imaging technique for body waves recorded by seismic arrays at regional distances (Pn waves). The technique combines the Multiple Source Classification (MUSIC) method with multitaper cross-spectral estimation to achieve sharper source imaging than existing methods. This technique allowed us to extract key aspects of the rupture process of the 2010 Haiti earthquake from recordings by the Venezuela National Seismic Network (VNSN). In particular, it provides the locations of high frequency source radiation. When integrated with independent studies based on teleseismic and geodetic data of this earthquake, our results indicate bilateral rupture at subshear speed, with a much longer rupture segment toward the west. Prominent high frequency radiation originates from rupture arrest phases at the tip of the main slip areas. Additional rupture offshore is not supported by our analysis. Our results demonstrate how regional array studies can contribute to the characterization of seismic sources in the Caribbean region and elsewhere, particularly in offshore regions where local seismic network or geodetic data coverage are not available, with potential application for rapid earthquake response.

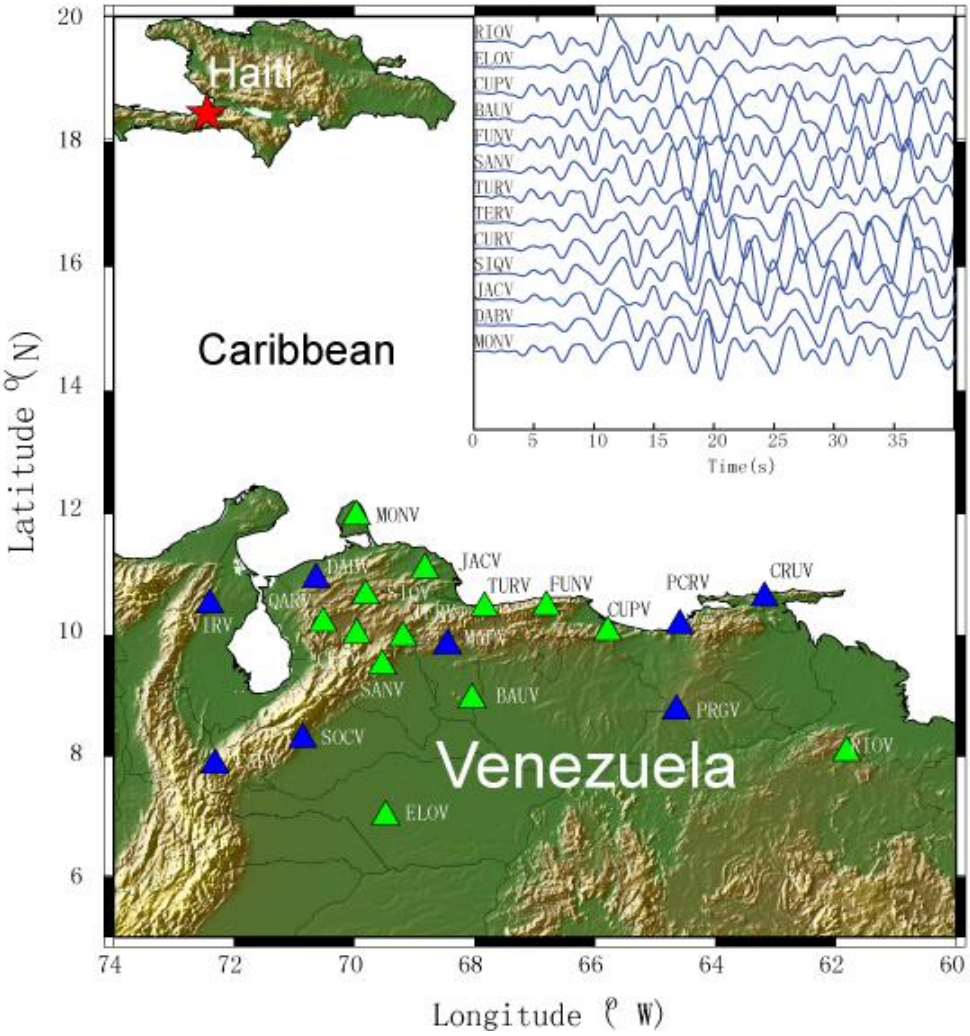

Figure 5.1. Haiti earthquake recorded by the Venezuela National Seismic Network. The triangles denote the 22 broadband stations of the VNSN that recorded the 2010 Haiti earthquake. The 13 stations shown in green were selected for our analysis based on their mutual coherency and signal to noise ratio. The red star indicates the epicenter (NEIC) of the Haiti event. The inset shows vertical component seismograms filtered from 0.2 to 0.7 Hz, aligned on their first P arrival and normalized by the standard deviation of their first 10 seconds.

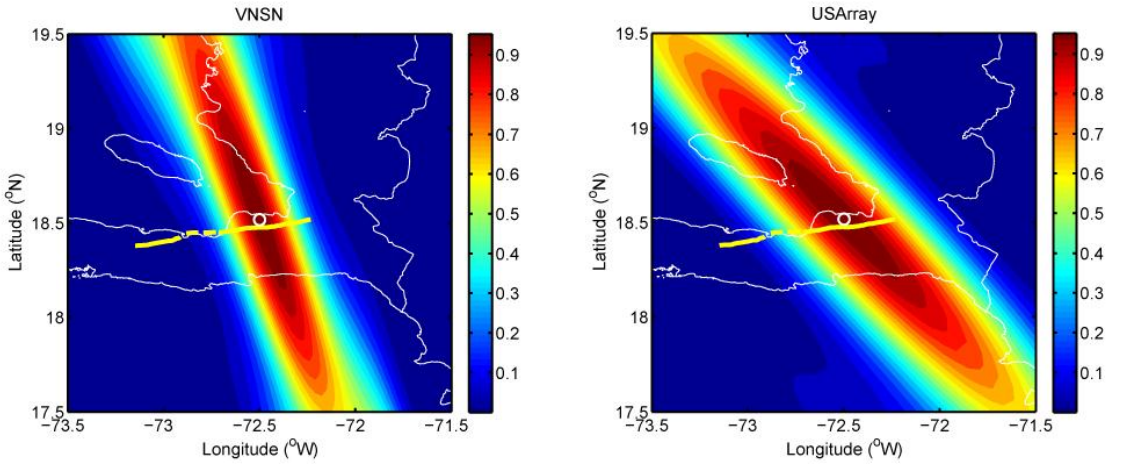

Figure 5.2. Array response patterns, of the VNSN (left) and USArray (right) back-projected into the Haiti source region plotted in map view. The color scale indicates the power of the array response, normalized by its peak value. This normalized color scale is used in all back projection images throughout the paper. The yellow line denotes the trace of the EPGF [*Calais et al.* 2010]. The white circle is the location of the NEIC epicenter.

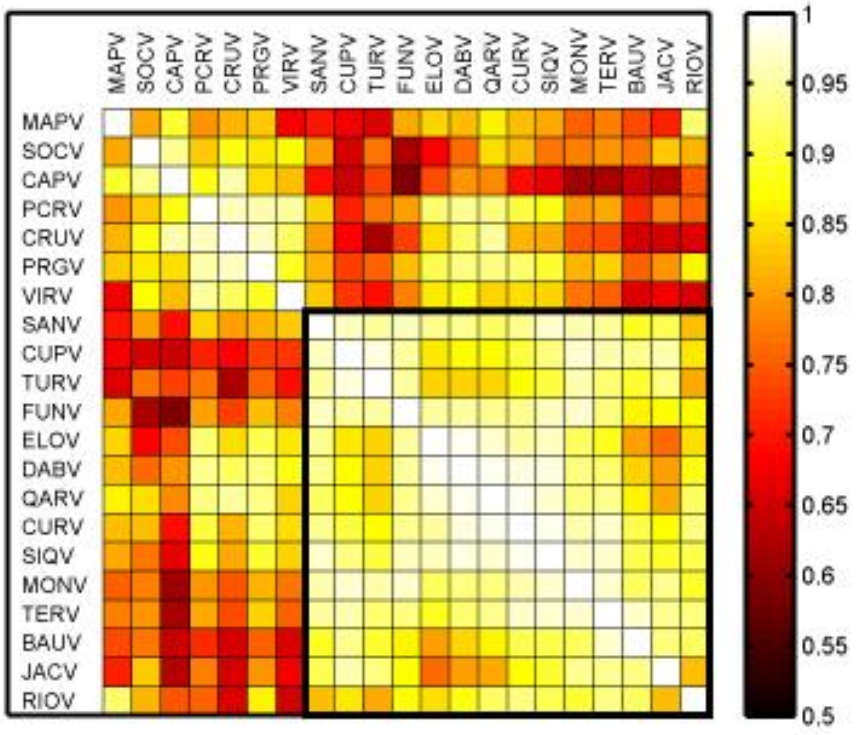

Figure 5.3. Station selection based on array data correlation matrix made of the correlation coefficients between all pairs of stations (indicated by the color scale). The stations are reordered by a clustering algorithm. The black box encompasses the most mutually coherent subset of stations, which is used in our array analysis.

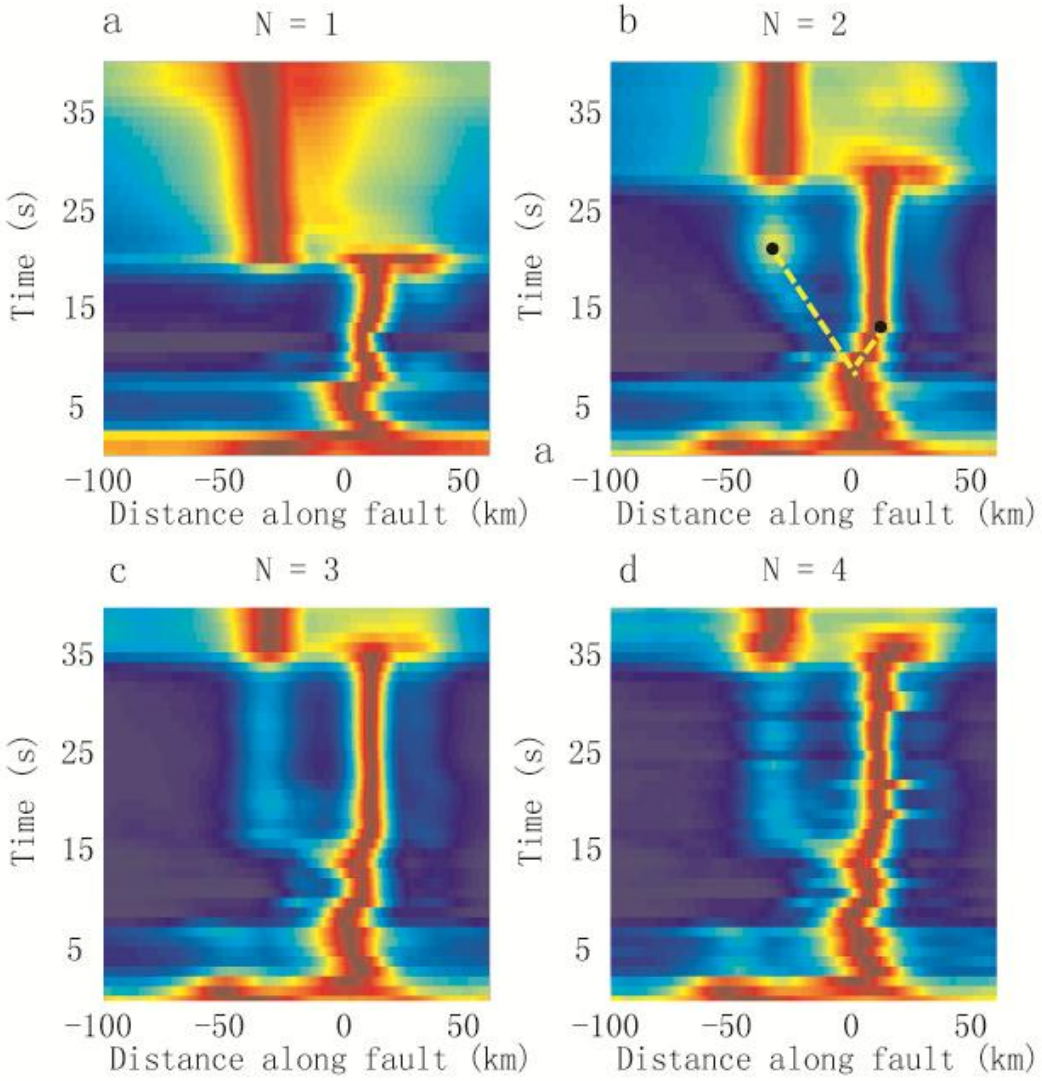

Figure 5.4. Dependence of MUSIC results on the assumed size N of the signal subspace, at 0.4 Hz with N=1 to 4 (a to d, respectively). The MUSIC pseudo-spectrum as a function of along strike position with respect to the hypocenter is shown in color and normalized by its maximum in each time window (color scale indicated in figure 5.2). The time axis is defined as the final time of the sliding windows of 30 s long sliding windows. The horizontal axis is the distance along the fault with respect to the epicenter. The yellow dashed lines and the black dots in figure b (N=2) show the bilateral rupture trend and subevent locations.

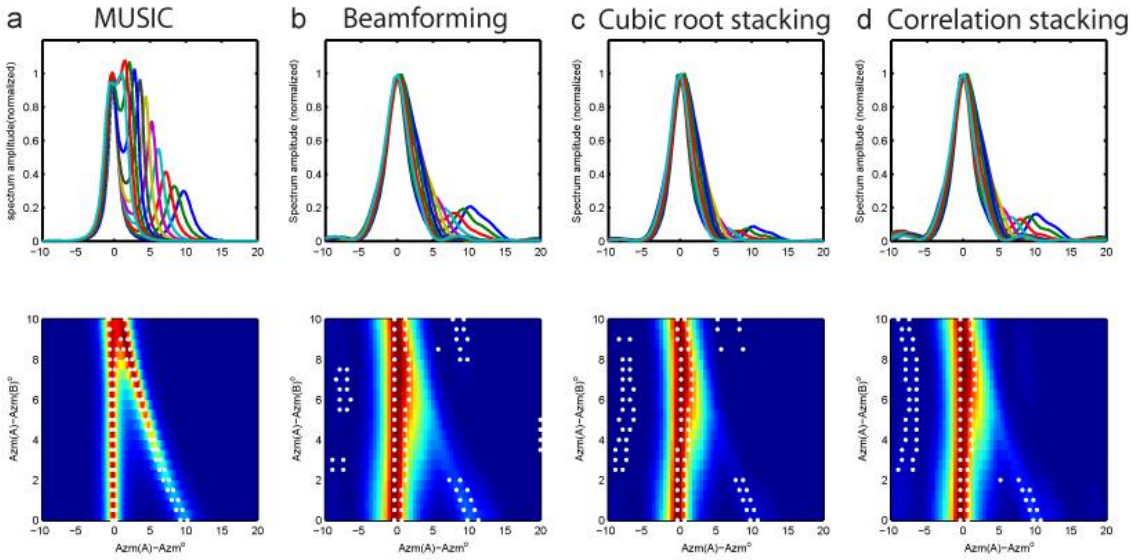

Figure 5.5. Comparison of resolution between array processing techniques. Two plane waves, A and B, impinge on a linear array. The azimuth of A is fixed at 0 degrees while the azimuth of B is varied from -10 to 0 degrees. Four array processing techniques are considered: MUSIC (a), classical beamforming (b), cubic root stacking (c), correlation stacking (d). Each curve in the top plots shows the normalized pseudo-spectra (a) or the stack (b-d) as a function of relative azimuth with respect to A for a given azimuth separation between A and B (value indicated in the legend). The bottom panels show the same quantities in color plots (color scale indicated in figure 5.2). The white dots mark the half-width of the two largest maxima at a given azimuth of B. This comparison shows that MUSIC can resolve waves with azimuth separation as small as 3 degrees, achieving at least twice higher resolution (minimum resolvable azimuthal separation) than the other methods.

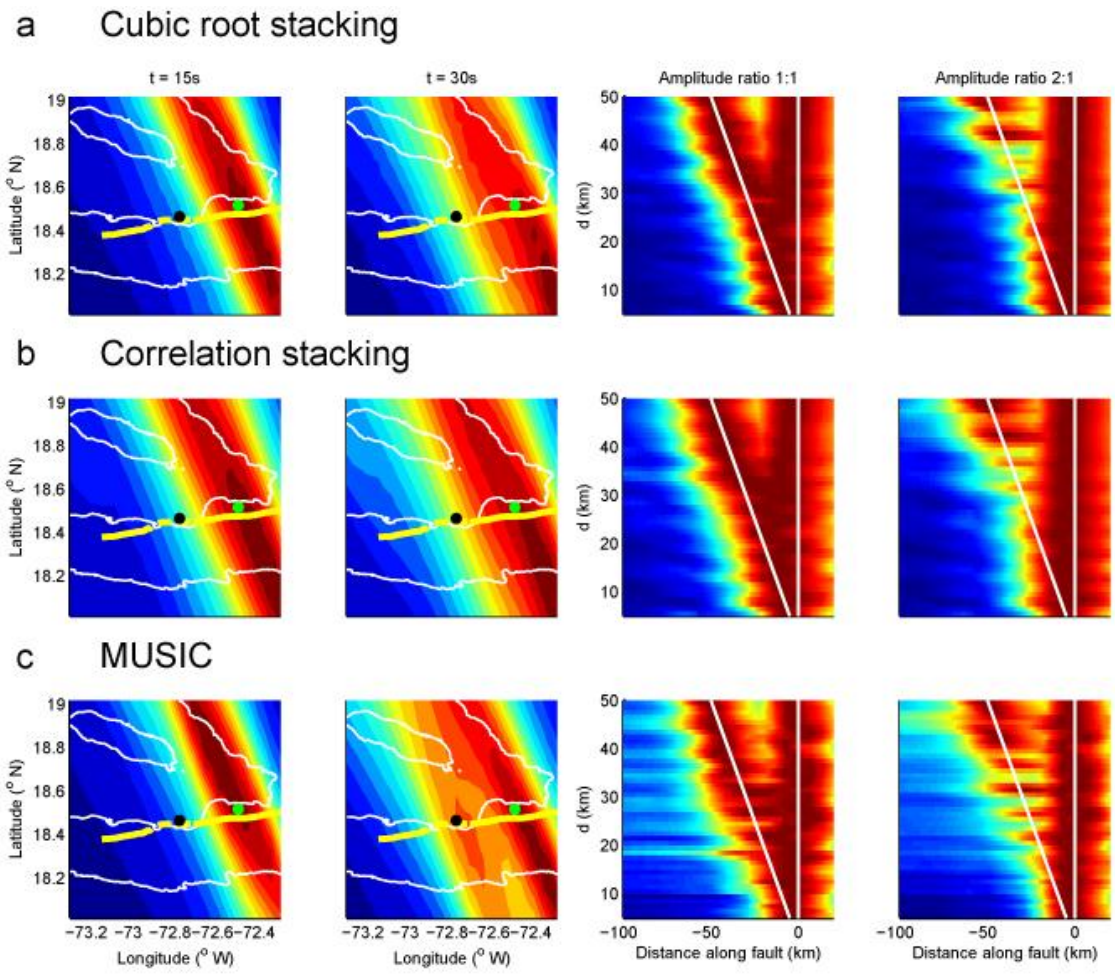

Figure 5.6. Synthetic test of array processing for the Haiti earthquake scenario. The earthquake is modeled by two point sources with 3 s long Brune source time functions. The first source is at the hypocenter (green dot) and the second one is at a distance *d* (black dot) westward along the fault trace. We applied cubic root stacking (a), correlation stacking (b) and MUSIC (c). The left two columns are map view back-projection images for d = 30 km (10s delay), in the time windows (30 s long) that end at the t = 15 s and t = 30 s. (t=0 is arrival time of the first source). The right two columns show the projection of the images along the source-to-array direction onto the fault trace, as a function of the distance *d*. The color scale indicates the pseudospectra (c) or the stack (b-c) normalized by the maximum value at each time (color scale indicated in figure 5.2). The white lines indicate the locations of the two sources. We considered moment ratios between first and second sources of 1:1 and 2:1. In the case of 2:1 source ratio, the cubic root stacking and correlation stack-

ing methods show resolution limit of about 35 km, while the resolution limit of MUSIC is about 25 km and the location error is approximately 5 km for each subevent.

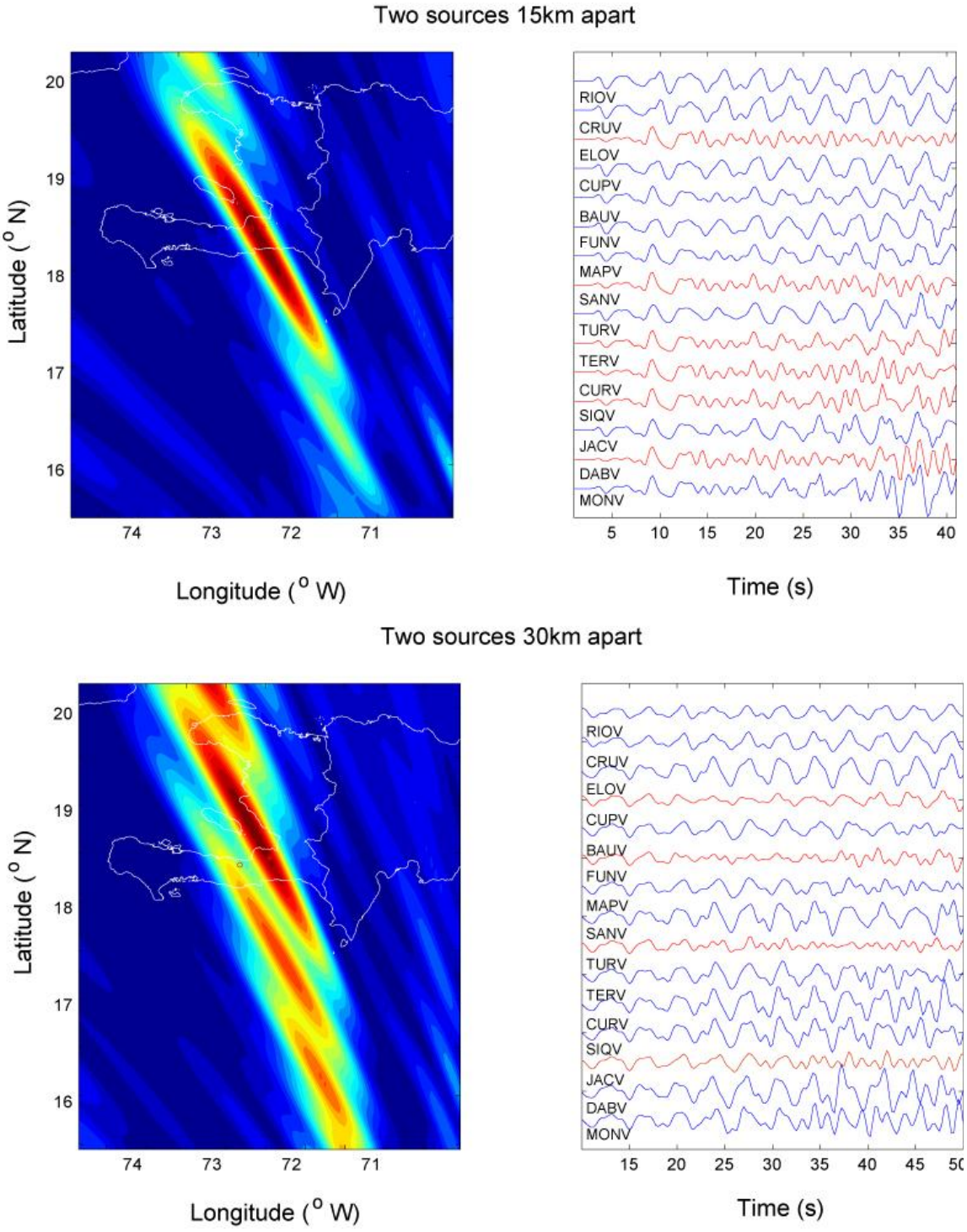

Figure 5.7. Interference issues associated with the beamforming analysis. Results of two synthetic tests with a composite source comprising two subevents 15 km (top) and 30 km (bottom) apart with Green's function computed with the frequency-wavenumber method of Zhu and Rivera (2002). The

30 s long time window ends at 15 s after the arrival of the second source. Left: maps of cubic root beam amplitude back-projected into the source region. Right: synthetic seismograms. The stations deficient in low frequencies, due to interference effects, are colored in red.

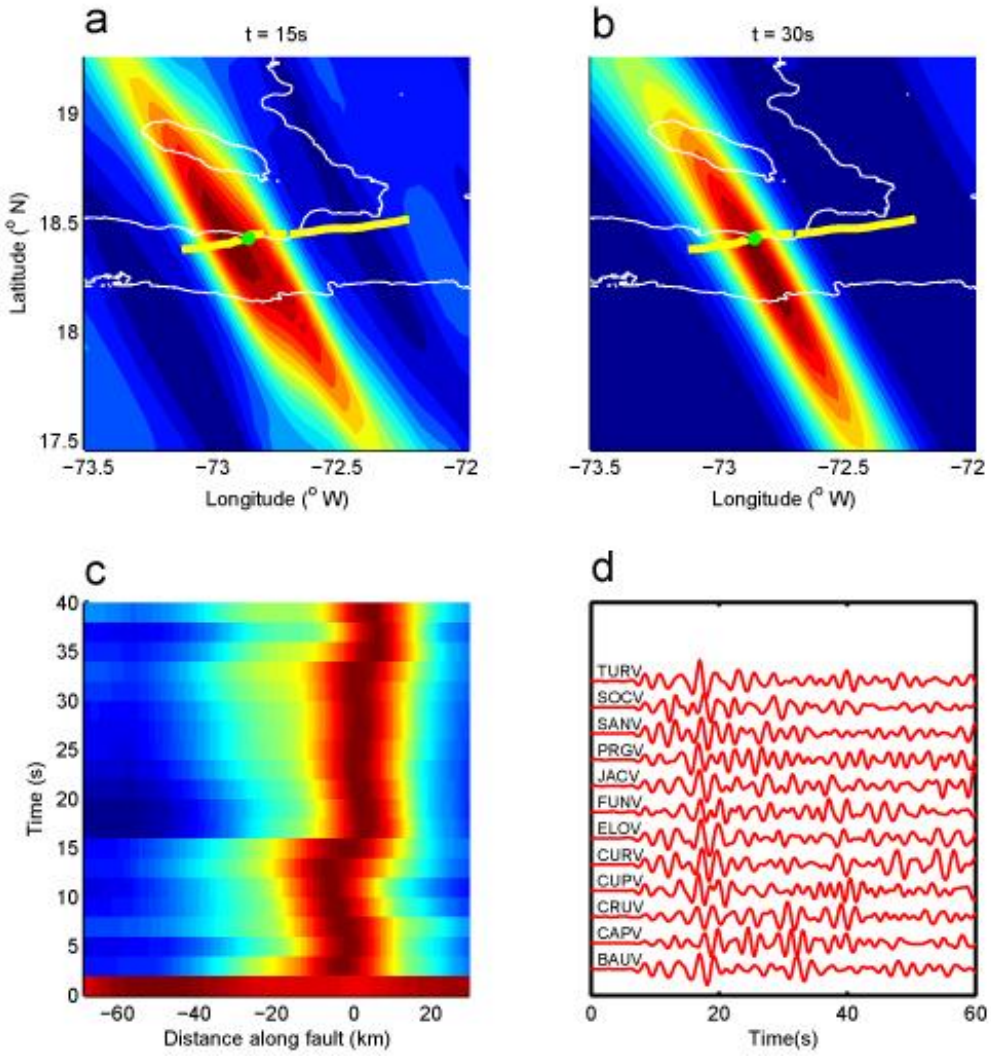

Figure 5.8. The MUSIC analysis of the largest aftershock (M5.9). The top row shows MUSIC images from 30 s long time windows ending at t=15 s and 30 s, respectively (t=0 s is the arrival time). The green dot indicates the location of the epicenter. The yellow curve indicates the trace of the EPGF [*Calais et al.* 2010]. The bottom left plot shows the projection on the fault as a function of final time of the sliding window. The color scale indicates the normalized MUSIC pseudospectra (color scale indicated in figure 5.2). The vertical recordings of the aftershock recorded at the VNSN filtered at 0.2 ~ 0.7 Hz shown in the bottom right panel.

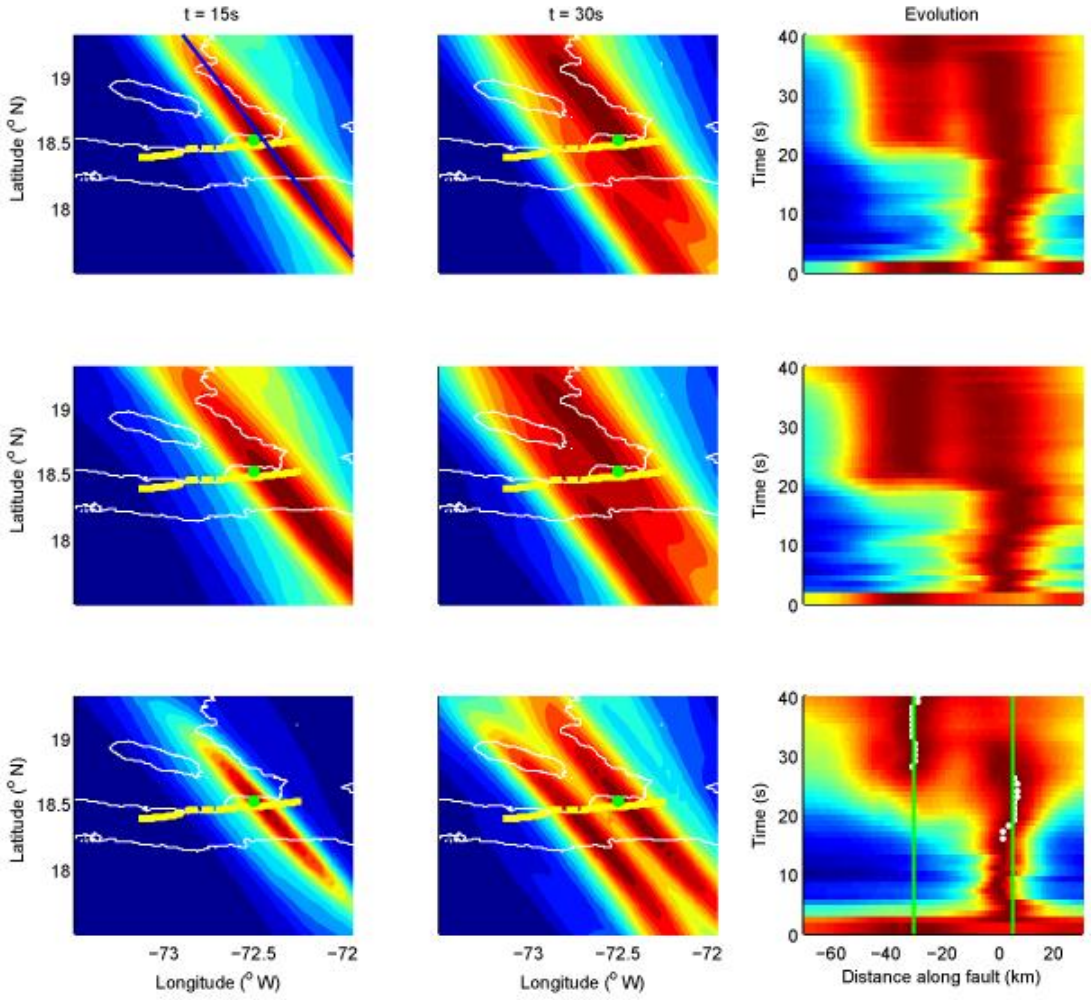

Figure 5.9. Array analysis of the Haiti event. Considering cubic root stacking (a), correlation stacking (b) and MUSIC (c). The left two columns shows back-projection images at t=15 s and 30 s. The MUSIC analysis has higher resolution and can clearly separate two asperities. The blue line in the top-left plot is the major axis of the array response pattern along which we project the array analysis onto the fault. The right column shows the projection on the fault as a function of final time of the sliding window. In the bottom-right plot, the peak locations of the two subevents are marked white dots. For each subevent, the averaged location is denoted by the green line. The color scale and rest of the symbols are used in the same fashion as in Figure 5.8.

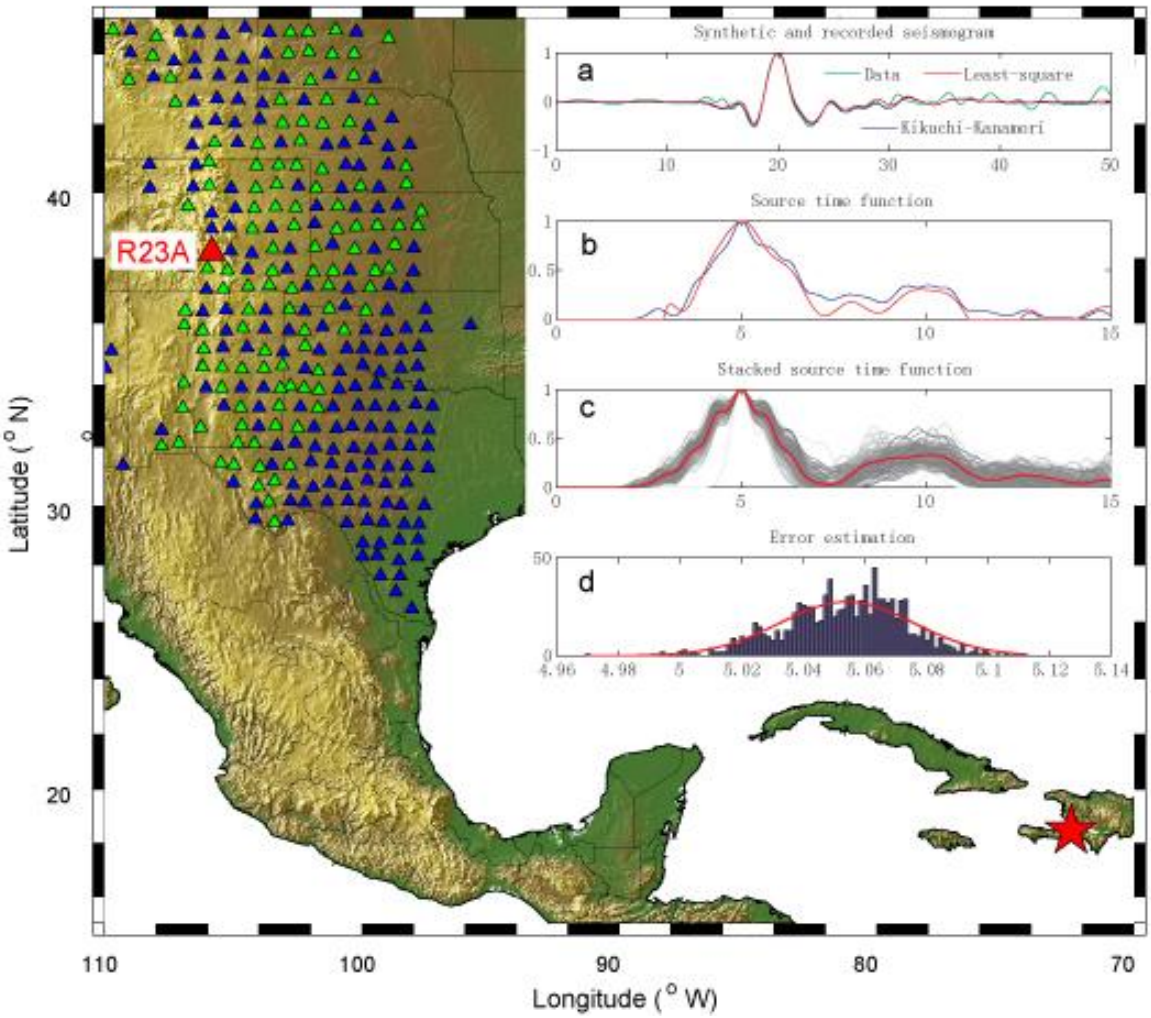

Figure 5.10. Source time function from USArray data. The blue and green triangles in the map show the USArray stations that recorded the Haiti event. The stations in green have epicentral distance greater than 30 degree and good signal to noise ratio, and are selected for deconvolution. The red star is the epicenter of the Haiti earthquake. The red triangle is station R23A. The inset shows (a) the recorded and synthetic seismograms, (b) the source time function retrieved by non-negative least square (red) and Kikuchi-Kanamori deconvolution techniques (blue) at station R23A; and (c) source time functions (grey) from all selected USArray stations and the stacked source time function (red). (d) histogram showing the delay between the two peaks from bootstrapping the stacked source time functions and the best-fit Gaussian distribution (red curve).

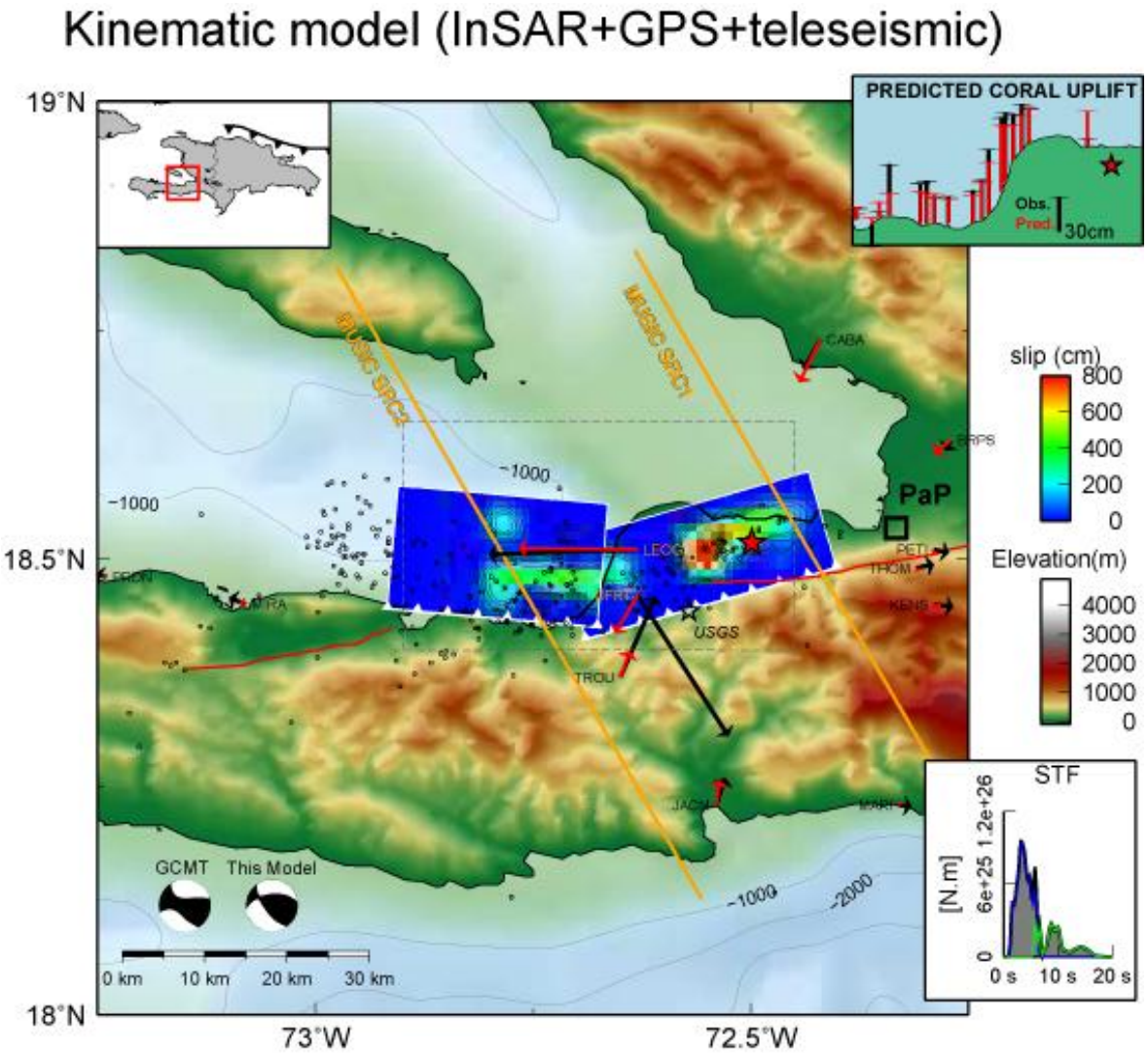

Figure 5.11. Improved joint finite fault inversion of the Haiti event. Surface projection of the slip distribution inferred from the joint inversion of teleseismic, GPS and InSAR data. The black and red arrows represent the recorded and model predicted campaign GPS vectors respectively. The two orange dash lines mark the locations of the subevents identified by MUSIC back-projection assuming our refined mainshock epicenter as reference (red star). The black empty star is the USGS epicenter. The small empty circles are the aftershock epicenters of the Haiti-OBS campaign. The three inset maps show the location of the study area (top left), the measured (black) and predicted (red) coastal uplift based on coral data [*Hayes et al. 2010*] (top right) and the inverted source time function (lower right). The dashed line rectangle on the main map corresponds to spatial extent of the

coastal uplift inset map (top right). On the source time function plot, the blue and green curve show the contribution of the Leogane and offshore fault segments respectively.

C h a p t e r 6

MITIGATING ARTIFACTS IN BACK-PROJECTION SOURCE IMAGING WITH IMPLICATIONS FOR FREQUENCY-DEPENDENT PROPERTIES OF THE TOHOKU-OKI EARTHQUAKE

Originally published in L. Meng, J.-P. Ampuero, Y. Luo, W. Wu and S. Ni (2012), Mitigating artifacts in back-projection source imaging with implications on frequency-dependent properties of the Tohoku-Oki earthquake, *Earth, Planets and Space*, special issue "The 2011 Tohoku-Oki earthquake". Doi:10.5047/eps.2012.05.010.

6.1. Abstract

Comparing teleseismic array back-projection source images of the 2011 Tohoku-Oki earthquake to results from static and kinematic finite source inversions has revealed little overlap between the regions of high and low frequency slip. Motivated by this interesting observation, back-projection studies extended to intermediate frequencies, down to about 0.1 Hz, have proposed that a progressive transition of rupture properties as a function of frequency is observable. Here, by adapting the concept of the array response function to non-stationary signals, we demonstrate that the "swimming artifact," a systematic drift resulting from signal nonstationarity, induces significant bias on beamforming back-projection at low frequencies. We introduce a "reference window strategy" into the multitaper-MUSIC back-projection technique and significantly mitigate the "swimming artifact" in high frequencies (1 s to 4 s). At lower frequencies, this modification yields notable but significantly smaller artifacts than time-domain stacking. We perform extensive synthetic tests that in-

clude a 3D regional velocity model for Japan. We analyze the recordings of the Tohoku-Oki earthquake at the USArray and at the European array at periods from 1 s to 16 s. The migration of the source location as a function of period, regardless of the back-projection methods, has characteristics that are consistent with the expected effect of the "swimming artifact." In particular, the apparent up-dip migration as a function of frequency obtained with the USArray can be explained by the "swimming artifact". This indicates that the most substantial frequency-dependence of the Tohoku-Oki earthquake source occurs at periods longer than 16 s. Thus, low frequency back-projection needs to be further tested and validated in order to contribute to the characterization of frequency-dependent rupture properties.

6.2. Introduction

As one of the most important earthquakes in the history of seismology, the 2011 M9 Tohoku-Oki earthquake enables a broad spectrum of studies of the physics of devastating subduction earthquake giants. One key feature observed in this earthquake is that most of the low frequency (LF) slip is located up-dip from the hypocenter. This is supported by teleseismic and geodetic source inversions [*Koketsu et al.* 2011; *Lee et al.* 2011; *Shao et al.* 2011; *Simons et al.* 2011; *Yue and Lay* 2011], sea-floor displacement measurement [*Sato et al.* 2011] and Rayleigh wave back-projection [*Roten et al.* 2011], In contrast, the high frequency (HF) slip is distributed at the bottom of the seismogenic zone. This is inferred from teleseismic back projection [*Ishii* 2011; *Koper, Hutko, Lay, Ammon et al.* 2011; *Meng et al.* 2011; *Wang and Mori* 2011; *Yao et al.* 2011] and local strong motion studies [*Asano and Iwata* 2011; *Meng et al.* 2011; *Miyake et al.* 2011]. This frequency-dependent rupture behavior is reported by Nakahara et al. (2008) for a number of earthquakes and has also been proposed for the 2004 Sumatra and 2010 Maule earthquakes [*Lay et al.* 2012]. This spatial complementarity between low and high frequency slip provides interesting constraints for physical models of

earthquake rupture [*Kato* 2007; *Huang et al.* 2011] and is important for strong motion prediction. Meng et al. (2011) related this observation to rheological heterogeneities in a broad brittle-ductile transition zone.

Motivated by the spatial complementarity between LF slip (< 0.1 Hz) and HF slip (~1 Hz), a number of studies [*Koper, Hutko, Lay* 2011; *Mori* 2011; *Yao et al.* 2011; *Lay et al.* 2012] attempted to probe the transition between these two frequency ranges by performing back-projection at intermediate frequencies. Their results based on the USArray recordings suggest a progressive up-dip migration of the dominant sources as a function of decreasing frequency from 1 to 0.1 Hz. As plausible as this finding is, the back-projection at low frequencies around 0.1 Hz needs to be validated. A potential source of bias addressed here is the so-called "swimming artifact" [*Ishii et al.* 2007; *Walker and Shearer* 2009; *Xu et al.* 2009; *Yao et al.* 2012] which appears as a frequency-dependent migration artifact due to the nonstationarity of seismic signals. This artifact is a well-known problem in the back-projection community. It degrades the quality of the images and makes it difficult to build confidence on the fine details of the source imaging, especially when the features of interest have a similar migration direction as the artifact. A common practice is to smooth the images to suppress the artifact [*Koper, Hutko, Lay* 2011], but this is not fully successful and comes at the expense of resolution.

In this study, by introducing a modified form of the array response function for nonstationary signals and synthetic tests that incorporate regional velocity models for Japan, we show that the "swimming artifact" is prominent in low-frequency beamforming back-projection and can lead to apparent frequency-dependent rupture behavior. On the other hand, by adopting a "reference window strategy" in the frequency-domain MUSIC back-projection [*Meng et al.* 2011], we are able to

compensate the signal nonstationarity and mitigate the swimming artifacts at high frequency (~1 Hz) and significantly reduce them at relative low frequencies (~0.1 Hz). Based on extensive synthetic tests and improved results from the USArray and European array, we find that the frequency-dependent source offset observed for the Tohoku-Oki earthquake is consistent with the expected effect of the artifact regardless of the back-projection methods. We thus conclude with a cautionary note on the inference of frequency dependent source properties from low frequency back-projection studies.

6.3. "Swimming" Effect in Back Projection of Nonstationary Signals

6.3.1. Nonstationary Array Response Function

The basic tool to assess the resolution capability of a seismic array is the array response function (ARF) defined as the linear beamforming amplitude as a function of source location (or direction of arrival theta) offset with respect to the true location of a point source, under the assumption of a stationary signal with perfect coherence across the array (e.g., Rost and Thomas 2002):

$$A(\theta) = \left| \sum_{k} e^{i\omega t_k(\theta)} \right|^2$$

where ω is the angular frequency, and t_k is the the time delay at the *k*th station as a function of relative location θ of the trial source. In principle, the true source location brings in phase the signal at all the stations and yields the maximum array beamforming output. The ARF of 2D arrays typically shows an elliptical main lobe, whose size is proportional to the wavelength to aperture ratio and defines the resolution limit of standard beamforming. In reality, earthquake waveforms are far from being stationary. Their envelope amplitude decays as a function of time due to scattering in the

heterogeneous crust [*Sato and Fehler* 1998; *Zerva and Zervas* 2002]. To account for the nonstationarity of the seismic signal, we propose a modified ARF by introducing an additional time dimension and a decaying weight function *S(t)* that represents the typical decay of the waveform envelopes:

$$A(\theta) = \left| \sum_k S(t_k(\theta)) e^{i\omega t_k(\theta)} \right|^2$$

The function *S(t)* can be rather complicated since it involves both the amplitude and phase perturbation. Furthermore, in general this function differs from station to station due to site effects. To simplify the presentation, we consider that *S(t)* is the same for all the stations in the array and adopt a decaying exponential function. We estimate its characteristic decay time as a function of frequency by fitting a decaying exponential to the envelope of the stacked USArray seismograms of a Mw 7.1 foreshock (on March 9, 2011) in different frequency bands. Introducing this decay function into the ARF represents the beamforming of a signal with an exponentially decaying envelope starting at t = 0 (Fig. 6.1.c).

6.3.2. The Origin of the "Swimming Artifact"

We study the modified ARF in a 2D Earth configuration first. A linear array composed of 16 stations is located at teleseismic distances, from 75 ° to 90 ° away from the hypocenter of a point source. The stations are regularly spaced by 1 °(Fig. 6.1a). We computed the modified ARF in different frequency bands. Figure 6.1b shows that the main lobe of the modified ARF migrates as a function of time toward the direction of the array. This is the hallmark of an artifact that has been referred to in previous back-projection studies as the "swimming artifact" [*Ishii et al.* 2007; *Walker and Shearer* 2009; *Xu et al.* 2009; *Yao et al.* 2012]. Our analysis shows that the artifact is caused by the nonstationarity of the signals.

Although the decay rate of *S(t)* controls the severity of the artifact, the existence of the bias is inevitable as long as the signal power decays as a function of time. In particular its existence does not depend on the detailed shape of the decay function. The origin of the artifact can be understood as follows. We consider the true source location A and a trial location B closer to the array. At t = 0 s, when the signal envelope reaches its maximum, the travel time curve from source A samples the maximum of the signal envelope at all stations and leads to a maximum stack. Thus the peak of the beam gives a correct estimate of the true location. Later on, for instance at t = 10 s, the travel time curve from A still aligns the array signals with uniform, although lower amplitude. However, the travel time curve from source B (dashed line in Figure 6.1a) samples also the earlier, larger amplitude part of the waveform. Although it renders the stations slightly out of phase, it gives a larger stack than a trial source on A at t=10 (solid line in Figure 6.1b). Thus, the modified ARF at B is larger than at A, which creates an apparent shift in the estimated source location. The speed of the drift scales with wavelength, so it is amplified at lower frequency. For a given travel time curve, the phase perturbation is smaller at longer period, resulting in the peak sum appearing even further off the true location. Although our analysis is based on the array response, a concept belonging to standard beamforming, this phenomenon is common to all array processing methods, since they are all based on the signal coherency and amplitude.

The “swimming artifact” in this 2D Earth example leads to the naive interpretation that the bias occurs in the source-array direction, which is in the along-strike direction when imaging the Tohoku-Oki earthquake with the USArray. However, in the 3D Earth case, the direction and strength of the artifact are controlled by both the source-to-array direction and the array configuration. Figure 6.2 shows that the artifact is most prominent along the longer axis of the array response for both the USArray and European array. The configuration of the two arrays can be found in Figure 6.3. The ARF of the USArray extends along the E-W direction due to its dominantly longitudinal station

distribution. Hence the swimming artifact operates along dip (Figure 6.2). This can potentially perturb any attempt to image frequency dependent along-dip location of slip.

6.3.3. Mitigating the Artifact

Based on our developed understanding of the origin of the "swimming artifact," we can now propose a mitigation technique. Since the artifact is due to the fact that the windows corresponding to different trial slownesses sample different amplitudes of the nonstationary signal envelope, we propose a certain choice of windowing to minimize the effect of the signal nonstationarity. We call this technique a "reference window" approach.

The idea is to sample the recordings with the window corresponding to a reference slowness, usually corresponding to the hypocenter. When testing different slownesses (corresponding to different trial source locations) instead of using the actual window defined by the trial differential arrival times, we phase shift the data inside the reference window in the Fourier domain. Because this approach tests different slownesses with the same segment of the waveforms, the result is not affected by the temporal nonstationarity of the signals, and therefore the swimming artifact is significantly reduced. Our reference window approach can be understood in the example in Figure 6.1. At t=10 s, when testing the travel time curve corresponding to location B, instead of using the actual curve (blue dashed line in Figure 6.1a) we test a curve B' (orange dashed line in Figure 6.1a) that has the same slope as B but whose mean is adjusted to that of curve A. This curve B' corresponds to the same location as B but has a delayed absolute source origin time. Curves A and B' sample the same part of the waveform and thus the same amplitude of the signal. Curve B' has a smaller stack than curve A since it is off phase. Therefore the correct location A is recovered and no artifact is introduced.

The reference window strategy is embedded in frequency domain back-projection techniques, such as the frequency-domain beamforming, MUSIC [*Meng et al.* 2011] and compressive sensing [*Yao*

et al. 2011], in which the Fourier coefficients or the covariance matrix are computed based on the signals in the reference window. Because the Fourier shift implies periodic signals, the phase shift should not be too long relative to the window. Hence the method is appropriate provided that the differential arrival times across the array are small compared to the length of the window. This is true when the sizes of the array and source region are small compared to the distance that P waves travel over the window duration. For the Tohoku-Oki earthquake imaged by the European array and USArray at teleseismic distance, if the trial source region is up to 2 ° from the epicenter, the standard deviation of the travel time curve is smaller than 1 s, which is a small fraction of the 10 s long window. Hence the reference window approach is valid in this case.

The reference window approach introduces a time shift, the difference between the mean of B and B', therefore a timing correction is needed [*Yao et al.* 2011]. This correction is readily implemented once the radiator locations have been identified in each back-projection image frame. The timing shown in our summary maps of HF radiation incorporates this correction, in which the true source time (color coded) of each identified radiator equals to the timing of the back-projection image frame minus the mean of the travel time curve corresponding to the location of the radiator. In the next section we conduct a series of synthetic tests to compare the frequency domain MUSIC (reference window) and time domain stacking (absolute window).

6.4. Synthetic Test of Back Projection at Various Frequencies

6.4.1 Point Source Synthetic Test

To demonstrate the artifact at various frequencies and how well it can be mitigated by MUSIC, we test the back-projection on the synthetic USArray and EU array seismograms of a M6.2 aftershock with hypocenter location at 143.4 ° E, 38.32 ° N. The station distributions of the two arrays are

shown in Figure 6.3. The synthetics are computed by a hybrid approach in which the wavefield in the source region (a 1100 km × 1000 km × 70 km box) is computed by the spectral element method (SPECFEM3D, [*Tromp et al.* 2008]) and interfaced with the geometrical ray theory up to the teleseismic receivers [*Helmberger* 1983]. This approach enables incorporating the complexity of regional velocity structures at affordable computational cost and is ideal for testing teleseismic back-projection techniques at relatively high frequencies. In the SPECFEM3D simulation we used a regional tomography model [*Miura et al.* 2005] to account for waveform complexity introduced by 3D structures. The synthetic seismograms are computed with the sampling rate of 5 Hz, but due to the limited computation power accuracy in the SPECFEM simulation is warranted only up to 1 Hz. Future work involves incorporating realistic small scale heterogeneities in the velocity model under the receivers to model waveform incoherence and coda decay.

Figure 6.4 shows the results of MUSIC and time-domain stacking back-projection of the aftershock scenario at various frequency bands. As expected from the modified ARF, the peak of the beam-forming power progressively migrates along the major axis of the array response. Like in our idealized ARF analysis, the peak amplitude decreases as it swims. On the other hand, the spatial bias of the MUSIC analysis at high frequencies (0.25 ~1 Hz) is negligible. At frequencies lower than 0.25 Hz, the location shift is notable but substantially smaller than in time-domain stacking. Hence at low frequency the "swimming" artifact cannot be ignored even with the MUSIC approach.

6.4.2 Kinematic Source Synthetic Test

To further understand the artifact under more complicated and realistic circumstances, we conduct a kinematic rupture scenario involving two branches of simultaneous rupture along a circular rim (Fig. 6.5). The circle is centered at the hypocenter of the M6.2 aftershock with a radius of 100 km. It

is divided into two semicircles by a line trending 210 ° through the center. Two simultaneous north-to-south ruptures develop along each semicircle with rupture speed of 2 km/s. Physically, this scenario is inspired by dynamic simulations in which a rupture front surrounds a circular asperity or low stress region before breaking it [*Dunham et al.* 2003]. The ruptures are composed of moving sources with a spatial interval of 40 km. This spacing is chosen so that the sources are dense enough to represent a continuous rupture, yet the coda wave is still substantial to maintain realistic signal nonstationarity. The Green's functions are the same as for the M6.2 aftershock. This circular rupture model is relatively simple but has enough complexity, including simultaneous sources with temporally varying spacing.

Figure 6.5 shows the results of MUSIC and linear beamforming back-projection of the circular rupture scenario with seismograms computed for both USArray and European array at periods from 2 s to 16 s. In order to compare to results by Yao et al. (2011), we set the time window to be 10 s at the band of 1s - 4 s and 20 s for 4s - 16 s. The locations of the first and second strongest radiators detected by both arrays in each window are plotted and color-coded by time. The size of the radiators is normalized by the maximum of the beamforming power or MUSIC pseudospectrum over the first 150 s of the rupture. In the highest frequency band (0.5-1 Hz), the MUSIC result of the European array almost exactly reproduces the synthetic rupture scenario, recovering radiators on the edge of the circle. The USArray result is noisier and distributed within the circle because its Green's functions have a smaller coherent arrival to coda ratio resulting from the nodal orientation of the array with respect to the focal mechanism. In the period band of 2 s to 4 s, the MUSIC result of both arrays are within the circle. In the low frequency band (8 s -16 s), the uncertainties become large due to limited resolution and the swimming bias starts to be notable.

In comparison, the beamforming is less capable of resolving the simultaneous sources. The recovered radiators are distributed along the expected artifact direction. Here we also applied a common postprocessing technique to weaken the swimming artifact [*Koper, Hutko, Lay* 2011]. The idea is that although the artifact swims, the true location always has the largest beamformed power. Thus plotting the high frequency power against time and picking only the local maximum can, in principle, discriminate the true source location from the spurious sources. The processing is useful when the source process is simple, for instance for a fixed point source or a unilateral rupture, but less effective in complicated rupture scenarios involving multiple simultaneous sources. In the case of the circular rupture scenario, at relatively short periods (1 s~4 s) the identified radiators are located in between the true locations. At longer periods (4 s~16 s) they show considerable bias "downstream" of the true locations along the artifact direction, creating an apparently frequency-dependent rupture pattern.

6.5. Low Frequency Back Projection of the Tohoku-Oki Earthquake

The along-dip frequency dependent slip migration observed in previous back projection studies is based on the USArray data [*Koper, Hutko, Lay, Ammon et al.* 2011; *Mori* 2011; *Yao et al.* 2011]. The other large regional array, the European array, has been processed at high frequency around 1 Hz [*Koper, Hutko, Lay* 2011; *Meng et al.* 2011]. Analysis of the European array data at longer periods has not been reported before. Here we back-project the Tohoku-Oki earthquake data recorded by the European array and USArray at periods from 2 s to 16 s with both the MUSIC and linear beamforming methods (Fig. 6.6). In order to be comparable to Yao et al. (2011), we set the beamforming time window to be 10 s at the band of 1 s - 4 s and 20 s for 4 - 16 s. The locations of the radiators detected by both arrays in each frequency band are shown at Figure 6.6. The size of the radiators is normalized by the maximum of the beamforming power or MUSIC pseudospectrum

over the first 150 s of the rupture. For time-domain stacking, similar to the point source synthetic test, we observe strong swimming effect at periods longer than 2 s. In the highest frequency band (0.5-1 Hz), the artifact is smaller and the beamforming images are roughly consistent with the MUSIC estimates, which explain the overall agreement of high frequency back-projection studies.

At lower frequencies, the peak beamforming power migrates along the elongated ARF and is clearly dominated by the swimming effect. In contrast, in the MUSIC back-projection results, the dominant distribution of the seismic radiation in the down-dip region is clear in all frequency bands at both arrays, except in the 8~16 s band which shows linear patterns corresponding to the artifact. We therefore restrict analysis of frequency-dependent source behavior based on MUSIC results to the band of 1~8 s. As shown by the synthetic tests, even with the reference window strategy and the MUSIC method, the artifact at lower frequency is significant. For a given period, the radiators imaged by MUSIC with the European array are always to the west of those imaged with the USArray. At USArray an eastward migration of about 70 km is seen between 1 and 8 s. This is consistent with the most clearly reported frequency dependent shifts by compressive sensing [*Yao et al.* 2011]. However, this trend is absent in the European array results, which do not show notable frequency-dependent variation. This difference is consistent with the stronger artifact in USArray, as shown in Figure 6.5, due to the smaller signal to coda ratio resulting from its nodal orientation. Therefore, a frequency-dependent source location is not needed to explain the observations within the 1~8 s band. This indicates that any true frequency dependent source migration is minor compared to the 70 km shift apparent in the USArray back-projection

6.6. Summary and Discussion

In this study we explained the origin of the “swimming” artifact in array back-projection through the modified array response function and synthetic tests. We find that this effect is significant for

time-domain stacking but can be efficiently mitigated by MUSIC array processing with a reference window strategy. MUSIC back-projection of the Tohoku-Oki earthquake recordings at the USArray and European array show no significant tendency for the source to migrate towards the trench at increasing periods within the period band of 1s - 8 s. An alternative interpretation is that the most substantial transition from deep to shallow slip occurs at periods longer than 16 s, which implies even longer rise time in the shallow portion of the megathrust. Furthermore, given that the swimming artifact is substantial in the time-domain stacking back projections especially at long periods, and that this bias at USArray behaves similarly to the potential frequency-dependent along-dip migration of slip, we consider further tests and validations need to be performed before one can conclude that the along-dip slip migration can be observed by the low-frequency back projection.

Our study also poses an interesting question: over which frequency band can we reliably image earthquake rupture processes by teleseismic back-projection? To image the 2011 Tohoku-Oki earthquake by the time-domain stacking technique with the USArray and European array we determined that the frequency should be above 0.25 Hz to avoid substantial artifacts. As for the MUSIC technique, which suffers less severely from the swimming artifact, we suggest that the low frequency results around 0.1 Hz can indicate first order spatial patterns, but the finer details of the images are not reliable due to the limited resolution.

The reference window strategy needs to be compared with other efforts to mitigate the “swimming” effect. For instance, Koper, Hutko, Lay 2011 proposed reducing the strength of the artifact by selecting the temporal maxima among all the identified radiators. However, as we show in the synthetic circular rupture test, this approach cannot fully eliminate the frequency-dependent artifact when dealing with realistic rupture complexity involving for instance multiple simultaneous sources.

One mystery that remains to be solved is the discrepancy between the MUSIC and compressive sensing result [*Yao et al.* 2011]. In principle, they are both performed in frequency domain and share the reference window strategy, therefore should both suffer less from the swimming artifact. Yet, compressive sensing provide large trenchward shift at 10 s ~ 20 s, which is absent in the 8 s ~ 16 s band result with MUSIC. Efforts could be devoted to understand the other potential bias and artifact of various back-projection techniques. This concern also demonstrates the need to perform more rigorous synthetic tests involving more realistic rupture scenarios and crustal velocity models, which we will address in future work.

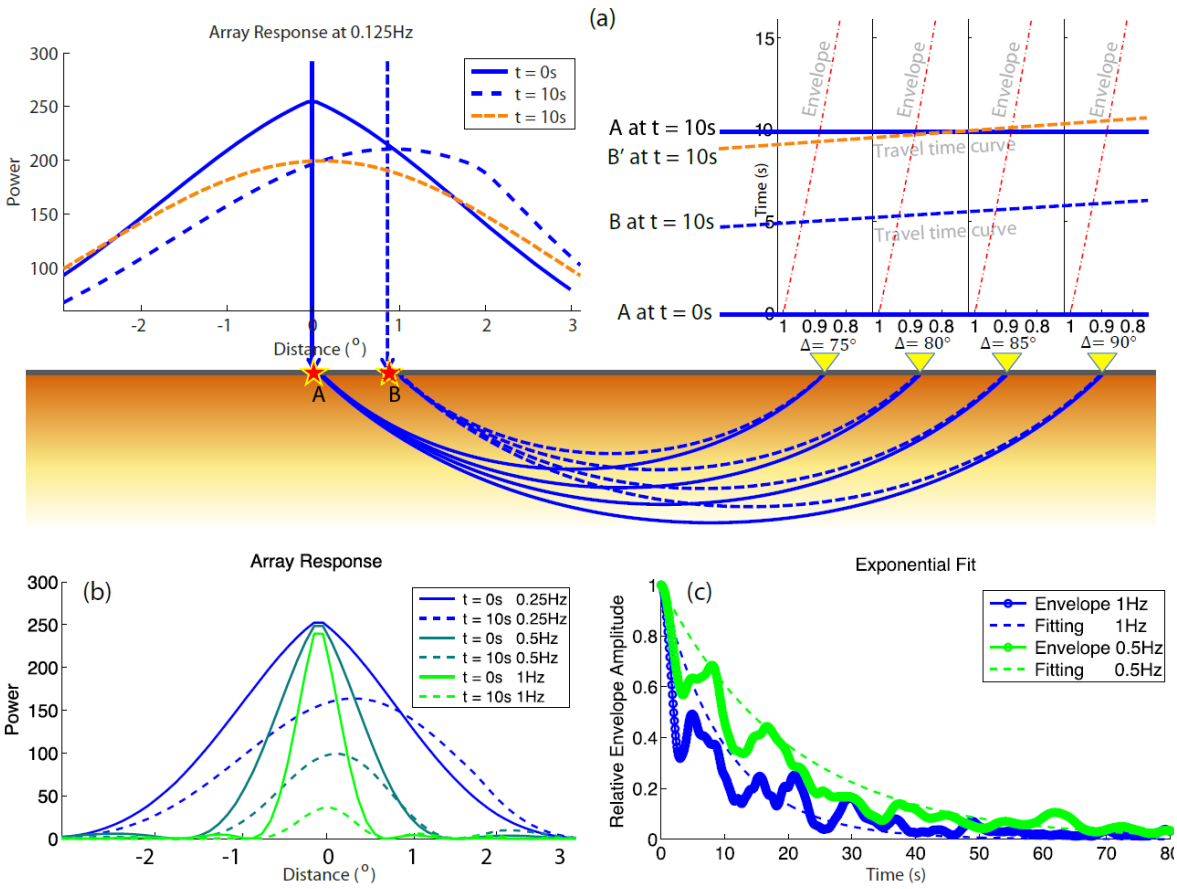

Figure 6.1. The "swimming" artifact of a 1D array in a 2D Earth.

(a) "Swimming" effect at lower frequency (0.125 Hz) with respect to a teleseismic (75 °-90 °) linear array of 16 stations (1 °spacing).

Upper left figure shows the artifact: at t = 10 s, maximum array response drifted from true location A (0 °, as solid-edged star) to apparent location B (0.9 °, dash-edged star), a difference of about 100 km.

Upper right figure shows the traveling time curve sampling envelopes of station 1, 6, 11 and 16 (distance 75 °, 80 °, 85 °, 90 °, respectively, plotted as yellow triangles). The solid and dashed abscissas denote the travel time curve of a hypothetical source occurring at certain location and origin time. At t = 10 s, Blue dashed line is the traveling time curve that yields the overall maximum of the array response taking into account the signal decay. Instead of the true source location A, it introduces an apparent location B closer to the array. The array response of the travel of B' (reference window strategy) is smaller than that of A, therefore no swimming artifact is created.

(b) “Swimming” effect in different frequency bands, with solid curves showing t = 0s, and dashed curves showing t = 10 s, respectively. Note that at all the frequencies the maximum of array response shifts towards the array direction, this effect is reduced at higher frequency. (c) Exponential-fitting estimation of the frequency dependent time decay function. Envelopes of the stacked signals are smoothed with a time window 2.5 times the upper period bound of the band-pass filter. Each envelope is aligned to t = 0 and normalized with respect to its maximum. Due to the contamination of the signals by microseisms, only signals higher than 0.25 Hz are analyzed. An attenuation decay function $e^{-0.1ft}$ is estimated and used for all frequencies in this chapter.

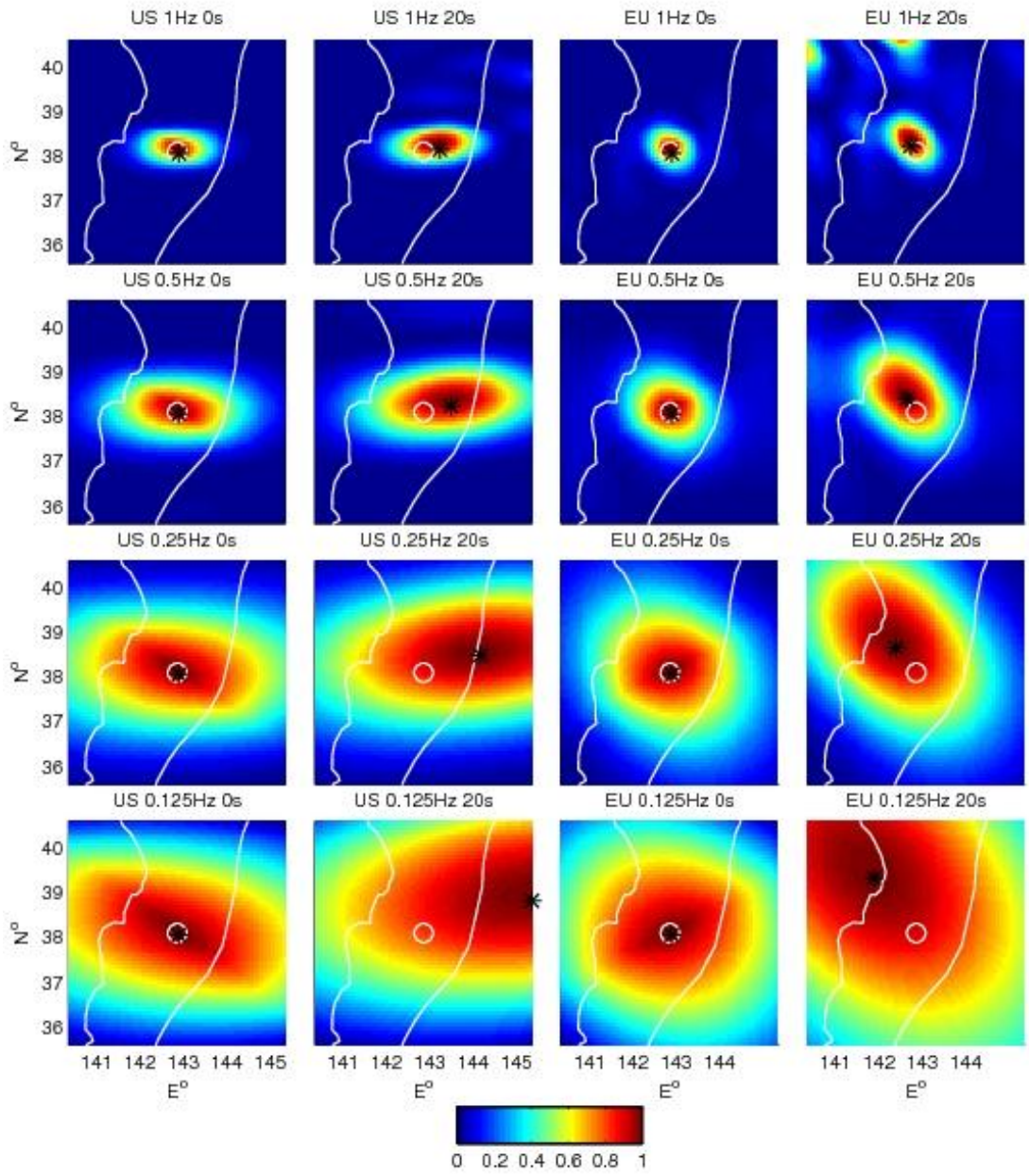
US 1Hz 0s
US 1Hz 20s
EU 1Hz 0s
EU 1Hz 20s
US 0.5Hz 0s
US 0.5Hz 20s
EU 0.5Hz 0s
EU 0.5Hz 20s
US 0.25Hz 0s
US 0.25Hz 20s
EU 0.25Hz 0s
EU 0.25Hz 20s
US 0.125Hz 0s
US 0.125Hz 20s
EU 0.125Hz 0s
EU 0.125Hz 20s
N°
40
39
38
37
36
141 142 143 144 145
141 142 143 144 145
141 142 143 144
141 142 143 144
E°
E°
E°
E°
0 0.2 0.4 0.6 0.8 1

Figure 6.2. Swimming effect in the 2D array response of the USArray (left two columns) and European array (right two columns) at frequency of 1, 0.5, 0.25 and 0.125 Hz, with color coded array response normalized by its maximum, white circle indicates the epicenter and black star indicates the location of maximum array response. Note that the swimming effect intensifies as frequency decreases like in the 1D case, but the maximum swims in a direction that combines the longer axis of the array response and the source-to-array direction.

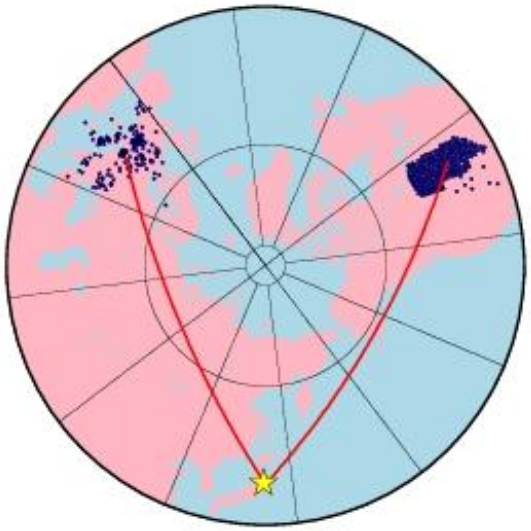

Figure 6.3. Selected stations of the USArray and European array are denoted as the blue dots. The JMA hypocenter of the Tohoku-Oki is the yellow star. The red lines are the great circle parth from the centroid of each array to the hypocenter. The two arrays are both 75 ~90 °away from the hypocenter.

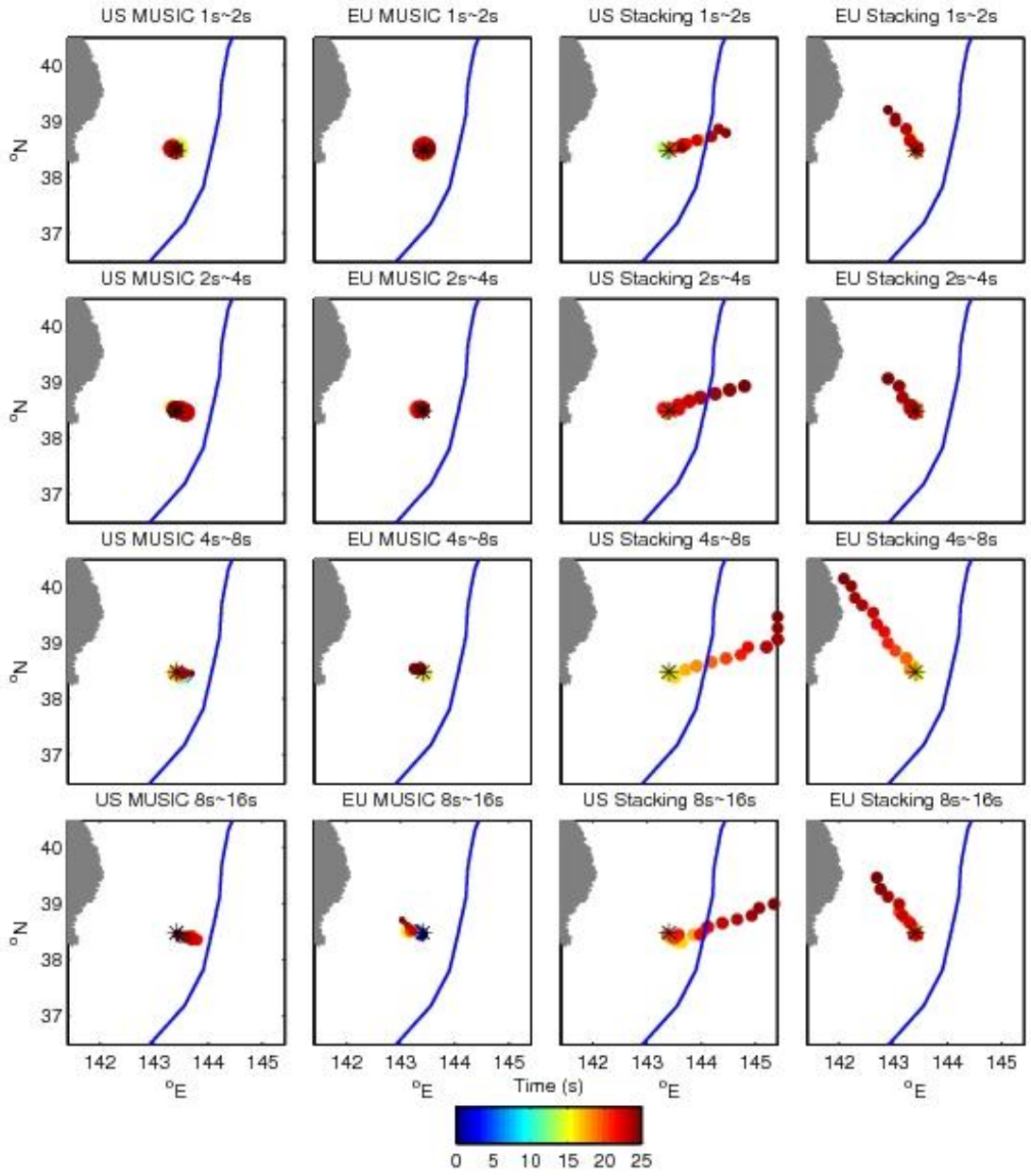

Figure 6.4. Back-projection of aftershock synthetics. The synthetic aftershock seismograms at USArray (left two columns) and European array (right two columns) are processed by the MUSIC and linear stacking techniques separately at periods of 1~2 s, 2~4 s, 4~8 s and 8~16 s. The location of the aftershock is denoted by the asterisk. The solid circles are the peak of the back projection images color coded by time and sized by their relative amplitude with respect to the global maximum. The beamforming results show a "swimming" artifact at all frequencies. The MUSIC estimates are

reliable at periods shorter than 4 s. In lower frequencies, the spatial bias is notable but less severe than that of beamforming.

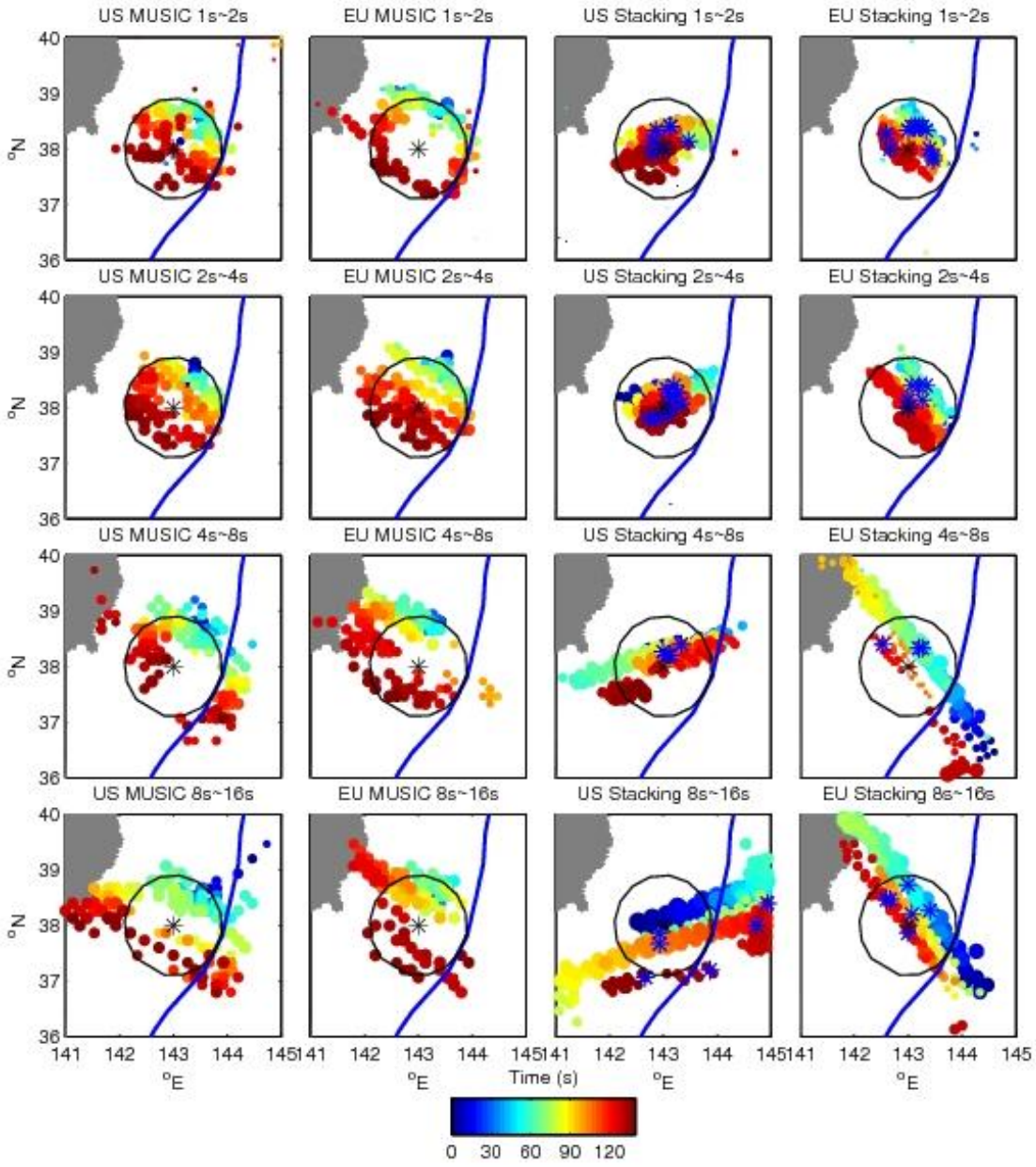

Figure 6.5. Back-projection of circular rupture synthetics. The synthetic seismograms of a circular rupture scenario recorded at USArray (left two columns) and European array (right two columns) are processed by the MUSIC and linear stacking techniques separately at periods of 1~2 s, 2~4 s, 4~8 s and 8~16 s. The location of the aftershock is denoted by the black asterisk. The black circle is the hypothetical circular path of the rupture scenario. The solid circles are the peak of the back pro-

jection images color coded by time and sized by their relative amplitude with respect to the global maximum. The blue asterisks are the “temporal local maxima” of the stacking result. The MUSIC recovers the rupture reasonably well at high frequency but loses the resolution beyond 4 s. The time-domain stacking method shows bias resulting from the swimming artifact.

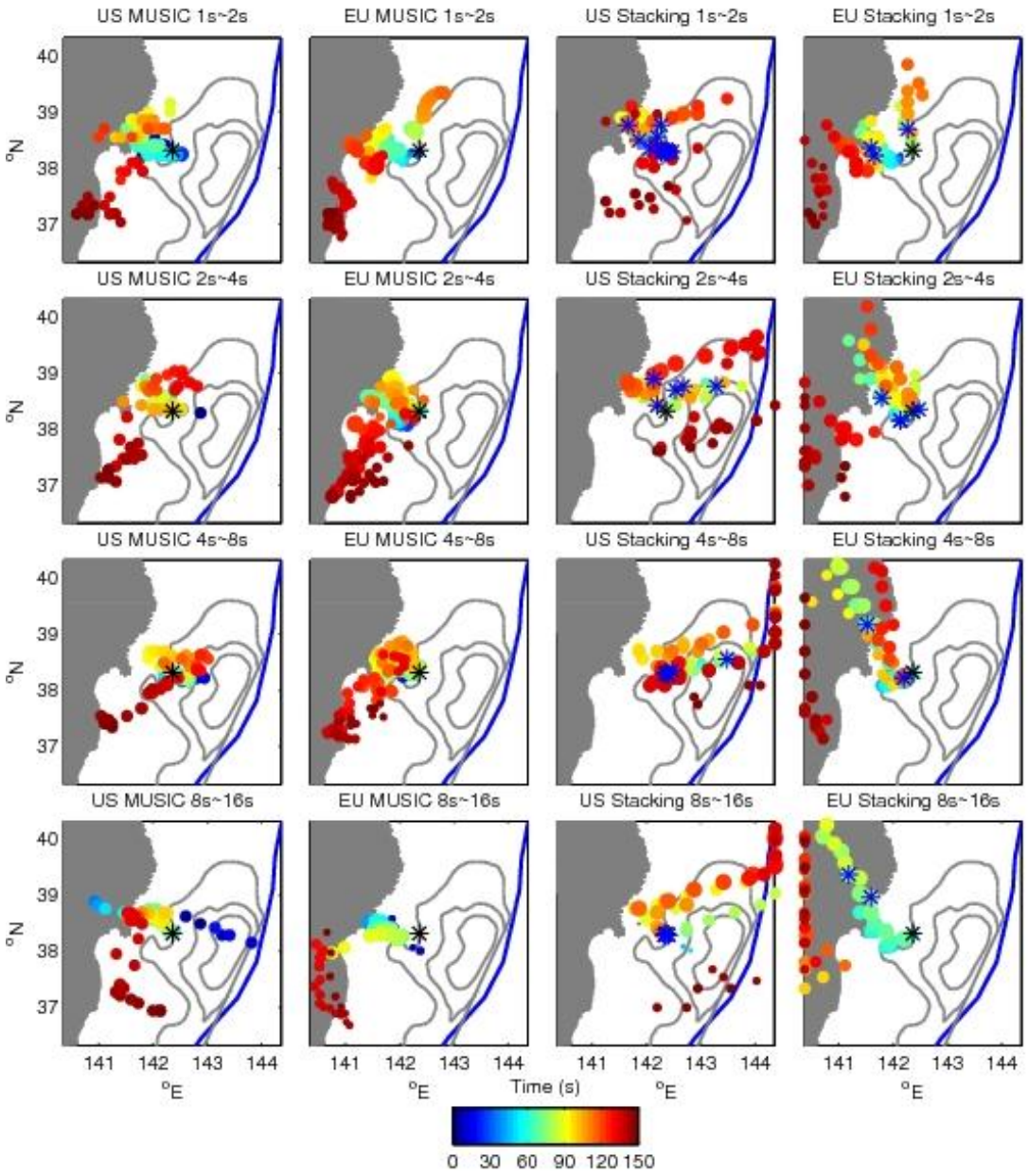

Figure 6.6. Back projection of the Tohoku-Oki earthquake at various periods (1s ~ 16s) of USArray and European array data with the linear stacking and MUSIC approaches. The hypocenter is denoted by the black asterisk. The location of the radiators are colored by time and sized by the amplitude with respect to the maximum. The blue asterisks are the "temporal local maxima" of the stacking result. The background grey lines are 12, 14 and 36 m slip contours of a geodetic and seismic joint inversion model [*Wei et al.* 2012]. The beamforming results are dominated by the artifact at periods longer than 4 s. The MUSIC results are consistent over all frequency bands. Minor up-dip migration

shows up in the period of 1 s ~ 8 s at the USArray, but it is within the range expected from the "swimming" artifact and it is absent in the European network.

A p p e n d i x A

SUPPLEMENTARY MATERIAL OF CHAPTER 2

A.1. Movies of back-projection results

The attached files, jp_movie_EU_music.gif and jp_movie_US_music.gif, are movies showing results of our MUSIC back-projection source imaging in the 0.5-1 Hz band. The quantities plotted and conventions are similar to those in figure 2.3 of the main text.

A.2. Theory and parameter selection of MUSIC back-projection

Theory

We applied a high resolution array processing technique called Multiple SIgnal Classification (MUSIC) [*Goldstein and Archuleta* 1991; *Schmidt* 1986], which estimates the direction of arrival (DOA) of multiple waves propagating through an array by a subspace projection method. We first estimate the covariance matrix of the array data for each sliding time window and each frequency using a multitaper technique [*Thomson* 1982]. The eigenvectors corresponding to its largest eigen-values span the signal subspace. Its complement defines the noise subspace. For a given DOA, a steering vector a collects the Fourier-domain phase shift terms for each station resulting from the differential travel times relative to the hypocentral travel times. The MUSIC pseudo-spectrum, as a function of DOA, is defined as the inverse of the projection of the steering vector onto the noise subspace (through a projection matrix U_n):

$$Pm = \frac{a^H a}{a^H U_n U_n^H a} \tag{A.1}$$

where the superscript H denotes the complex conjugate transpose. Ideally, the steering vector of a

signal is orthogonal to the noise subspace. In practice, the DOAs of the multiple sources are identified by the largest peaks of the MUSIC pseudospectrum. We improve the estimate robustness by averaging over a frequency band the pseudo-spectra normalized by their respective maximum at each frequency. The absolute amplitude of the MUSIC pseudospectrum is not directly related to the strength of the source. Once the DOA of the sources are determined, we estimate their power by the projection of the principal eigenvalues (diagonal matrix Λ_s) onto the signal subspace (projection matrix U_s) excluding the noise power (square of the averaged noise eigenvalues σ) [*Mestre et al.* 2007]

$$Pw = \frac{a^H a}{a^H U_s (\Lambda_s - \sigma^2 I)^{-1} U_s^H a} \tag{A.2}$$

Data Preprocessing and Selection

We band-pass filtered the vertical component of the waveforms between 0.5 and 1 Hz. We then selected the stations with signal to noise ratio greater than 3. We aligned these on the first 8 seconds of P arrival by multichannel cross-correlation [*Vandecar and Crosson* 1990]. The seismograms are then normalized by the standard deviation of the first 200 s of P wave recordings.

Length of Sliding Windows

To achieve a balance between temporal resolution and imaging stability we fixed the length of the analysis windows to 5 times the longest period at which the data is analysed. For our primary frequency band (0.5-1 Hz) we slide a 10 seconds long analysis window by steps of 1 second.

Number of Principal Eigenvalues in MUSIC

In theory the number (M) of eigenvalues of the covariance matrix contained in the signal subspace is equal to the number of signal sources. In practice the signal is not perfectly coherent and its power is partially diverted into the subspace of smaller eigenvalues. We set M equal to the number of eigenvalues greater than the number of stations times the floating point precision scaled by the largest eigenvalue.

Number of Tapers in Cross-Spectrum Estimation

MUSIC achieves better resolution than beamforming in direction of arrival estimation problems with sufficiently long and stationary signals [*Krim and Viberg* 1996]. However, seismic signals are highly transient. This hampers the robust estimation of the data covariance matrix. To circumvent this issue, we estimate the array covariance with the multitaper cross-spectrum estimator [*Thomson* 1982], which averages the Fourier estimates tapered by a sequence of functions with optimal spectral concentration. The Slepian tapers maximize the ratio of energy within and outside a frequency band W for a window of duration T. We require the frequency smearing bandwidth to be at most 20% of the highest frequency (1 Hz), that is, $W = 0.2$ Hz. Following standard practice, we use the first $2TW - 1$ tapers. Hence, for the frequency band 0.5-1 Hz and $T = 10$ s we use 3 tapers.

A.3. Foreshocks and Aftershocks

The M7.2 March 9, foreshock and the March 11, M7.1 aftershock have adequate signal to noise ratio to be aligned and back projected by the USarray (Fig. A.3). The two events appear to radiate coherent energies no longer than 30s with rupture length around 30km. The two events also have different rupture directions, indicating no systematic bias due to the array orientation. The deviation

of the back-projection locations of the initial phases with respect to their epicenter is due to imperfect alignment of the waveforms. We use the M7.1 aftershock as the empirical Green's function for the synthetic scenario tests in the next section.

A.4. Synthetic Tests of Back Projection Source Imaging

To understand the performance and potential bias of the back-projection we conduct tests over a series of hypothetical earthquake scenarios. To include key characteristics of the real wave field, such as the decay of the waveform coherence as a function of time, we employ empirical Green's functions (eGf). Synthetics based on theoretical Green's functions computed by ray theory and spherically symmetric Earth models tend to over emphasize the effect of interference between multiple sources. We chose the March 11, M7.1 aftershock as eGf event. The initial location error due to the waveforms misalignment is corrected by shifting the initial HF radiator to the event epicenter. We first test a scenario of unilateral rupture to the South. We consider 10 uniform subsources located every 15 km along the strike direction (Fig. A.4). Their rupture time corresponds to an assumed rupture speed of 1.5 km/s. The MUSIC back-projection recovers the location and timing of the scenario sources very well. The apparent secondary rupture to the west is an artifact due to the rupture pattern of the eGf event itself.

We also tested more complicated scenarios inspired by our final results of the back-projection of the Tohoku earthquake. Our second scenario is composed of five different phases with various rupture speeds and directions (Fig. A.5). The source process is well recovered, although perturbed by modulation by the rupture pattern of the eGf event. To minimize that effect, in our third scenario the inter-subevent spacing is exaggerated (Fig. A.6). Overall, the back projection results image our synthetic scenarios adequately. In particular, the stages of different rupture speed are reproduced. One

of potential bias of the back projection imaging is that when rupture temporally ceases, the coda of previous rupture would create apparent secondary sources (Fig. A.7). However, these sources show substantially smaller power than the previously sources, which is unlikely to be the case of this earthquake, since we observed sources of almost uniform power during the rupture.

A.5. Rupture Time Versus along Strike and Dip Distance

An alternative way of demonstrating the spatiotemporal rupture evolution is to plot the rupture time versus the along strike and dip distance (Fig.A.8), assuming the strike is 210 °(following the trench trace). The along dip plots indicate very clear down-dip distribution of the HF hotspots. In the along strike plots, both arrays shows very little along strike propagation in the first 100s and progressive southern rupture thereafter, with the exception of supershear rupture at about 80 to 90s clearly imaged by the European array.

A.6. Array Analysis of Lower Frequency Recordings

To explore the potential frequency-dependence of the spatial distribution of the source radiation, we repeat the back-projection analysis of the Tohoku-Oki earthquake in two lower frequency bands, 0.125-0.25 Hz and 0.25-0.5 Hz. Fig. A.9 shows a map of the peak energy radiators. Overall the lower frequency results follow the similar down-dip distribution and temporal evolution as the high frequencies (Figure 2.1 of the main text). The results from both arrays remain mutually consistent. However, the lower frequency results are more scattered due to the expected lower resolution of the array processing, which is inversely proportional to the wavelength.

A.7. Analysis of Strong Motion Data

We examine velocity envelopes of strong motion data recorded along the northeastern Honshu coastline in order to identify prominent phases observed at teleseismic distances. We band pass filter the data, integrate, square and sum traces of horizontal components. The resulting velocity envelopes are averaged using a sliding median filter whose length is equal to five times the lower bound of the band pass filter. Fig. A.10a and Fig. A.10b show scaled smoothed velocity envelopes for 0.5-1 Hz and 2.5-5 Hz frequency bands, respectively. We find that the prominent high-frequency bursts from locations that ruptured 33, 85, and 140 seconds after the mainshock are well resolved for frequencies as low as 0.5Hz. This observation is consistent with our results for the 5-10 Hz frequency band presented in the main text.

A.8. Velocity Model

In the analysis of the ground motion data recorded by the K-net and KiK-net seismic networks we use the following 1D model derived from [*Takahashi et al.* 2004] :

Table A.1. 1D velocity model in Japan.

Depth (km)	S-wave velocity (km/s)
0	3.46
16	3.87
32	4.5

A.9. Data Sources

We downloaded the data from the following sources:

USArray: http://www.usarray.org/

European seismic network: http://www.orfeus-eu.org/

K-net: http://www.k-net.bosai.go.jp/

Kik-net: http://www.kik.bosai.go.jp/

Italian network: http://iside.rm.ingv.it/

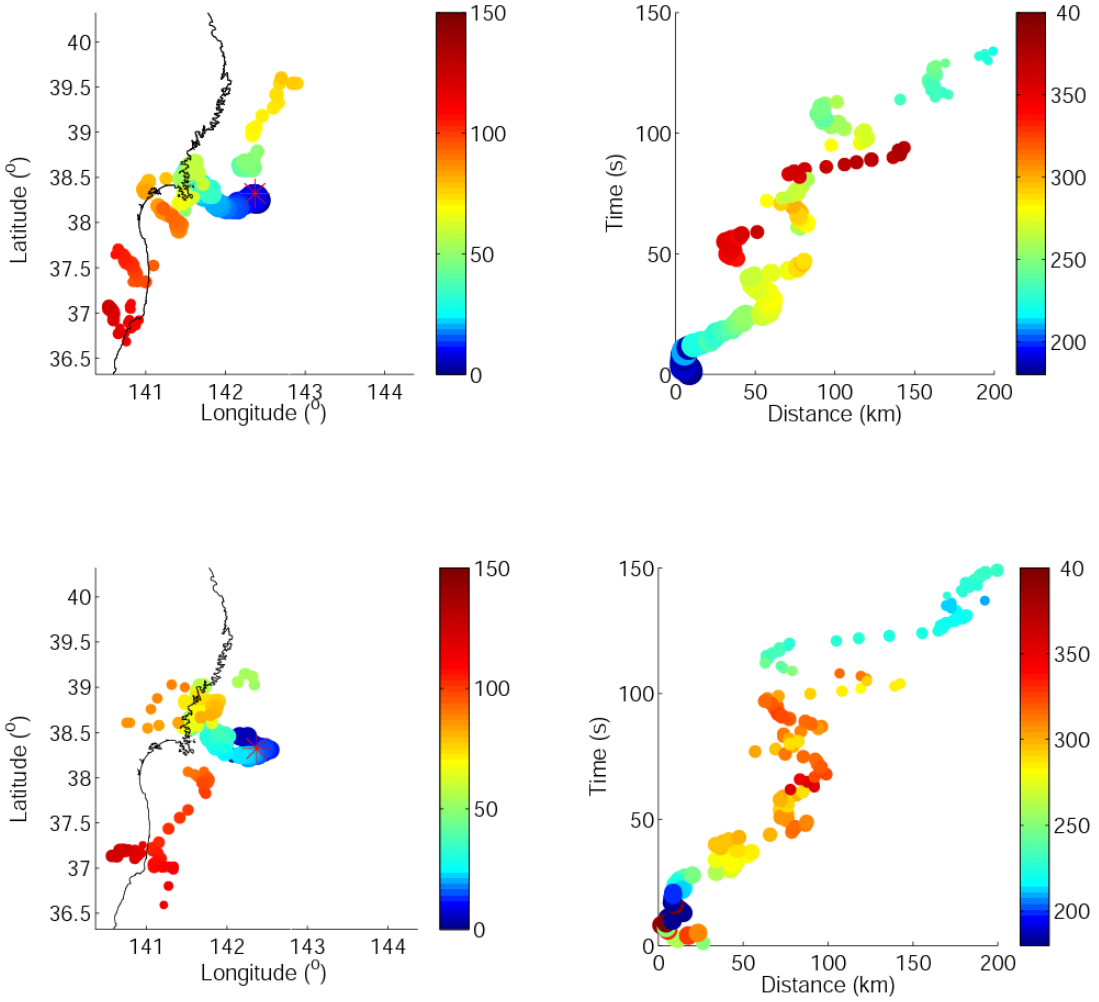

Figure A.1. Back projections using correlation stacking at 0.5-1 Hz. *Left*: location of the strongest HF radiators color coded by rupture time. *Right*: rupture time versus epicentral distance, color coded by azimuth relative to the epicenter. *Top*: results based on European data. *Bottom*: results based on USarray data.

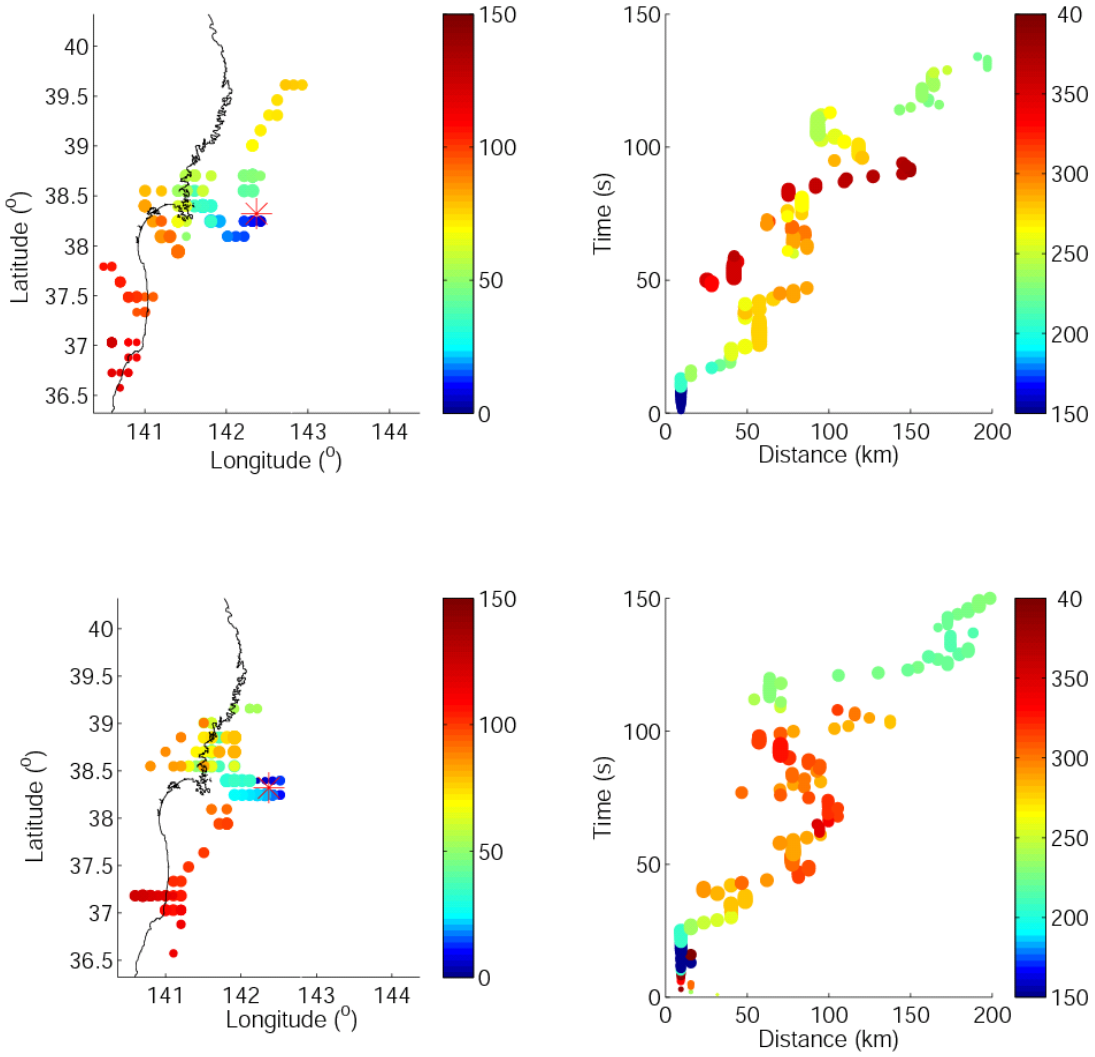

Figure A.2. Back projections using cubic root stacking. Left: location of the strongest HF radiators color coded by rupture time. Right: rupture time versus epicentral distance, color coded by azimuth relative to the epicenter. Top: results based on European data. Bottom: results based on USarray data.

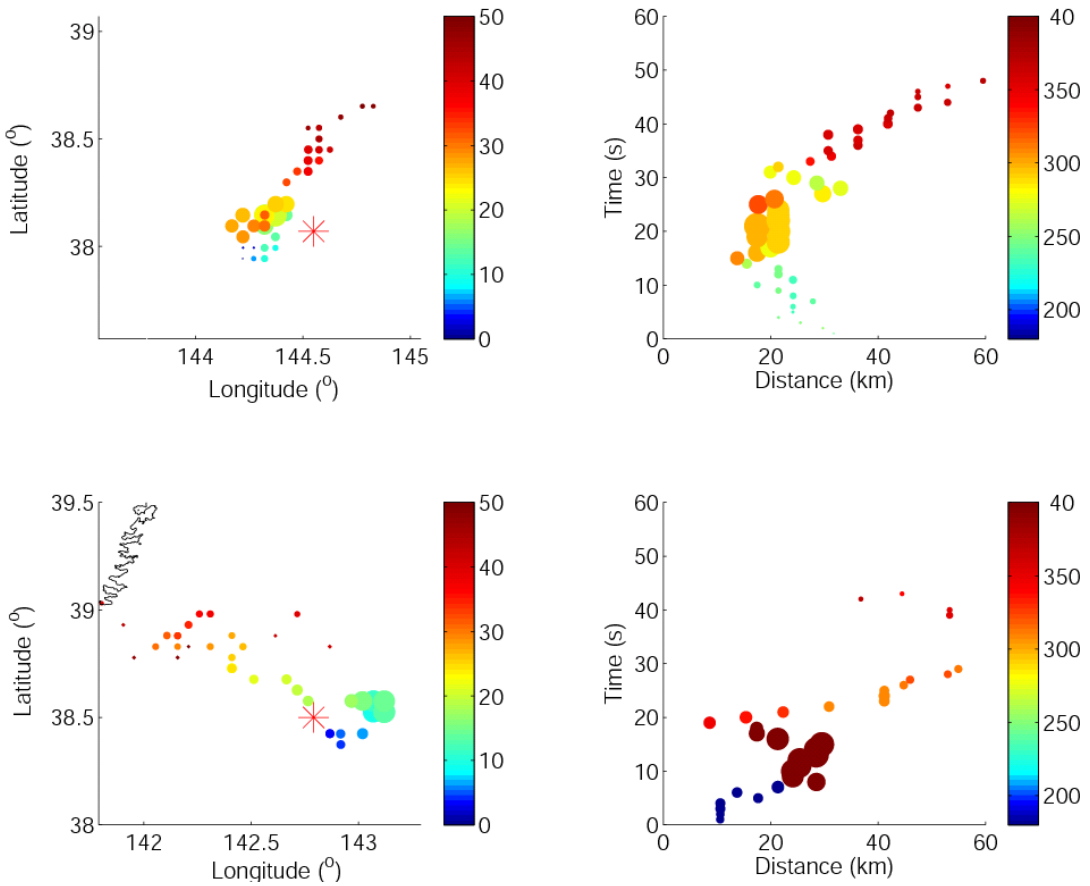

Figure A.3. Foreshocks and aftershocks processed by the MUSIC technique at 0.5-1Hz, based on USArray data. Same convention as as in figures S1 and S2. Top: the March 9 M7.2 foreshock. Bottom: the March 11 M7.1 aftershock.

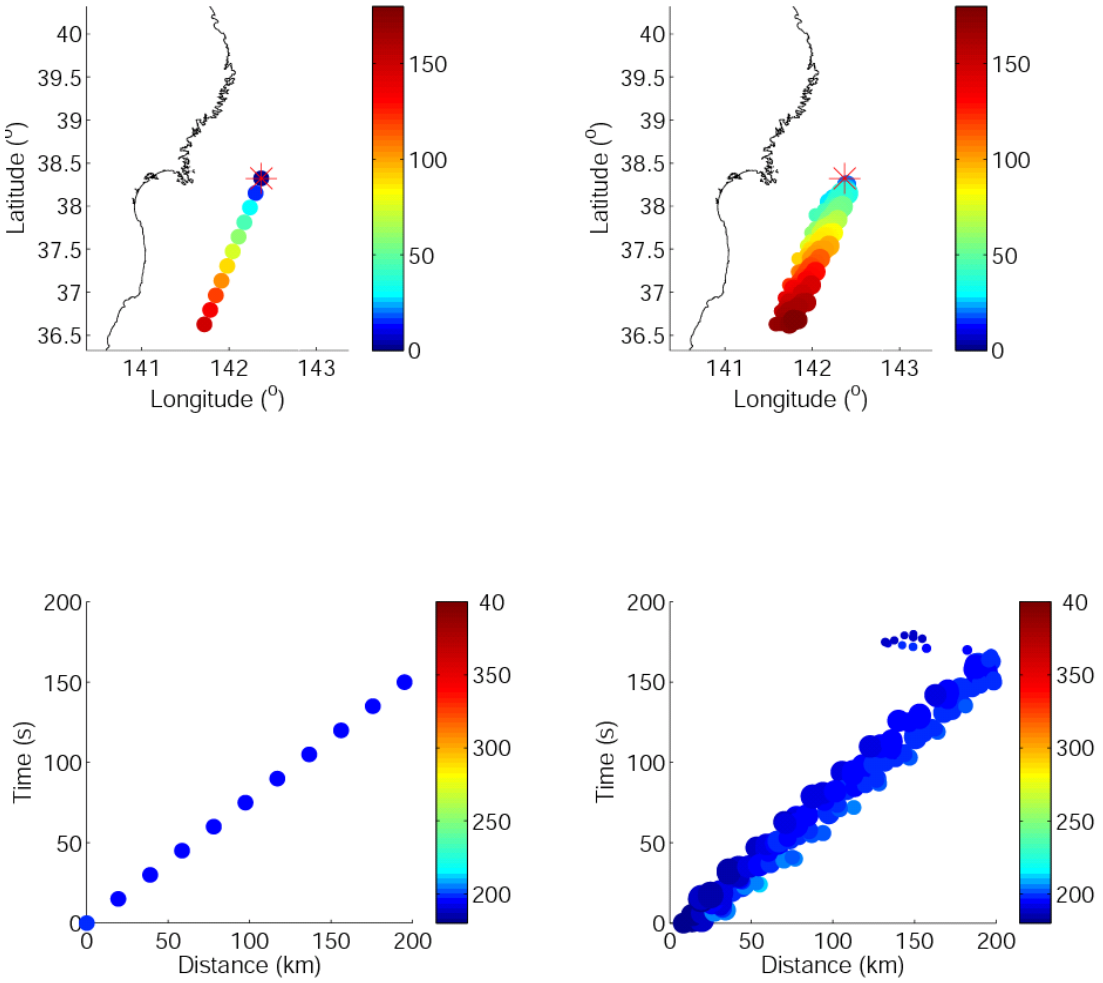

Figure A.4. Synthetic test 1. Same conventions as in previous figures. Left: synthetic source scenario. Right: source model recovered by MUSIC back-projection.

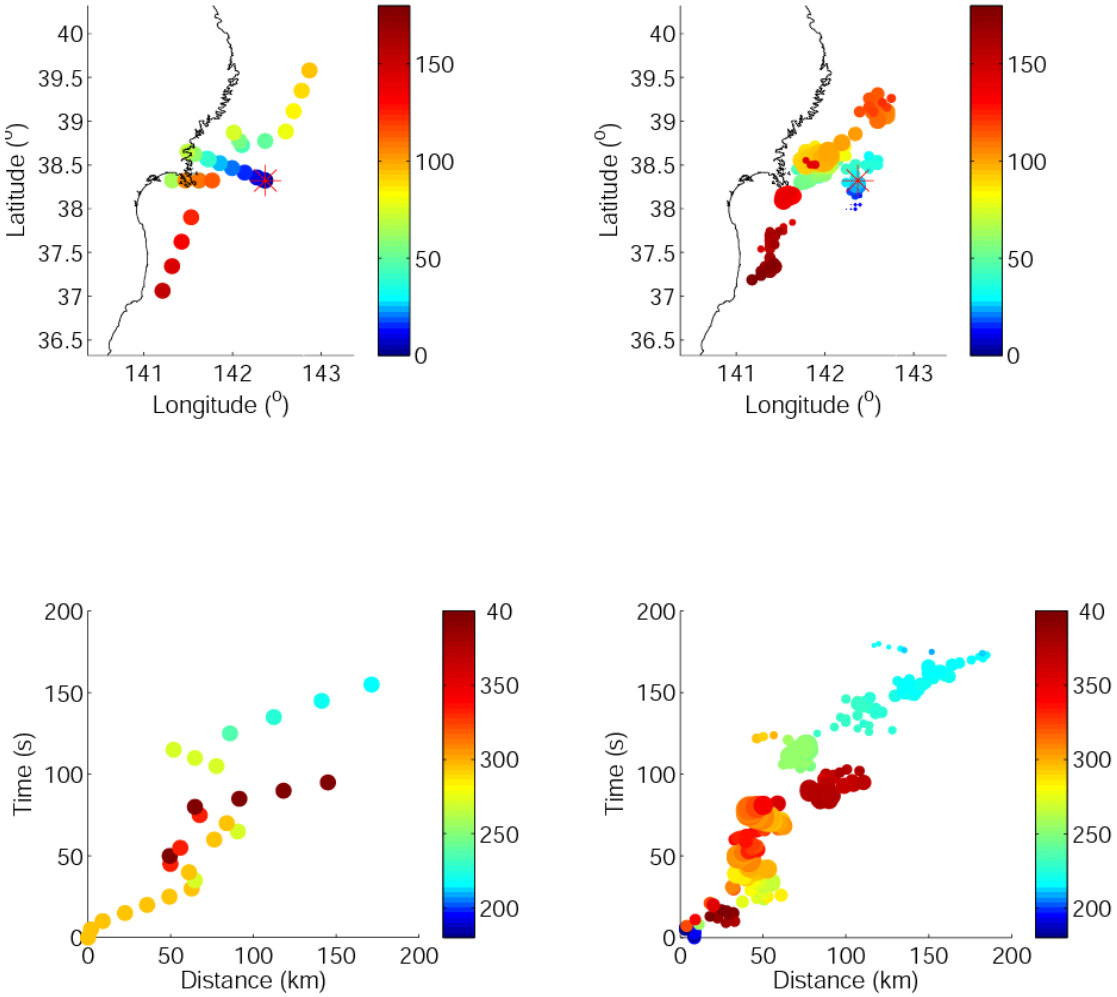

Figure A.5. Synthetic test 2. Same conventions as in previous figures. Left: synthetic source scenario. Right: source model recovered by MUSIC back-projection.

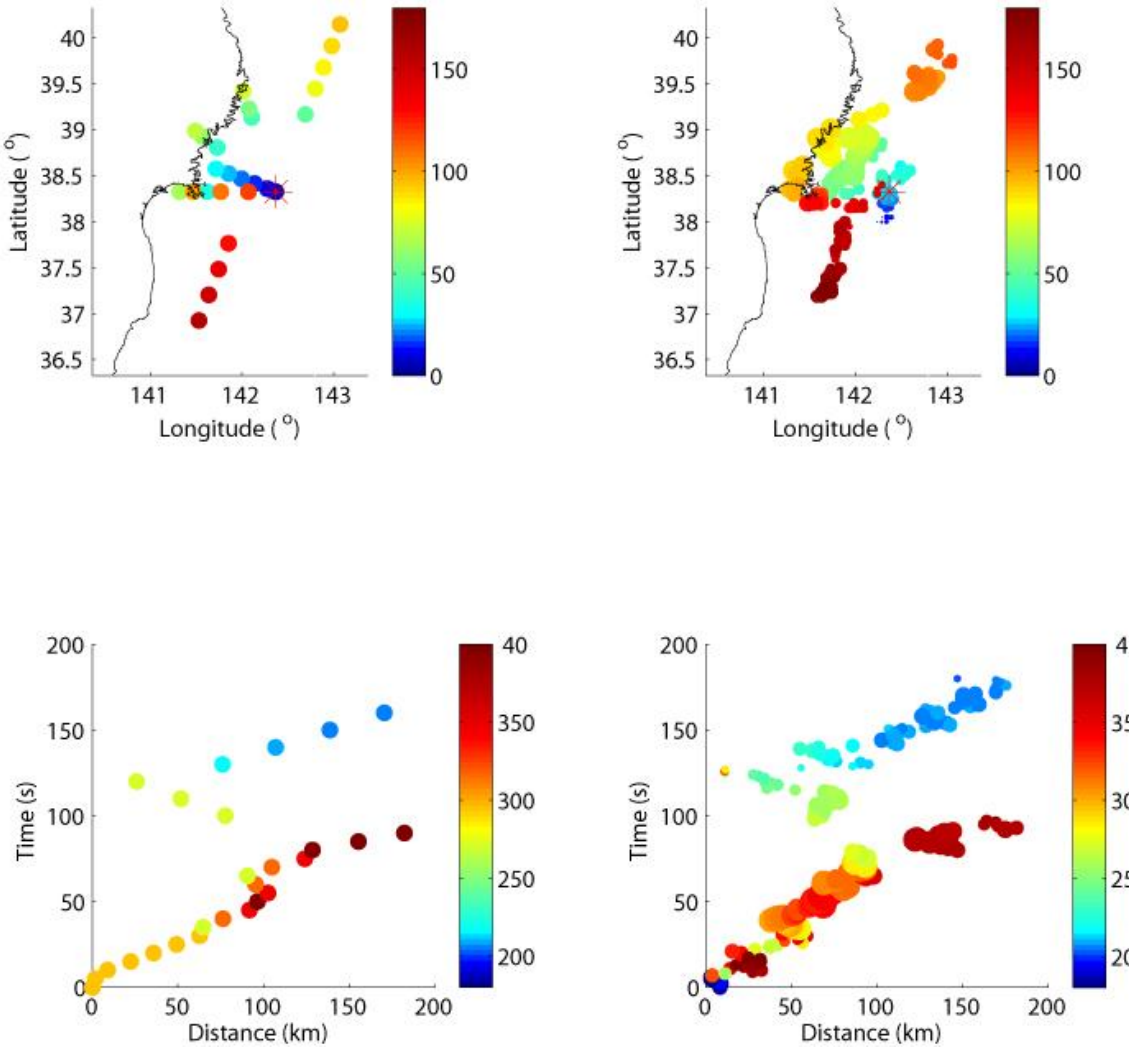

Figure A.6. Synthetic test 3. Same conventions as in previous figures. Left: synthetic source scenario. Right: source model recovered by MUSIC back-projection.

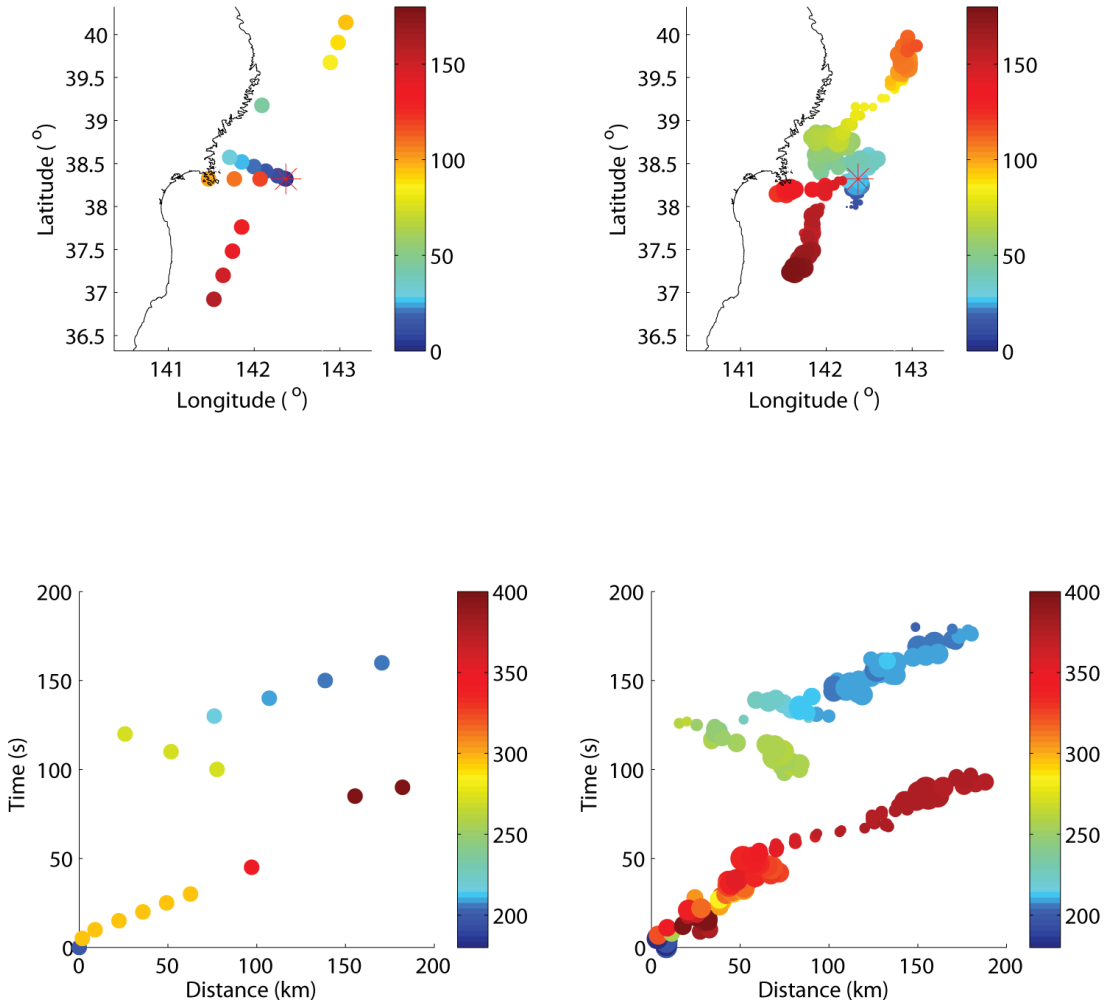

Figure A.7. Synthetic test 4. Same conventions as in previous figures. Left: synthetic source scenario. Right: source model recovered by MUSIC back-projection.

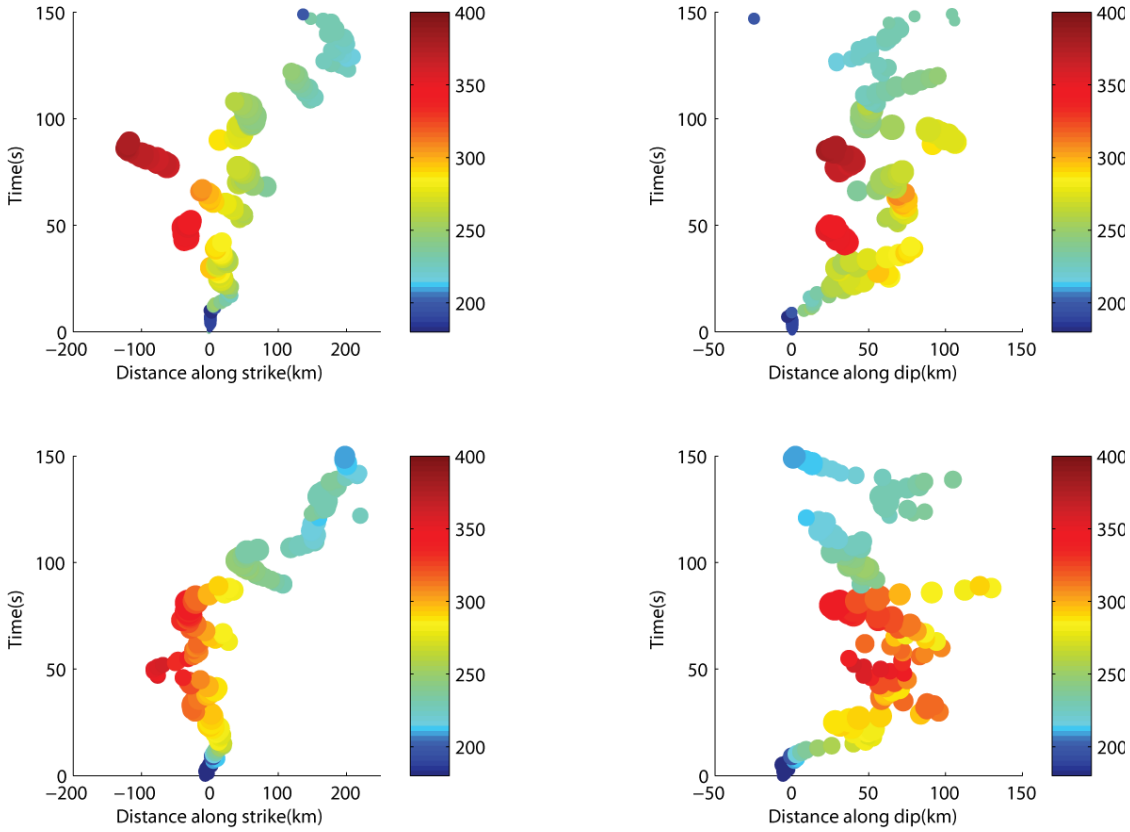

Figure A.8. Rupture time versus along strike and dip distance Left: rupture time versus along strike distance, color coded by azimuth relative to the epicenter. Right: rupture time versus along dip distance, color coded by azimuth relative to the epicenter. Top: results based on European data. Bottom: results based on USarray data.

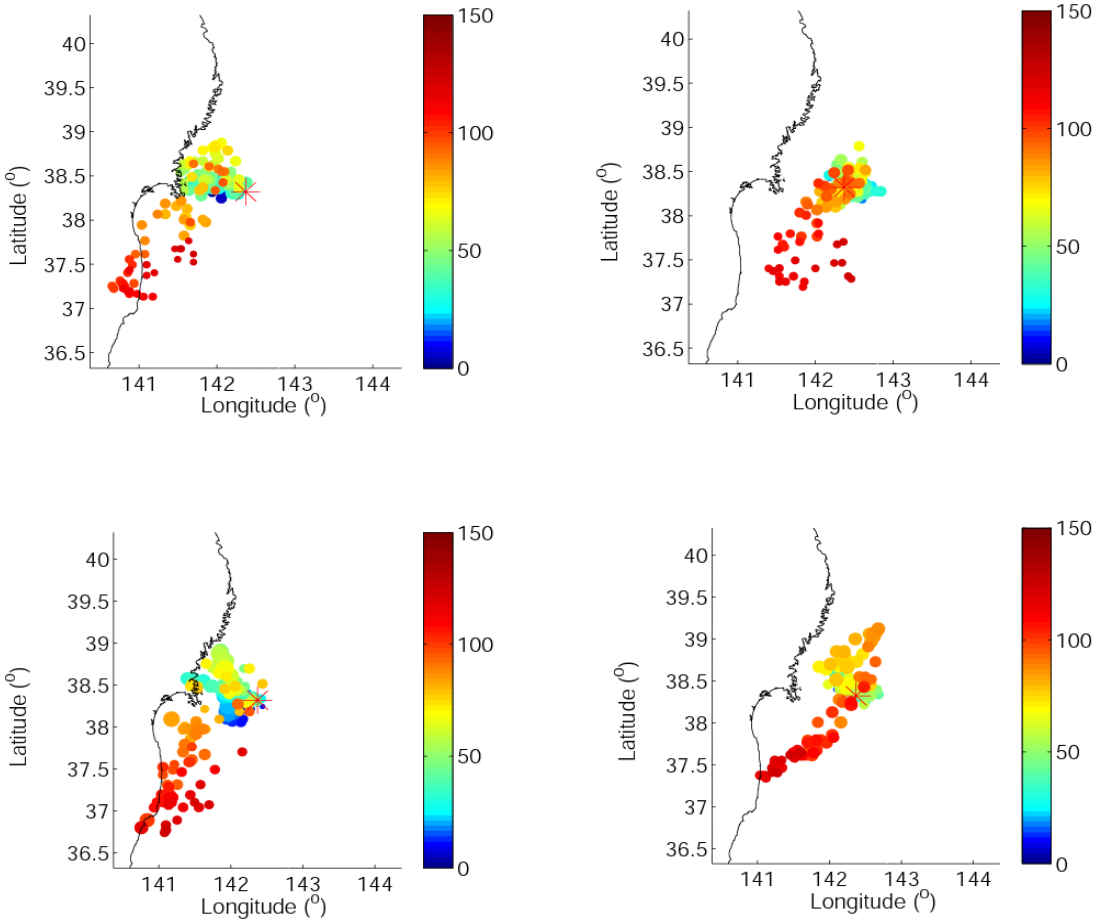

Figure A.9. Array analysis of lower frequency recordings. Location of the strongest radiators color coded by rupture time. Top: 0.125 to 0.25 Hz. Bottom: 0.25 to 0.5 Hz. Left: USarray. Right: European network.

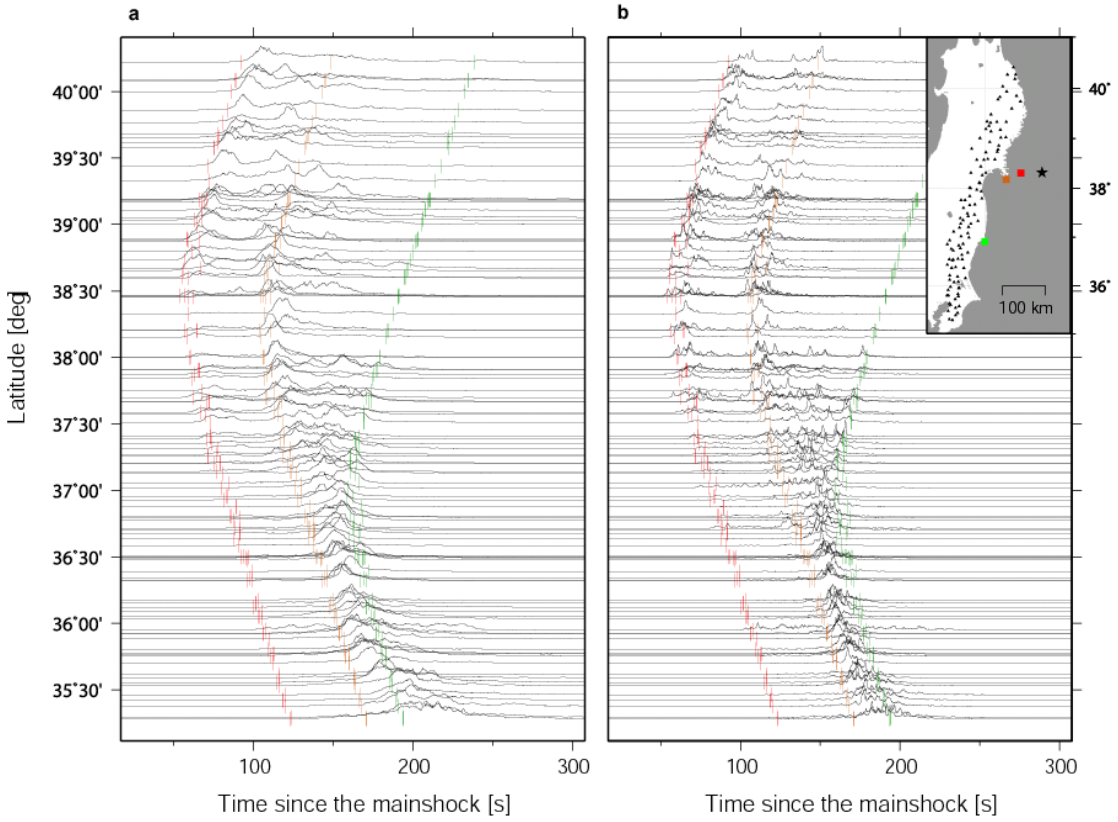

Figure A.10. Strong motion recordings at lower frequency band. Smoothed 0.5-1 Hz (left) and 2.5-5 Hz (right) velocity envelopes of strong motion data recorded along the north-eastern Honshu coastline. Traces are scaled by their maximal amplitude. Star and triangles in the inset map denote the epicentral location of the Tohoku Mw 9.0 mainshock (USGS catalog reference) and the recording stations, respectively. Red, yellow and green vertical bars along the time series indicate the the S-wave travel times from asperities that ruptured 33, 85, and 140s after that mainshock, respectively. The asperities locations are indicated by squares of corresponding colors in the inset map.

A p p e n d i x B

SUPPLEMENTARY MATERIALS OF CHAPTER 3

B.1. Back Projection Data Selection and Processing

We processed the seismic data recorded by various seismic arrays at epicentral distances between 30 and 90 degrees. The large aperture and dense spacing of the European (www.orfeus-eu.org; Figure B.1) and Japanese Hi-net networks (www.hinet.bosai.go.jp; Figure B.2) provided fine spatial resolution for this event. The two arrays are located at almost orthogonal azimuths relative to the source area, providing complementary views of the rupture process. The P waveforms were filtered between 0.5 and 1 Hz, selected by their signal-to-noise ratio and by the mutual coherency of their initial 10 seconds, and then aligned by multichannel cross-correlation. We applied the MUSIC back-projection technique [*Meng et al.* 2011; *Meng Ampuero Sladen et al.* 2012] on sliding windows ten seconds in length. This source imaging technique allows tracking the migration of the multiple sources of high-frequency (HF) radiation of an earthquake rupture. Our particular approach combines a high-resolution array processing technique [*Schmidt* 1986; *Goldstein and Archuleta* 1991] with multitaper cross-spectral estimation [*Thomson* 1982] to achieve higher resolution than conventional beamforming. Adopting a "reference window" strategy avoids the systematic "swimming" artifact [*Meng Ampuero Luo et al.* 2012]. The MUSIC pseudospectrum is back-projected into the off-Sumatra region based on P travel times computed by the Tau-P toolkit and the IASP91 model [*Snoke* 2009].

B.2. Resolution and Uncertainty of Back Projection Source Imaging

We conducted several analyses to understand the strengths and limitations of our back-projection method, as specifically applied to the European and Japanese arrays. We address two different array

performance criteria. The spatial resolution of an array is defined as the capability to separate two simultaneous sources of different location: the resolution length is the minimum distance between sources that can be distinguished without ambiguity. The spatial uncertainty of an array is defined as the error in estimates of source location for isolated sources.

The resolution length that can be achieved with linear beamforming is conventionally estimated as the width at half peak amplitude of the main lobe of the array response function (ARF, 35). Figs. S4 and S5 show the ARFs of the Japanese and the European networks back-projected into the off-Sumatra region. The European ARF is relatively compact with resolution lengths of 35 km in the N-S direction and 65 km in the E-W direction. These are one order of magnitude smaller than the source dimension of the M8.6 off-Sumatra event, which indicates that the overall rupture process can be resolved as long as there is adequate signal coherence. The Japanese Hi-Net array has a larger and more anisotropic ARF, with resolution lengths of 450 km in the N-S direction and 70 km in the E-W direction. This helps explaining why the early separation of the bilateral rupture fronts on fault B is imaged by the European array (movie B.2) but the two fronts appear simultaneously in the Hi-Net images only when they reach the ends of fault B.

In back-projection source imaging with linear beamforming, the estimation of source location is based on identifying the peak position of an image that is smeared by the array response. The Cramer-Rao bound, a theoretical estimate of the upper bound of uncertainty of an estimator, indicates that the source location uncertainty is proportional to the resolution length of the ARF and inversely proportional to the signal-to-noise ratio of the images (SNR), defined as the ratio between the main peak amplitude and the mean amplitude of the background peaks of the image. The SNR depends on both the signal quality (noise and multipath) and the station density (sidelobe ampli-

tude). The Hi-Net array has a particularly large SNR due to its small ambient noise level (borehole stations) and extremely dense spacing (~20 km).

However, due to the nonlinearity of the MUSIC technique, its resolution cannot be fully appreciated by considering the ARF. Typically, the resolution length of MUSIC is at least two times smaller than the beamforming resolution length [*Meng Ampuero Sladen et al.* 2012]. Moreover, the resolution analysis based on the ARF assumes perfect signal coherence. In practice, we quantify the uncertainty of back-projection of Hi-Net data by bootstrapping the back-projection of a M6.1 aftershock that occurred on April 21, 2012 at 93.39 ° E and 2.22 ° N. The aftershock seismograms are first aligned by the initial 3 s of the P-wave arrival. The noise at each station is computed as the waveform residual with respect to the array-stacked waveform. The noise is shuffled by randomizing its Fourier phase spectrum, then added back to the stack. One thousand synthetic realizations of the aftershock array recordings plus noise are then back-projected considering the 10s long window that begins at the initial arrival. The resulting back-projection locations are shown in Fig. S6. The bootstrap 95% confidence ellipse is elongated along the N-S direction with a major axis length of 9.5 km and minor axis length of 2.8 km. Unfortunately, the recording of this aftershock at the European array is too weak to be used in the 0.5-1 Hz frequency band.

To further understand the performance of the back-projection on complicated ruptures, we conduct two synthetic earthquake scenarios. To include key characteristics of the real wavefield, such as the decay of waveform coherence as a function of time, we use the M6.1 event as empirical Green's function. Inspired by our final back-projection result, particularly a jump from the fault C to fault D imaged with the Hi-Net array, we test scenarios of bilateral rupture on Fault A and B and unilateral rupture on Fault C with (Fig. B.7) or without (Fig. B.8) an additional fault D. We consider a uniform distribution of subsources, regularly located every 15 km along each fault. The rupture times

correspond to an assumed rupture speed of 2.5 km/s. The MUSIC back-projection technique recovers the location and timing of the scenario sources very well. The uncertainty of the peak locations is less than 20 km, which is reasonably good considering the coda and interference between sub-sources. These synthetic tests indicate that the jump between faults C and D is resolvable by the Hi-Net array.

B.3. Multiple Point Source Analysis

Seismic waves from the 2012 Sumatra earthquake sequence were recorded by a large number of broadband seismic stations enabling robust and reliable characterization of the overall source characteristics at long periods. For the Mw=8.6 event, 113 channels were used to perform a multiple point source inversion. We inverted simultaneously for the moment tensors of the subevents, their locations (latitude, longitude, depth) and time delays using a global sampling approach. The inversion is performed using the W-phase waveforms at shorter period (150-500 s) than the usual practice for single point source inversions of Mw>8.0 earthquakes. The optimal centroid depth of the mainshock is 30 km. Our preferred model is a two point source solution which is presented on Fig. 3.1.

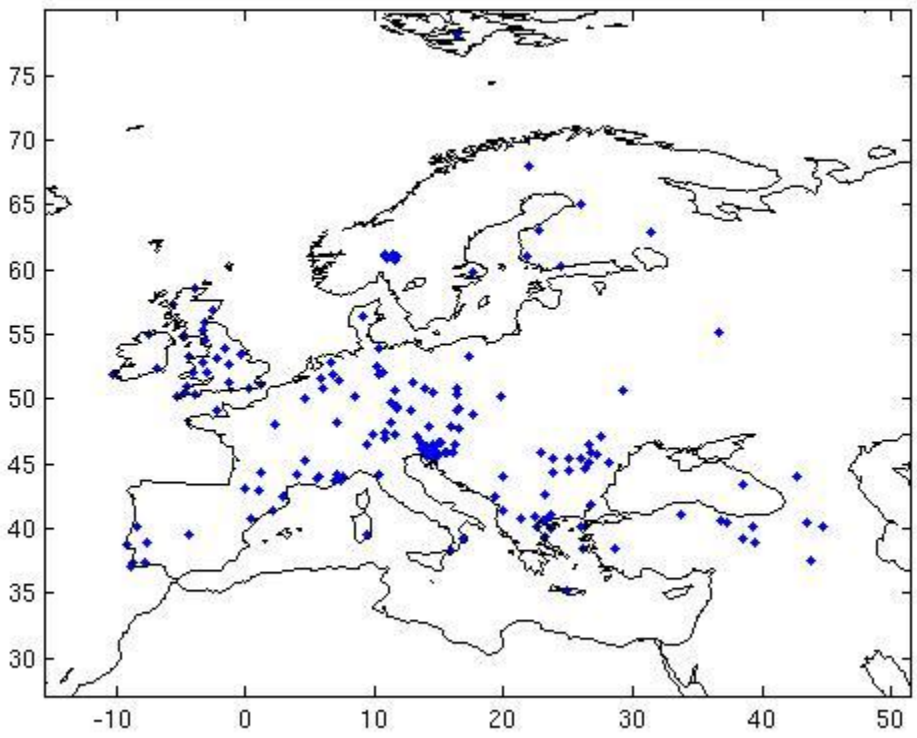

Figure B.1. Selected stations used for back-projection from the European network.

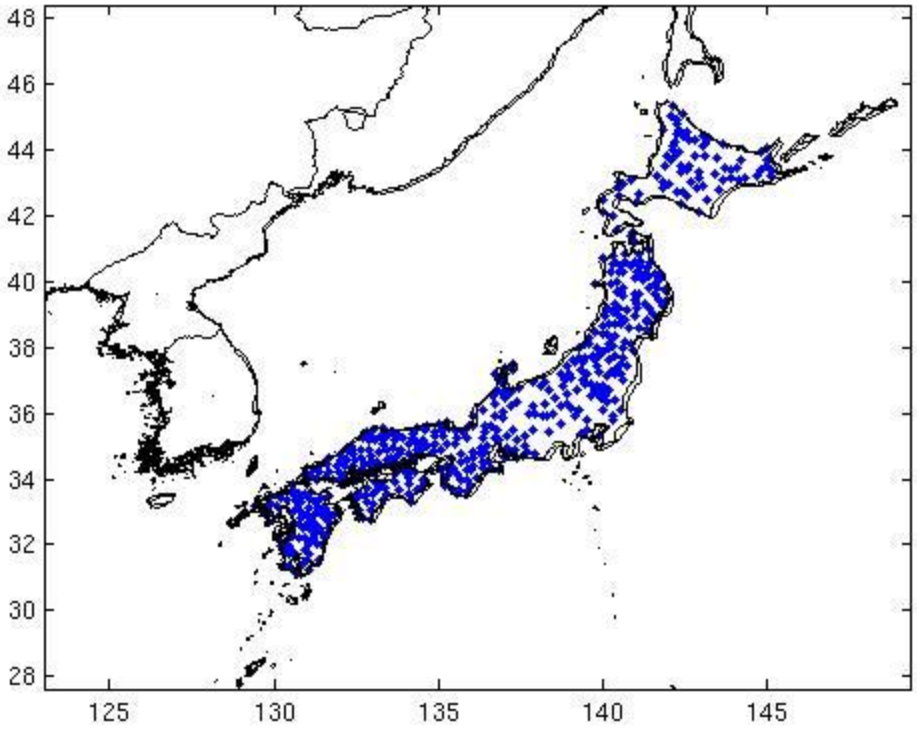

Figure B.2. Selected stations for back-projection from the Hi-Net (Japan) network.

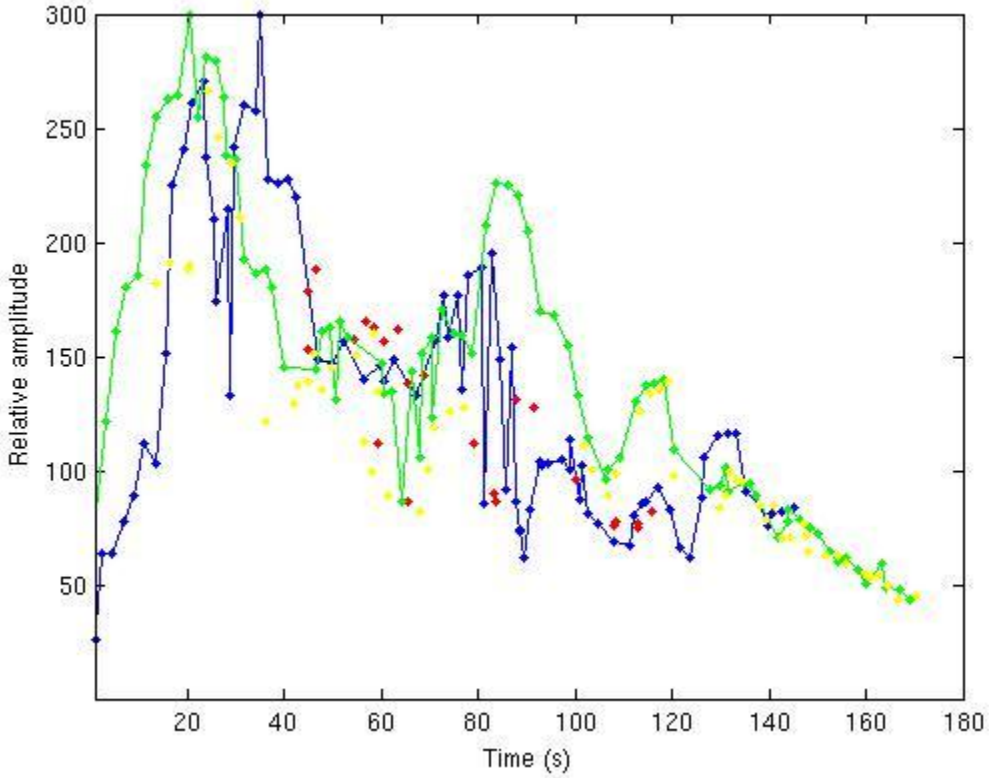

Figure B.3. Beamforming source amplitude evaluated at the location of the HF radiators obtained by MUSIC as a function of time, obtained with the European array (green) and Japanese Hi-Net array (blue). The scale is normalized by the beamforming amplitude of the initial window. The yellow and red dots indicate the amplitude of the secondary sources for the European and Japanese arrays, respectively.

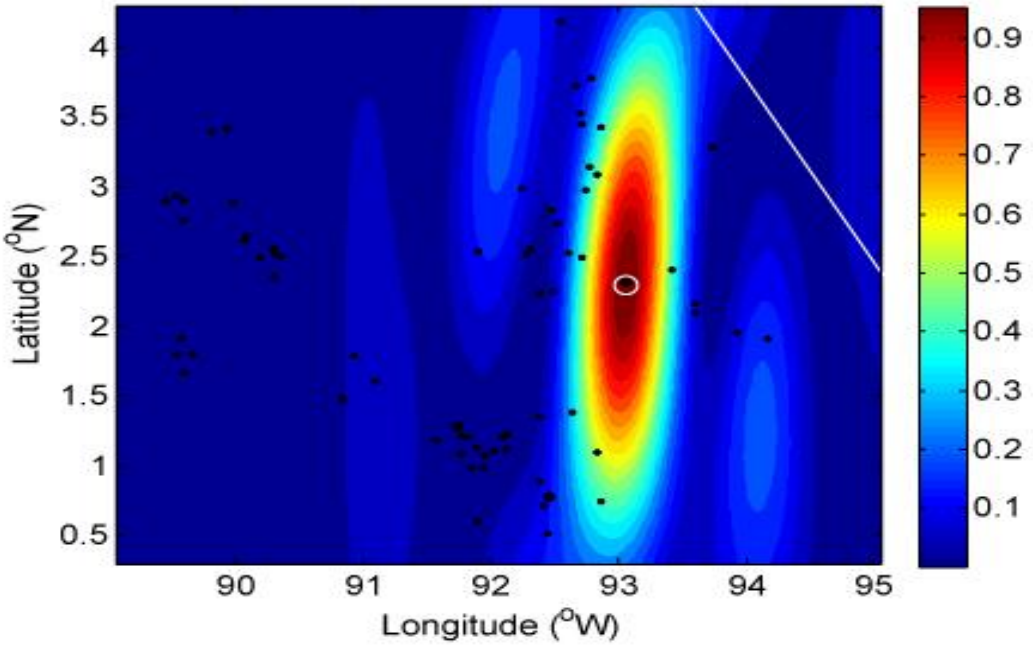

Figure B.4. Array response pattern of the Japanese Hi-Net array back-projected into the off-Sumatra earthquake region, plotted in map view. The color scale indicates the power of the array response, normalized by its peak value. The white line denotes the trace of the Sumatra trench. The white circle is the location of the epicenter. The black dots are early aftershocks that occurred within 24 hours of the mainshock.

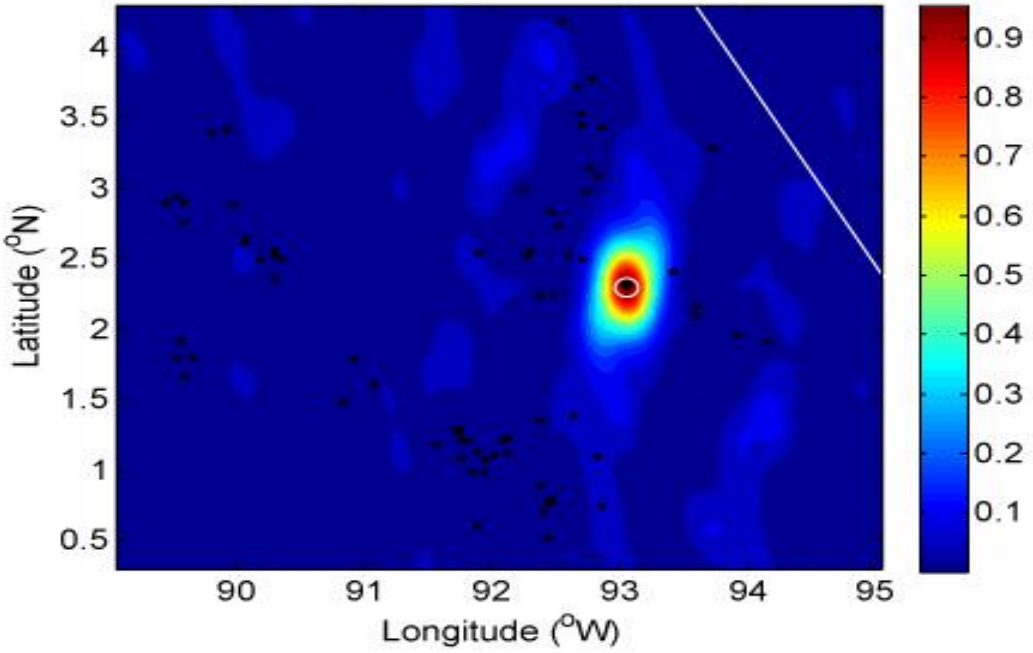

Figure B.5. Array response pattern of the European network. The convention is the same as in the previous figure.

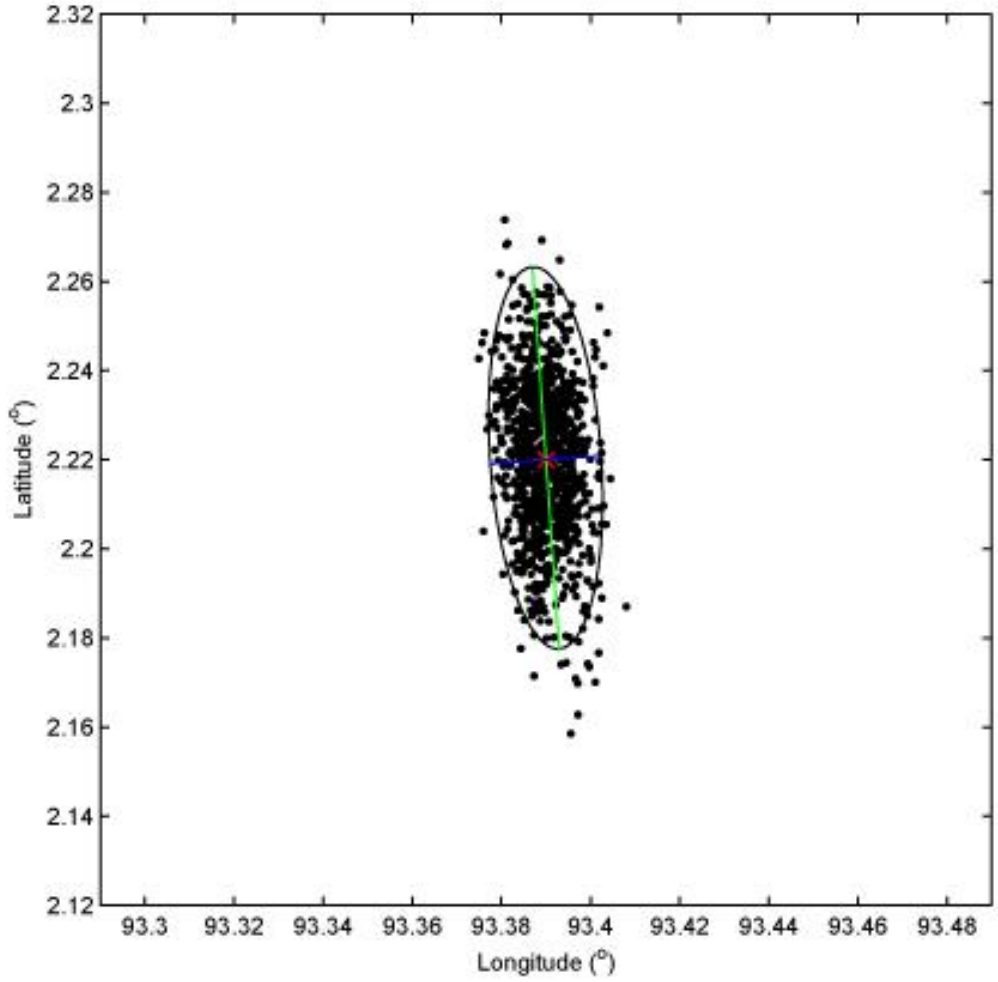

Figure B.6. Uncertainty of the back-projection. A M6.1 aftershock that occurred on April 21, 2012 is used here as an empirical Green's function. The red asterisk denotes the hypocenter. The black dots are the back-projection of the bootstrapped aftershock recordings. The ellipse is the 95% confidence interval. It has a 9.5 km long major axis (blue line) and 2.8 km long minor axis (green line).

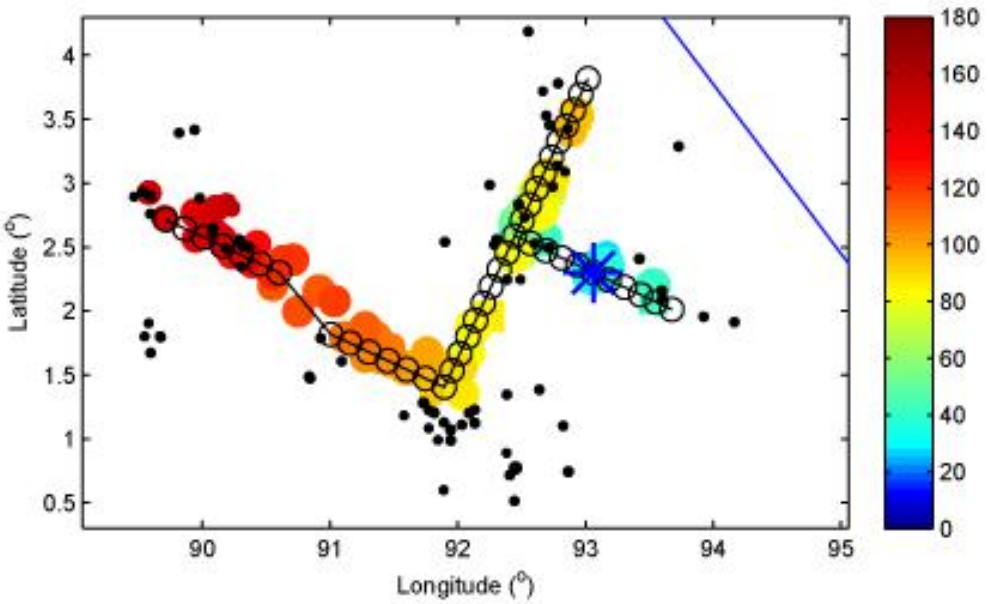

Figure B.7. Back-projection of a synthetic rupture scenario. The black circles are the synthetic sources. The colored circles are the recovered back-projection locations color-coded by time. The black dots are the early aftershocks that occurred within 24 hours of the mainshock.

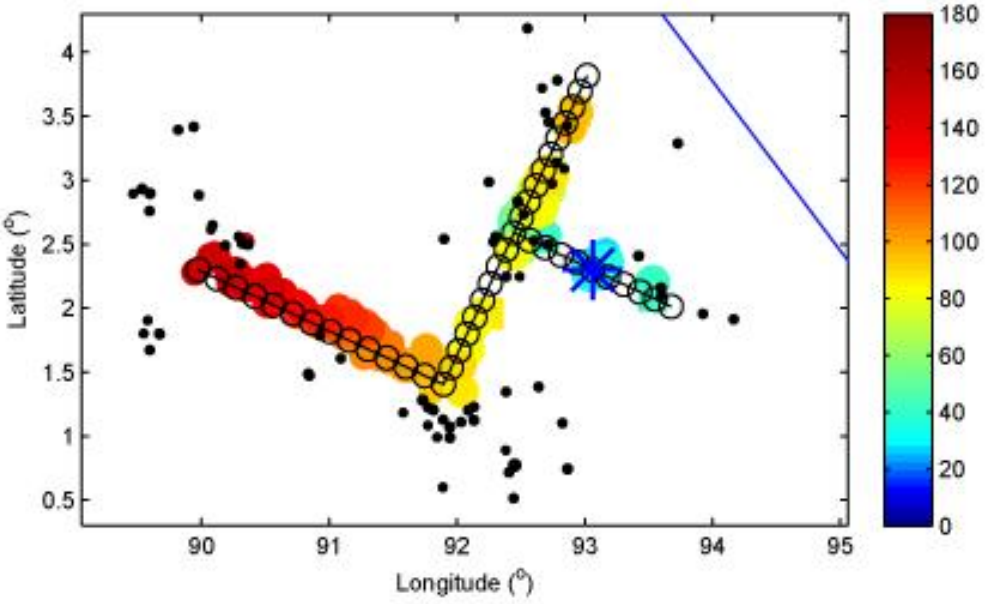

Figure B.8. Back-projection of a synthetic rupture scenario without offset between faults C and D. The convention of the figure is the same as in the previous one.

Movie B.1: The movie shows the raw results of back-projection source imaging based on teleseismic data from European networks. Warm colors indicate the positions of the high frequency (0.5 to 1 Hz) radiation back-projected onto the source region based on IASP91 travel times [*Snoke* 2009]. The sliding window is 10 s long and the origin time is 08:38:37, 04-12-12 (UTC). The beginning of the sliding window is set to be 5 s before the initial P-wave arrival. Colors indicate the amplitude of the MUSIC pseudospectrum on a logarithmic scale (dB) after subtracting the background level and rescaling the maximum to the linear beamforming power in each frame separately. The white star is the mainshock epicenter and the green circles are the epicenters of the first day of aftershocks from the NEIC catalog. Time relative to hypocentral arrival time is shown on top. The trench and coastlines are shown by white curves.

Movie B.2: Back-projection source imaging based on teleseismic data from Japanese networks. Same convention as the previous movie.

A p p e n d i x C

SUPPLEMENTARY MATERIALS OF CHAPTER 4

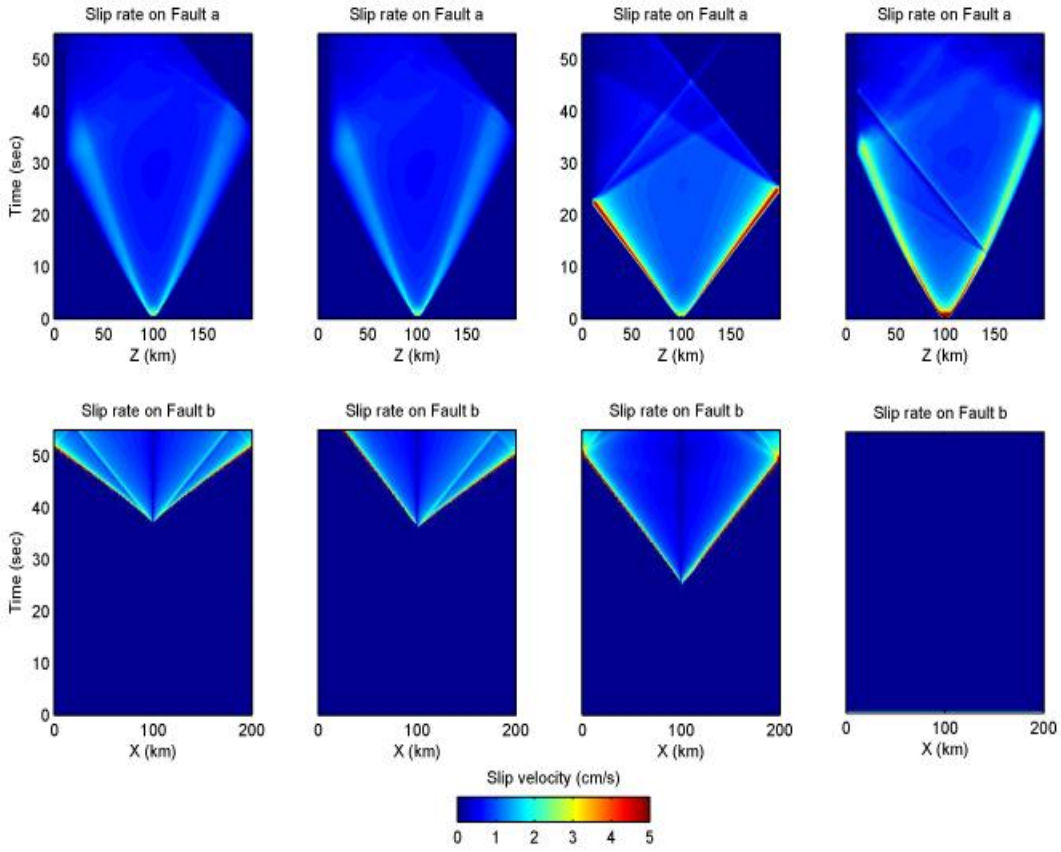

Figure C.1. The slip rate of models with same parameters as in Figure 4.3 except that the dilatational branch fault **bd** is unlocked. Fault **bc** in Model 3 fails to break in Figure 4.3 but broke here due to the triggering by **bd**.

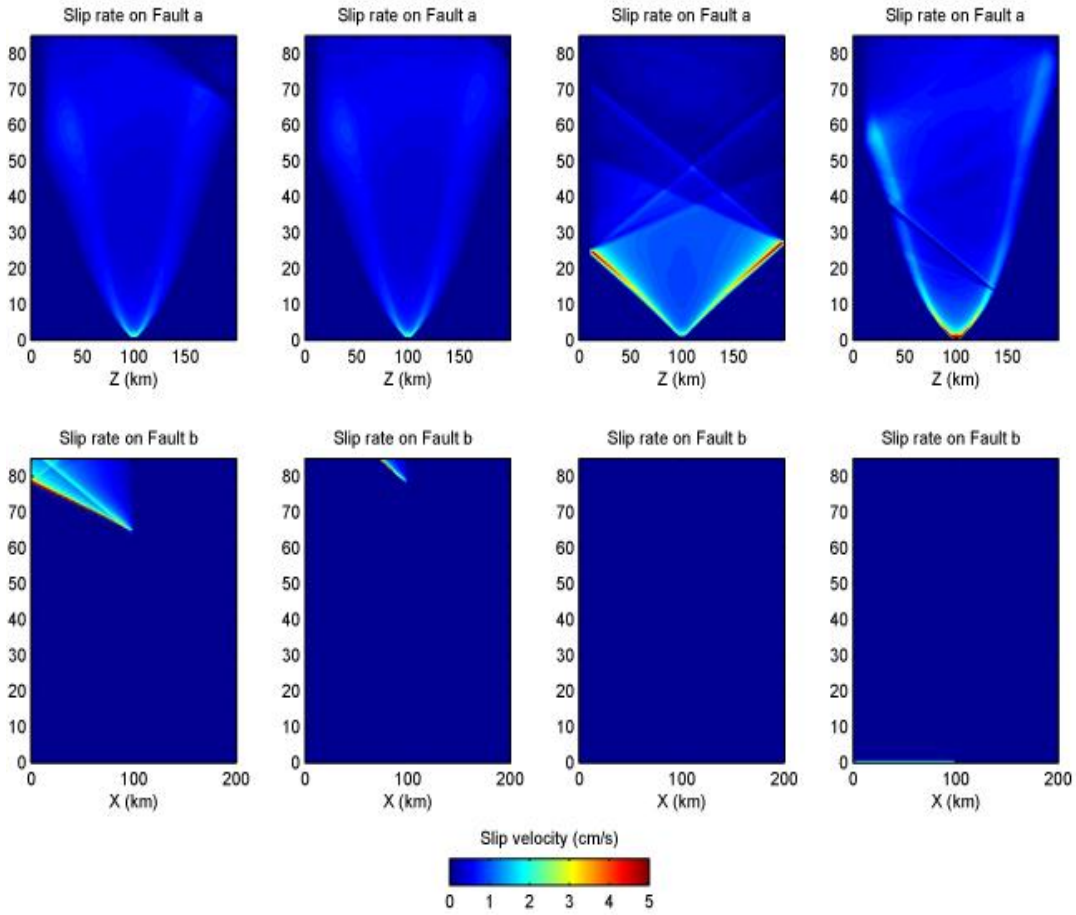

Figure C.2. The Slip rate of models with smaller rupture speed and larger stress drop adjusted to scenario of Fault A. The simulation results remain the same as shown in figure 4.3.

Model index	Mu_s	Mu_d	C	Sigma0	Tau0	Vr/Vs	d_Tau	Dc’
1	0	0	42 Mpa	250 Mpa	42 Mpa	0.29	17 Mpa	3.2e-3
2	0.2	0.1	0	250 Mpa	42 Mpa	0.29	17Mpa	3.2e-3
3	0.2	0.1	0	250 Mpa	42 Mpa	1	17 Mpa	0(Dc=5 m)
4	0.6	0.4	0	250 Mpa	115 Mpa	0.29	17 Mpa	1.5e-3

Table C.1. Parameters of the 4 models shown in figure C.2

A p p e n d i x D

SUPPLEMENTARY MATERIAL OF CHAPTER 5

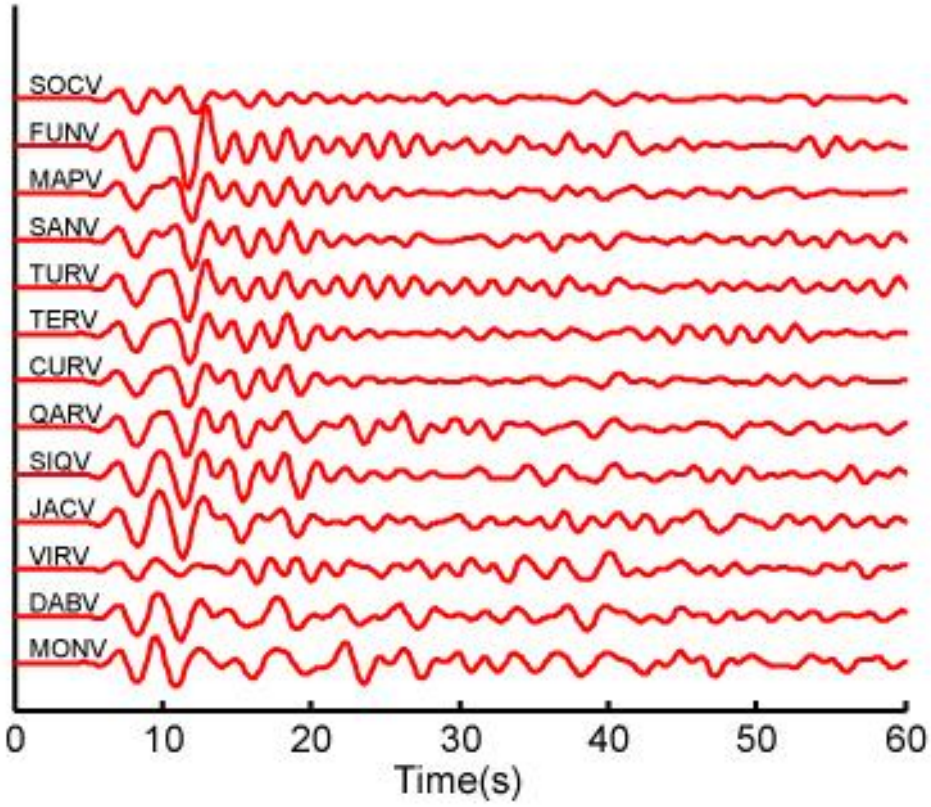

Figure D.1. Synthetic seismograms at the VNSN. The top figure (a) shows the vertical component of the synthetic seismograms of the mainshock filtered from 0.2 to 0.7 Hz, assuming a point source with mechanism given by the CMT solution.

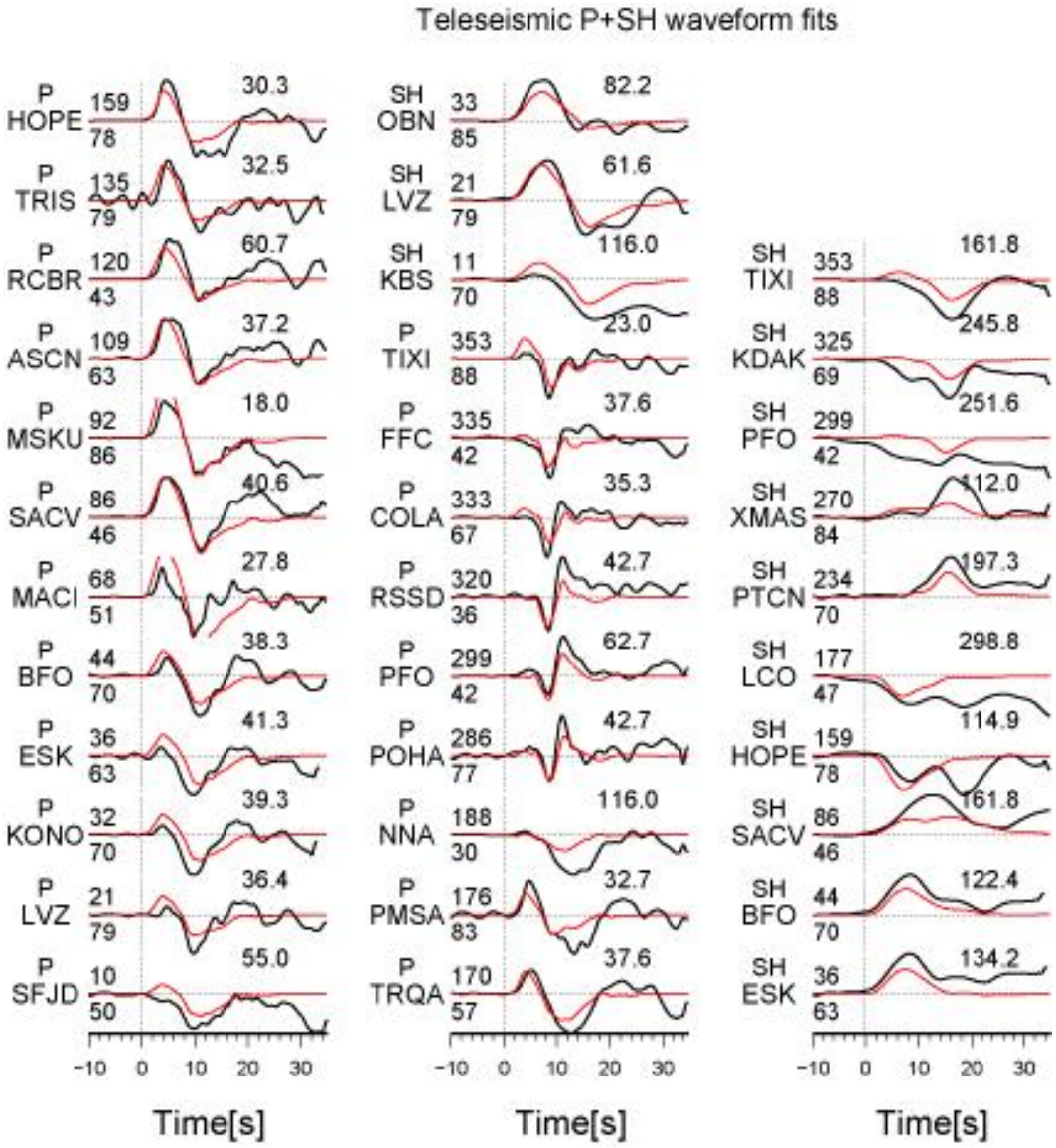

Figure D.2. Fit of the teleseismic P and SH waveforms for the kinematic slip model. Comparison between the observed (black) and predicted (red) waveforms computed for our preferred joint kinematic slip model. The P and SH waveforms are sorted with increasing azimuth angle (number above the beginning of each waveform, number below is the azimuthal distance). The maximum amplitude of the observed seismograms is indicated above the end of each waveform.

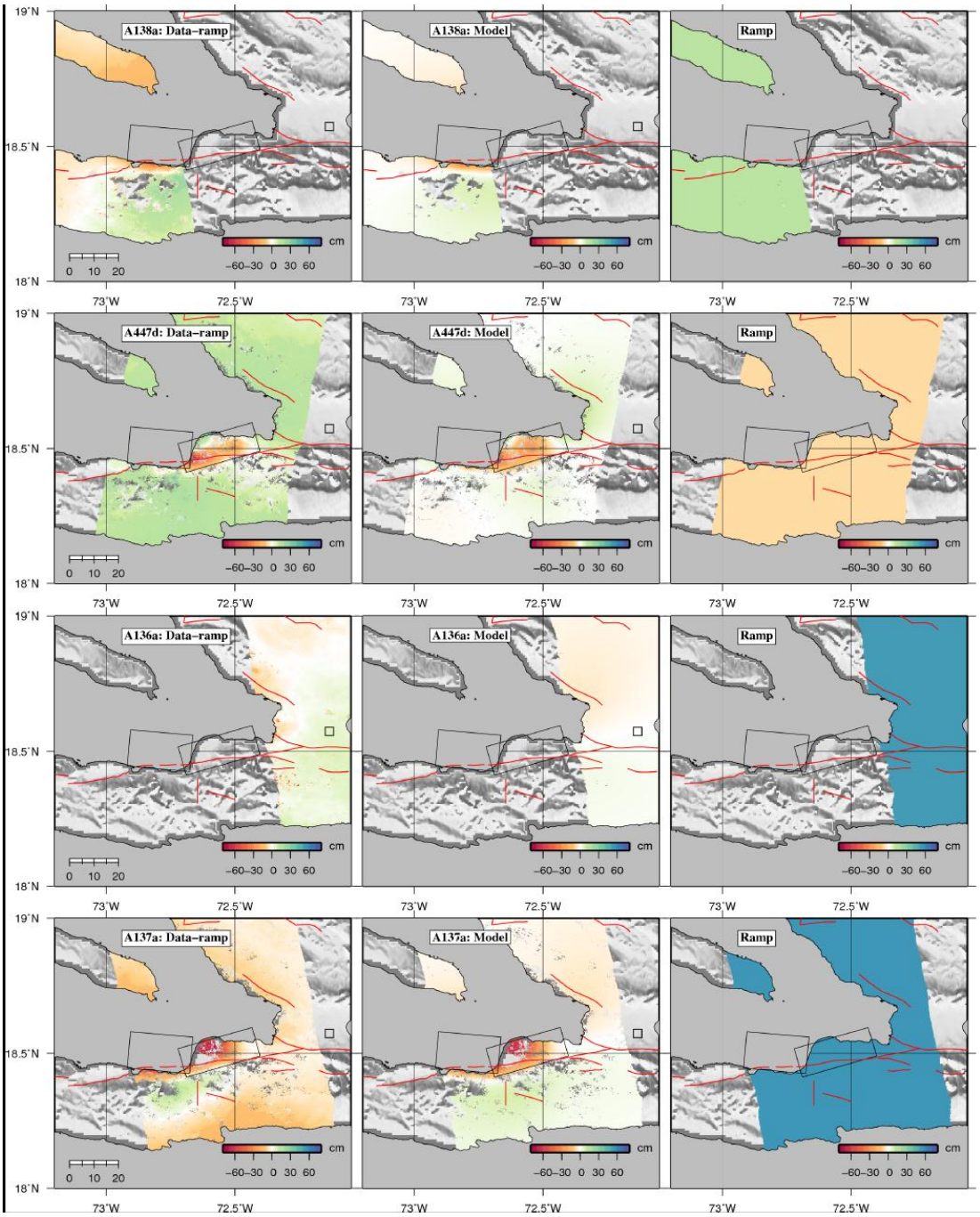

Figure D.3. Comparison of the unwrapped InSAR images for the kinematic slip model.

Each row is composed of the observed minus the ramp (left) and predicted (middle) motion in the line-of-sight of the satellite, and the amplitude of this constant ramp correction (right). The satellite track number is indicated in the top-right corner of the images with the last letter indicating whether this is an (a)scending or (d)escending track.

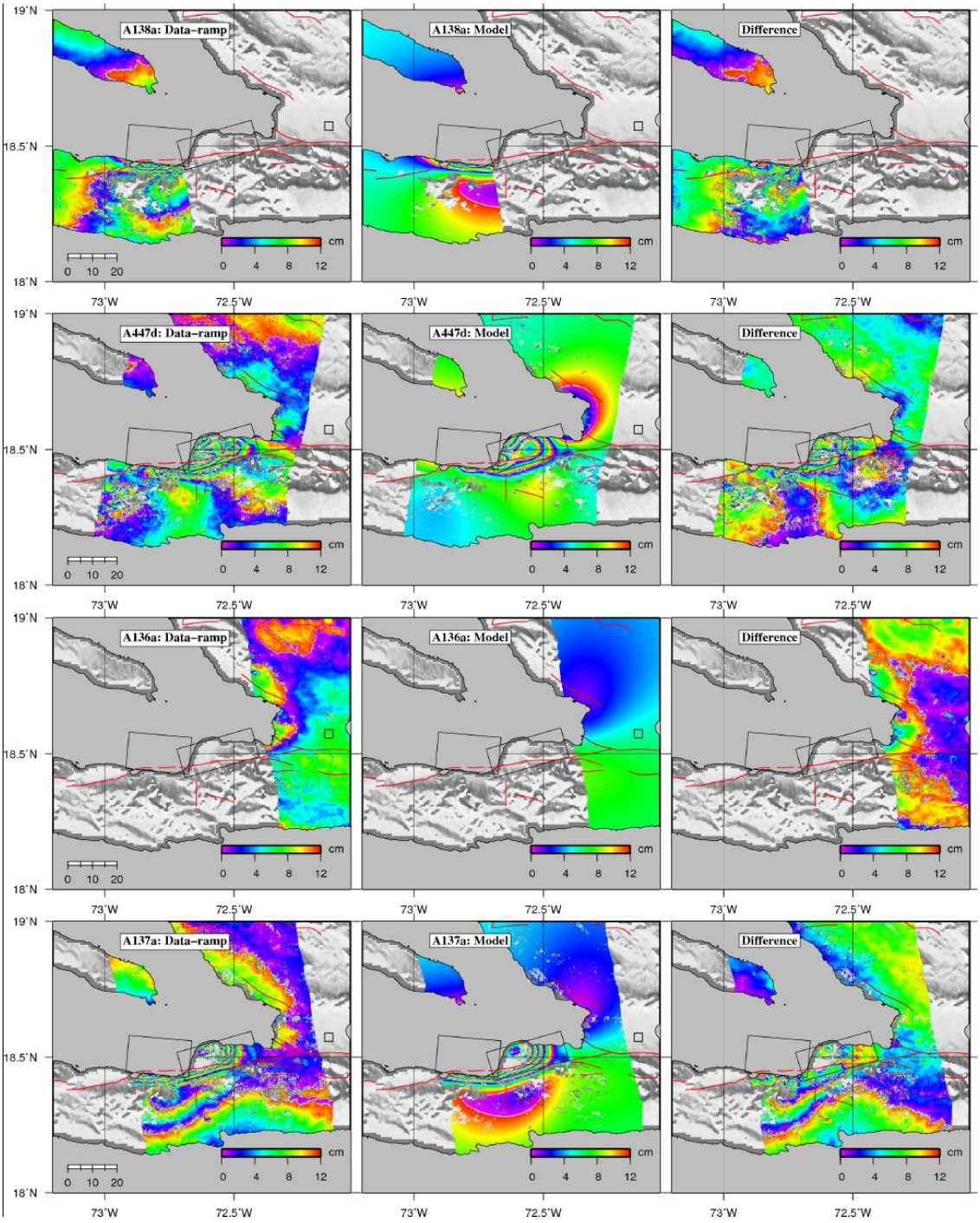

Figure D.4. Comparison of the wrapped InSAR images for the kinematic slip model. Each row is composed of the observed minus the ramp (left), predicted (middle) motion in the line-of-sight of the satellite, as well as the difference between the two (right). The satellite track number is indicated

in the top-right corner of the images with the last letter indicating whether this is an (a)scending or (d)escending track.

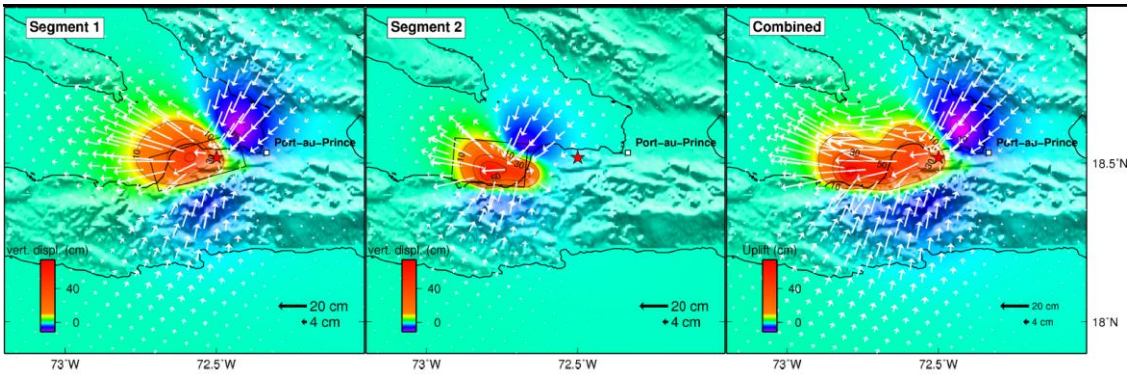

Figure D.5. Predicted surface deformation for the hypocenter segment (left), the second segment (middle) and both segments (right) corresponding to our preferred kinematic source model. Horizontal motion is indicated with arrows and vertical motion by the color scale.

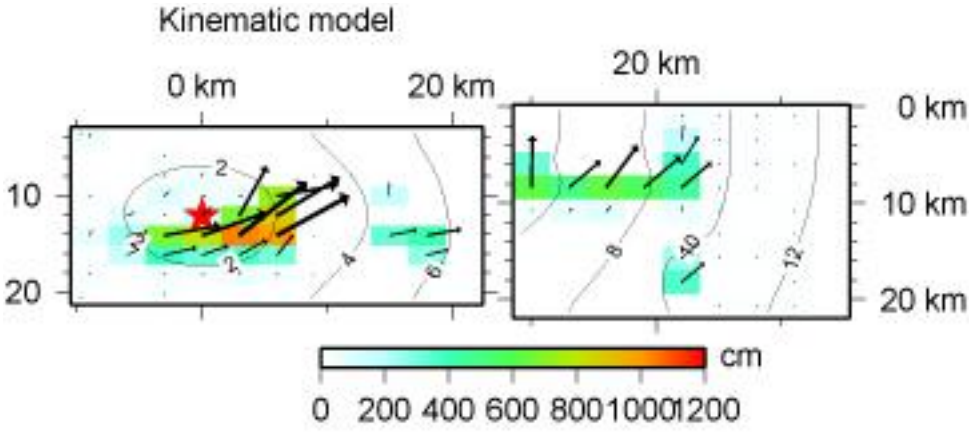

Figure D.6. Head-on view of the slip distribution for our preferred kinematic model. Color levels represent the amplitude of slip at each node of the fault model, the arrows the rake orientation, and the red star the hypocenter. The time evolution of slip is plotted as line contours every 2 seconds.

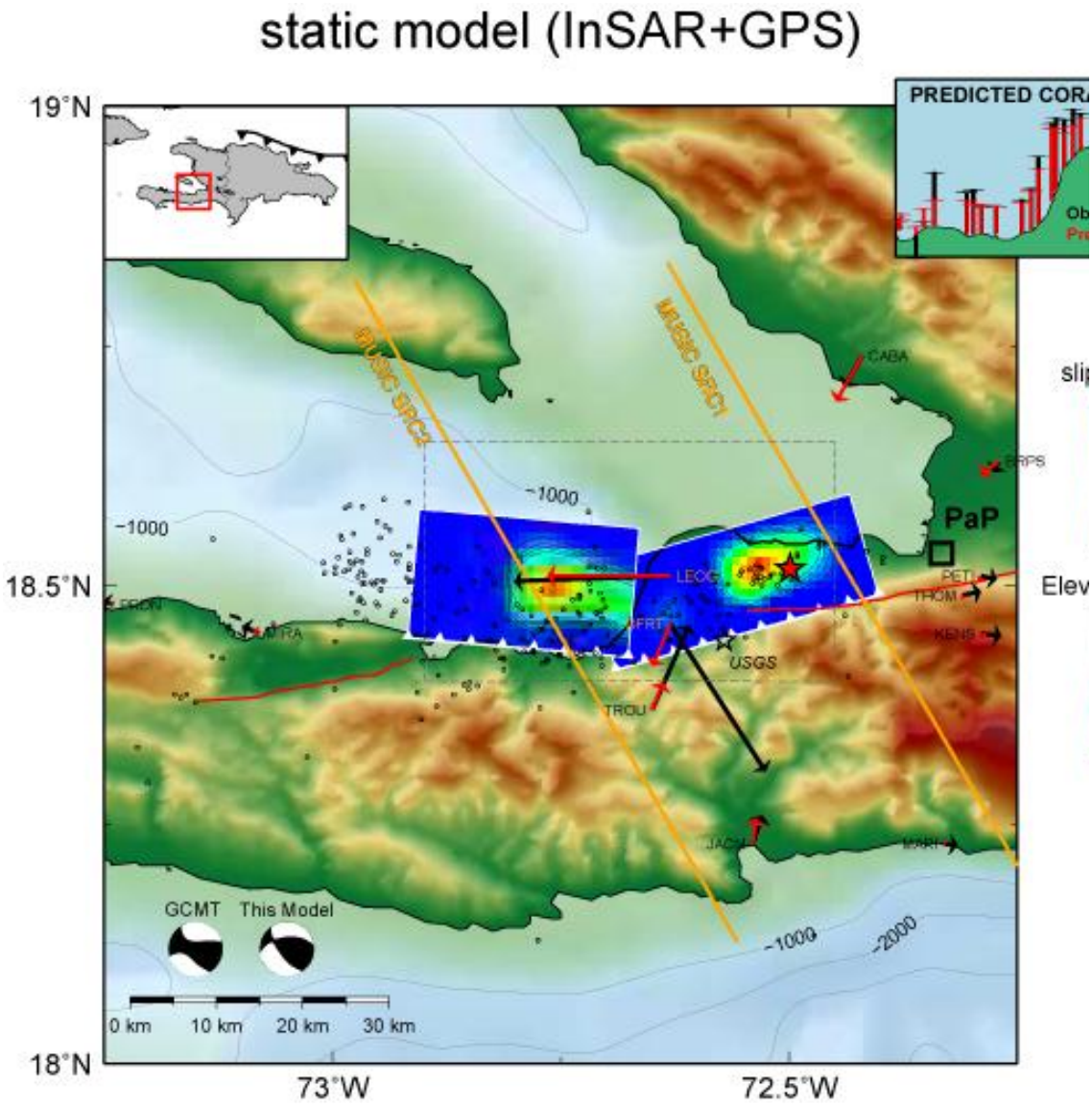

Figure D.7. Surface projection of the preferred static slip model (InSAR+GPS). The black and red arrows represent the recorded and model predicted campaign GPS vectors respectively. The two orange dashed lines mark the centroid locations of the subevents identified by MUSIC back-projection assuming our refined mainshock epicenter as reference (red star). The black empty star is the USGS epicenter. The small empty circles are the aftershock epicenters of the Haiti-OBS campaign. The two inset maps show the location of the study area (top left) and the measured (black) and predicted (red) coastal uplift (top right).

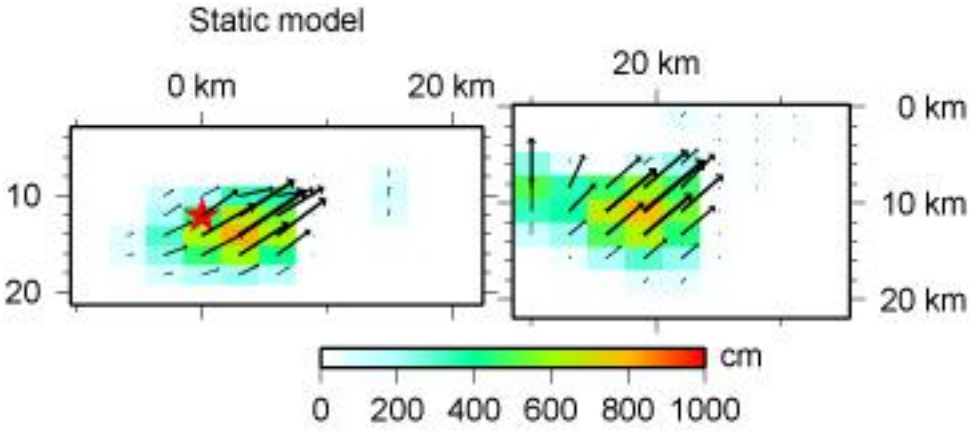

Figure D.8. Head-on view of the slip distribution for our preferred static slip model (InSAR+GPS). Color levels represent the amplitude of slip at each node of the fault model, the arrows the rake orientation, and the red star the hypocenter shown for reference.

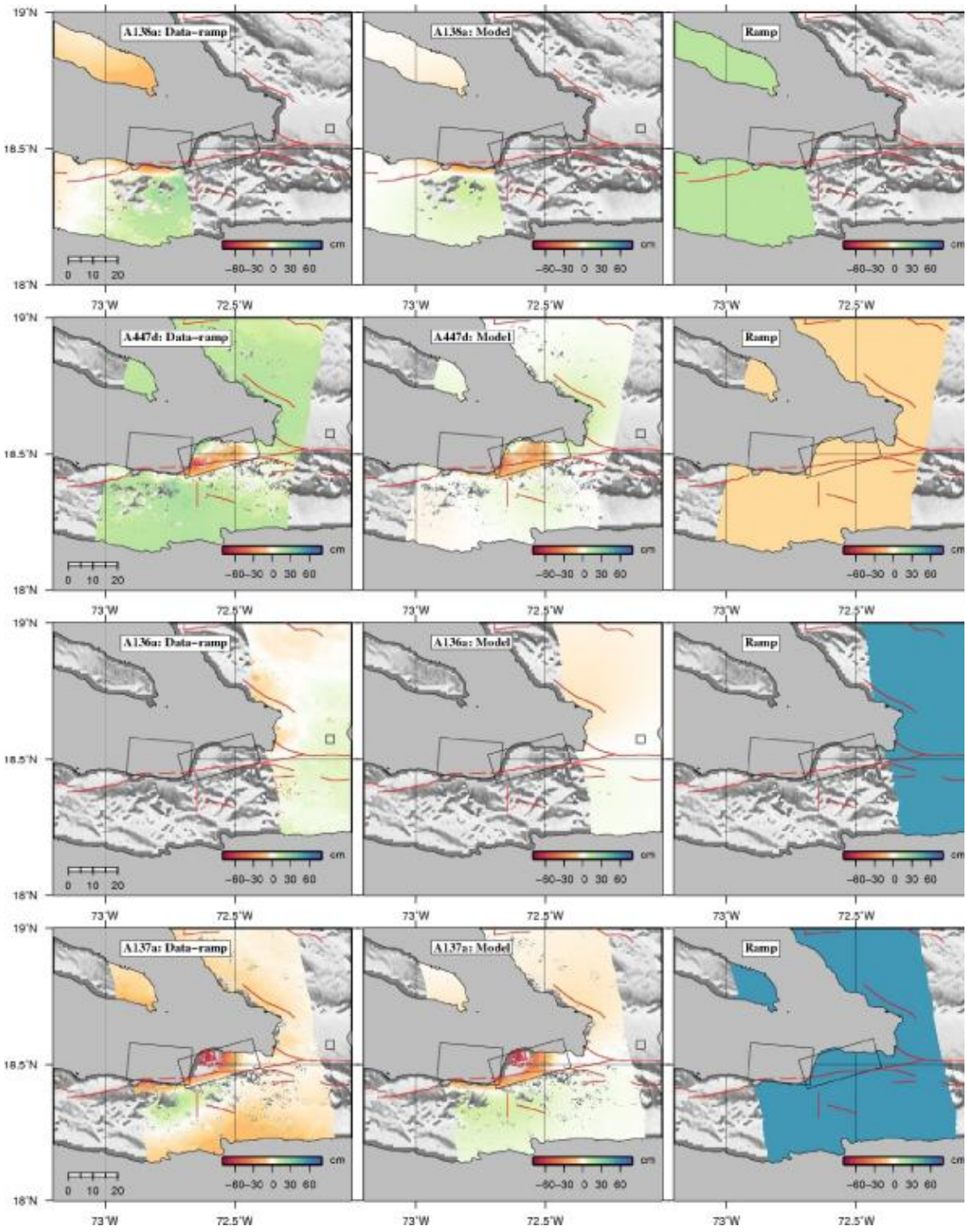

Figure D.9. Comparison of the unwrapped InSAR images for the static slip model. Each row is composed of the observed minus the ramp (left) and predicted (middle) motion in the line-of-sight of the satellite, and the amplitude of this constant ramp correction (right). The satellite track number

is indicated in the top-right corner of the images with the last letter indicating whether this is an (a)scending or (d)escending track.

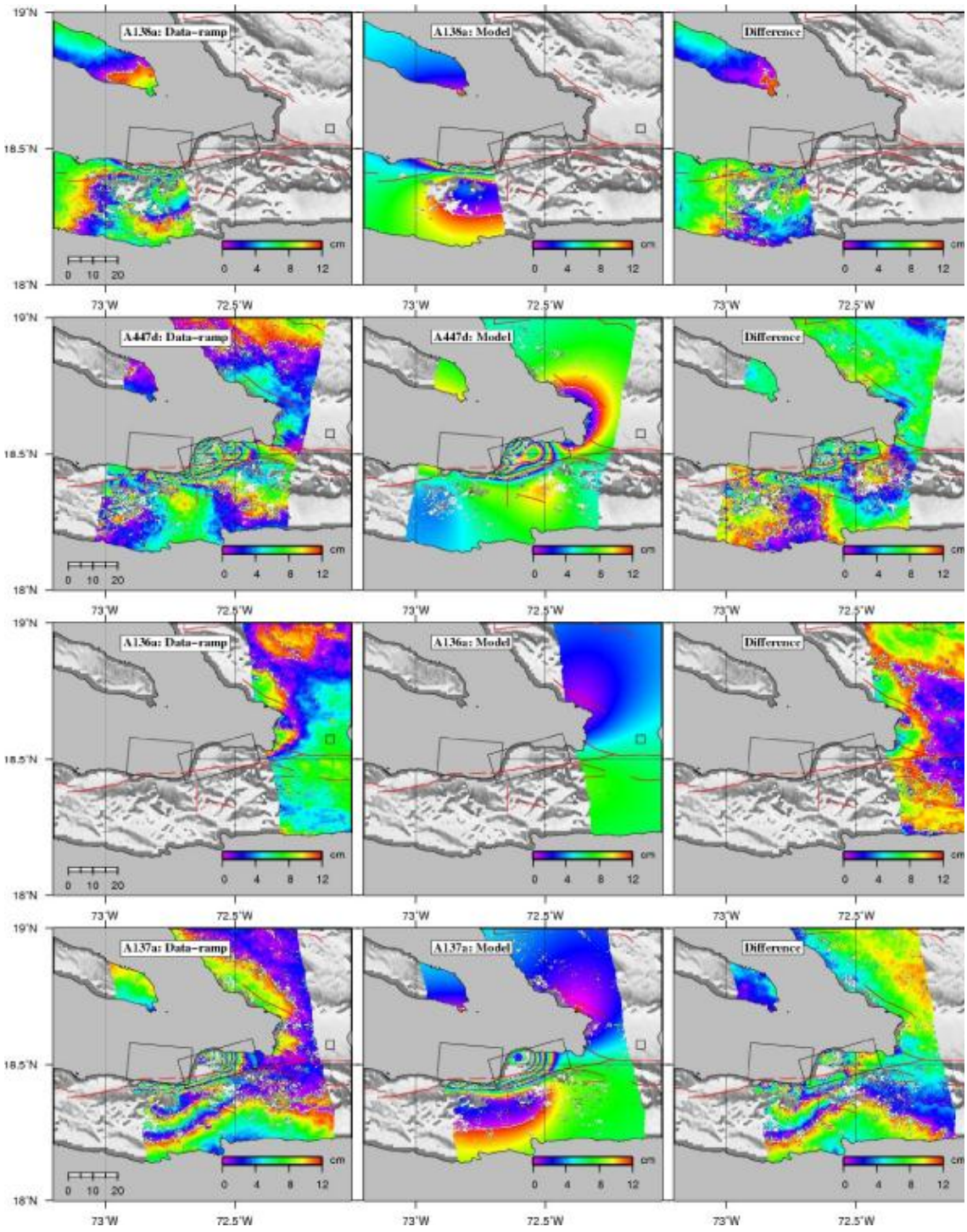

Figure D.10. Comparison of the wrapped InSAR images for the static slip model. Each row is composed of the observed minus the ramp (left), predicted (middle) motion in the line-of-sight of the satellite, as well as the difference between the two (right). The satellite track number is indicated in

the top-right corner of the images with the last letter indicating whether this is an (a)scending or (d)escending track.

	InSAR tracks				GPS data	Teleseismic data
	A136a	A137a	A138a	A447d		
Kinematic model	0.09	0.18	0.61	0.38	0.35	0.23
Static model	0.09	0.18	0.59	0.36	0.38	

Table D.1. Misfit of the kinematic and static slip models. Normalized root-mean-square values of the different datasets used to produce the kinematic and static slip models.

BIBLIOGRAPHY

Abercrombie, R. E., M. Antolik, and G. Ekström (2003), The June 2000 M_w 7.9 earthquakes south of Sumatra: Deformation in the India–Australia Plate, *J. Geophys. Res.*, *108*, 2018, doi:10.1029/2001JB000674.

Allmann, B. P., and P. M. Shearer (2009), Global variations of stress drop for moderate to large earthquakes, *J. Geophys. Res.*, *114*, B01310, doi:10.1029/2008JB005821.

Ampuero, J. P., and A. M. Rubin (2008), Earthquake nucleation on rate and state faults aging and slip laws, *J. Geophys. Res.*, *113*, B01302, doi:10.1029/2007JB005082.

Andrews, D. J. (2005), Rupture dynamics with energy loss outside the slip zone, *J. Geophys. Res.*, *110*, B01307, doi:10.1029/2004JB003191.

Antolik, M., A. Kaverina, and D. S. Dreger (2000), Compound rupture of the great 1998 Antarctic plate earthquake, *J. Geophys. Res.*, *105*(B10), 23,825–23,838, doi:10.1029/2000JB900246.

Asano, K., and T. Iwata (2011), Strong Ground Motion Generation during the 2011 Tohoku-Oki Earthquake, AGU abstract, U42A-03.

Bassin, C., G. Laske, and G. Masters (2000), The current limits of resolution for surface wave tomography in North America, *Eos Trans. AGU*, *81*(48), Fall Meet. Suppl., Abstract S12A-03.

Bernard, P., and R. Madariaga (1984a), A new asymptotic method for the modeling of near-field accelerograms, *Bull. Seismol. Soc. Am.*, *74*(2), 539–557.

Bernard, P., and R. Madariaga (1984b), High-frequency seismic radiation from a buried circular fault, *Geophys. J. R. Astron. Soc.*, *78*(1), 1–17, doi:10.1111/j.1365-246X.1984.tb06468.x.

Bhat, H. S., M. Olives, R. Dmowska, and J. R. Rice (2007), Role of fault branches in earthquake rupture dynamics, *J. Geophys. Res.*, *112*, B11309, doi:10.1029/2007JB005027.

Borcea, L., G. Papanicolaou, and C. Tsogka (2005), Interferometric array imaging in clutter, *Inverse Probl.*, *21*(4), 1419–1460, doi:10.1088/0266-5611/21/4/015.

Bouchon, M., H. Karabulut, M. Aktar, S. Ozalaybey, J. Schmittbuhl, and M. P. Bouin (2011), Extended nucleation of the 1999 M-w 7.6 Izmit earthquake, *Science*, *331*(6019), 877–880, doi:10.1126/science.1197341.

Calais, E., A. Freed, G. Mattioli, F. Amelung, S. Jonsson, P. Jansma, S. H. Hong, T. Dixon, C. Prepetit, and R. Momplaisir (2010), Transpressional rupture of an unmapped fault during the 2010 Haiti earthquake, *Nat. Geosci.*, *3*(11), 794–799, doi:10.1038/ngeo992.

Calais, E., Y. Mazabraud, B. M. de Lepinay, P. Mann, G. Mattioli, and P. Jansma (2002), Strain partitioning and fault slip rates in the northeastern Caribbean from GPS measurements, *Geophys. Res. Lett.*, *29*(18), 1856, doi:10.1029/2002GL015397.

Chandran, S. (2006), Advances in Direction-of-Arrival Estimation, Artech House.

Chlieh, M., Avouac, J.P., Hjorleifsdottir, V., Song, T-R.A., Ji, C., Sieh, K., Sladen, A., Hebert, H., Prawirodirdjo, L., Bock and Y., Galetzka, J. (2007), Coseismic slip and afterslip of the great Mw 9.15 Sumatra–Andaman earthquake of 2004, *Bulletin of the Seismological Society of America*, Vol. 97, No. 1A, pp. S152–S173, doi: 10.1785/0120050631.

Choy, G. L. and A. McGarr (2002), Strike-slip earthquakes in the oceanic lithosphere: observations of exceptionally high apparent stress. *Geophys. J. Int.* 150, 506.

Christensen, N. I. (2004), Serpentinites, peridotites, and seismology, *International Geology Review*, vol. 46, 795-816.

Chu, R., L. P. Zhu, and D. V. Helmberger (2009), Determination of earthquake focal depths and source time functions in central Asia using teleseismic *P* waveforms, *Geophys. Res. Lett.*, *36*, L17317, doi:10.1029/2009GL039494.

Cloetingh, S. and R. Wortel (1986), Stress in the Indo-Australian Plate. *Tectonophysics* 132, 49.

Cocco, M., and J. R. Rice (2002), Pore pressure and poroelasticity effects in Coulomb stress analysis of earthquake interactions, *J. Geophys. Res.*, 107, 2030, doi:10.1029/2000JB000138.

Delescluse, M., and N. Chamotrooke (2007), Instantaneous deformation and kinematics of the India-Australia Plate, *Geophys. J. Int.*, 168(2), 818-842.

Delescluse, M., and N. Chamot-Rooke (2008), Serpentinization pulse in the actively deforming Central Indian Basin, *Earth Planet Sci. Lett.*, 276(1-2), 140-151.

DeMets C., R. G. Gordon, D. F. Argus (2010), Geologically current plate motions. *Geophys. J. Int.* 181, 1.

Deplus, C., M. Diament, H. Habert, G. Bertrand, S. Dominguez, J. Dubois, P. Patriat, B. Pontoise, and J. J. Sibilla, (1998). Direct evidence of active deformation in the eastern Indian oceanic plate. *Geology* 26, 131.

Dieterich, J. H. (1992), Earthquake nucleation on faults with rate-dependent and state-dependent strength, *Tectonophysics*, *211*(1–4), 115–134, doi:10.1016/0040-1951(92)90055-B.

Dixon, T. H., F. Farina, C. DeMets, P. Jansma, P. Mann, and E. Calais (1998), Relative motion between the Caribbean and North American plates and related boundary zone deformation from a decade of GPS observations, *J. Geophys. Res.*, *103*(B7), 15,157–15,182, doi:10.1029/97JB03575.

Duan, B., and D. D. Oglesby (2007), Nonuniform prestress from prior earthquakes and the effect on dynamics of branched fault systems, *J. Geophys. Res.*, *112*, B05308, doi:10.1029/2006JB004443.

Duan, B. (2012), Dynamic rupture of the 2011 Mw 9.0 Tohoku-Oki earthquake: Roles of a possible subducting seamount, *J. Geophys. Res.*, *117*, B05311, doi:10.1029/2011JB009124.

Dunham, E. M., P. Favreau, and J. M. Carlson (2003), A supershear transition mechanism for cracks, *Science*, 299(5612), 1557-1559, doi:10.1126/science.1080650.

Duputel, Z., H. Kanamori, V. Tsai., L. Rivera., L. Meng., and J.-P. Ampuero (2012), The 2012 Sumatra great earthquake sequence, *Earth Plants Sc. Lett.*, in press.

Ellsworth, W. L., and G. C. Beroza (1995), Seismic evidence for an earthquake nucleation phase, *Science*, *268*(5212), 851–855, doi:10.1126/science.268.5212.851.

Engdahl, E. R., A. Villasenor, H. R. DeShon and C. H. Thurber (2007), Teleseismic relocation and assessment of seismicity (1918-2005) in the region of the 2004 Mw 9.0 Sumatra-Andaman and 2005 Mw 8.6 Nias Island great earthquakes. *B Seismol Soc Am* 97, S43.

England, P., and J. Jackson (2011), Uncharted seismic risk, *Nat. Geosci.*, *4*, 348–349, doi:10.1038/ngeo1168.

Escartin, J., G. Hirth, and B. Evans (2001), Strength of slightly serpentinized peridotites: Implications for the tectonics of oceanic lithosphere, *Geology*, 29(11), 1023-1026.

Fletcher, J. B., P. Spudich, and L. M. Baker (2006), Rupture propagation of the 2004 Parkfield, California, earthquake from observations at the UPSAR, *Bull. Seismol. Soc. Am.*, *96*(4B), S129–S142, doi:10.1785/0120050812.

Fliss, S., H. S. Bhat, R. Dmowska, and J. R. Rice (2005), Fault branching and rupture directivity,*J. Geophys. Res.*, *110*, B06312, doi:10.1029/2004JB003368.

Freund, L. B. (1998), *Dynamic Fracture Mechanics*, Cambridge University Press.

Goldstein, P., and R. J. Archuleta (1991), Deterministic frequency-wave-number methods and direct measurements of rupture propagation during earthquakes using a dense array: Theory and methods, *J. Geophys. Res.*, *96*(B4), 6173–6185, doi:10.1029/90JB02123.

Guilbert, J., J. Vergoz, E. Schissele, A. Roueff, and Y. Cansi (2005), Use of hydroacoustic and seismic arrays to observe rupture propagation and source extent of theM_w = 9.0 Sumatra earthquake, *Geophys. Res. Lett.*, *32*, L15310, doi:10.1029/2005GL022966.

Hashimoto, M., Y. Fukushima, and Y. Fukahata (2011), Fan-delta uplift and mountain subsidence during the Haiti 2010 earthquake, *Nat. Geosci.*, *4*(4), 255–259, doi:10.1038/ngeo1115.

Hayes, G. P., et al. (2010), Complex rupture during the 12 January 2010 Haiti earthquake, *Nat. Geosci.*, *3*(11), 800–805, doi:10.1038/ngeo977.

Helmberger, D. V. (1983), Theory and application of synthetic seismograms, in *Earthquakes: Observation, Theory and Interpretation*, pp. 174–222, Soc. Ital. di Fis, Bologna, Italy.

Hillers, G., Y. Ben-Zion, and P. M. Mai (2006), Seismicity on a fault controlled by rate- and state-dependent friction with spatial variations of the critical slip distance, *J. Geophys. Res.*, *111*, B01403, doi:10.1029/2005JB003859.

Horikawa, H. Earthquake doublet in Kagoshima, Japan (2001), Rupture of asperities in a stress shadow. *B. Seismol. Soc. Am.*, 91, 112.

Hoshiba, M., and I. Kazuhiro (2011), Initial 30 seconds of the 2011 off the Pacific coast Tohoku earthquake (Mw 9.0)-amplitude and τc for magnitude estimation for earthquake early warning, *Earth Planets Space*, doi:10.5047/eps.2011.06.015.

Huang, Y., L. Meng, and J.-P. Ampuero (2012), A Dynamic Model of the Frequency-Dependent Rupture Process of the 2011 Tohoku-Oki Earthquake, *Earth Planets Space* (speical issue on the Tohoku-Oki earthquake), in press.

Igarashi, T., T. Matsuzawa, N. Umino, and A. Hasegawa (2001), Spatial distribution of focal mechanisms for interplate and intraplate earthquakes associated with the subducting Pacific plate beneath the northeastern Japan arc: A triple-planed deep seismic zone, *J. Geophys. Res.*, *106*(B2), 2177–2191, doi:10.1029/2000JB900386.

Ide, S. Slip inversion (2009), *Treatise on Geophysics Volume 4: Earthquake Seismology*, Elsevier press.

Ide, S., A. Baltay, and G. Beroza (2011), Shallow dynamic overshoot and energetic deep rupture in the 2011 M_w 9.0 Tohoku-Oki earthquake, *Science*, *332*, 1426–1429.

Ishii, M., P. M. Shearer, H. Houston, and J. E. Vidale (2005), Extent, duration and speed of the 2004 Sumatra-Andaman earthquake imaged by the Hi-Net array, *Nature*,*435*(7044), 933–936.

Ishii, M., P. M. Shearer, H. Houston, and J. E. Vidale (2007), Teleseismic P wave imaging of the 26 December 2004 Sumatra-Andaman and 28 March 2005 Sumatra earthquake ruptures using the Hi-net array, *J. Geophys. Res.*,112(B11), Doi 10.1029/2006jb004700.

Ishii, M. (2011), High-frequency rupture properties of the M-w 9.0 off the Pacific coast of Tohoku Earthquake, Earth Planets Space, 63(7), 609-614.

Ito, Y., K. Obara, K. Shiomi, S. Sekine, and H. Hirose (2007), Slow earthquakes coincident with episodic tremors and slow slip events, *Science*, *315*(5811), 503–506, doi:10.1126/science.1134454.

Ji, C., D. J. Wald, and D. V. Helmberger (2002), Source description of the 1999 Hector Mine, California, earthquake, part I: Wavelet domain inversion theory and resolution analysis, *Bull. Seismol. Soc. Am.*, *92*(4), 1192–1207, doi:10.1785/0120000916.

Jung, H., H. W. Green, and L. F. Dobrzhinetskaya (2004), Intermediate-depth earthquake faulting by dehydration embrittlement with negative volume change, Nature, 428(6982), 545-549.

Kiser, E., & Ishii, M., (2011), The 2010 Mw 8.8 Chile earthquake: Triggering on multiple segments and frequency-dependent rupture behavior. *Geophys. Res. Lett.* 38, L07301, doi:10.1029/2011GL047140.

Kame, N., J. R. Rice, and R. Dmowska (2003), Effects of prestress state and rupture velocity on dynamic fault branching, *J. Geophys. Res.*, 108, 2265, doi:10.1029/2002JB002189.

Kato, N. (2007), How frictional properties lead to either rupture-front focusing or crack-like behavior, Bull. *Seismol. Soc. Am.*, 97, 2182-2189.

Kato, N., and S. Yoshida (2011), A shallow strong patch model for the 2011 great Tohoku-oki earthquake: A numerical simulation, *Geophys. Res. Lett.*, 38, L00G04, doi:10.1029/2011GL048565.

Kelemen, P. B., and G. Hirth (2007), A periodic shear-heating mechanism for intermediate-depth earthquakes in the mantle, *Nature*, 446(7137), 787-790.

Kennett, B. L. N., and E. R. Engdahl (1991), Traveltimes for global earthquake location and phase identification, *Geophys. J. Int.*, *105*(2), 429–465, doi:10.1111/j.1365-246X.1991.tb06724.x.

Kikuchi, M. (1975), Inelastic effect on crack propagation, *J. Phys. Earth*(23).

Kikuchi, M., and H. Kanamori (1982), Inversion of complex body waves, *Bull. Seismol. Soc. Am.*, *72*(2), 491–506.

Klingelhoefer, F., M.-A. Gutscher, S. Ladage, J.-X. Dessa, D. Graindorge, D. Franke, C. Andréé, H. Permana, T. Yudistira, and A. Chauhan (2010), Limits of the seismogenic zone in the epicentral region of the 26 December 2004 great Sumatra-Andaman earthquake: Results from seismic refraction and wide-angle reflection surveys and thermal modeling, *J. Geophys. Res.*, 115, B01304, doi:10.1029/2009JB006569.

Koketsu, K., et al. (2011), A unified source model for the 2011 Tohoku earthquake, *Earth Planet Sc. Lett*, 310(3-4), 480-487, Doi 10.1016/j.epsl.2011.09.009.

Koper, K. D., A. Hutko, T. Lay, C. J. Ammon, and H. Kanamori (2011), Frequency-dependent rupture process of the 2011 Mw 9.0 Tohoku earthquake: comparison of short-period P wave backprojection images and broadband seismic rupture models, Earth Planets Space, 63(7), 599-602, doi: 10.5047/eps.2011.05.026, 2011.

Koper, K. D., A. R. Hutko, and T. Lay (2011), Along-dip variation of teleseismic short-period radiation from the 11 March 2011 Tohoku earthquake (Mw 9.0), *Geophys. Res. Lett.*, 38, L21309, doi:10.1029/2011GL049689.

Koper, K. D., A. R. Hutko, T. Lay, and O. Sufri (2012), Imaging short-period seismic radiation from the 27 February 2010 Chile (MW 8.8) earthquake by back-projection of P, PP, and PKIKP waves, *J. Geophys. Res.*, 117, B02308, doi:10.1029/2011JB008576.

Kozdon, J., and E. Dunham (2012), Rupture to the trench: Dynamic rupture simulations of the 11 March 2011 Tohoku earthquake, *B. Seismol. Soc. Am.*, submitted.

Krim, H., and M. Viberg (1996), Two decades of array signal processing research: The parametric approach, *IEEE Signal Process Mag.*, *13*(4), 67–94, doi:10.1109/79.526899.

Lapusta, N., and J. R. Rice (2003), Nucleation and early seismic propagation of small and large events in a crustal earthquake model, *J. Geophys. Res.*, *108*(B4), 2205, doi:10.1029/2001JB000793.

Lawson, C. L., and R. J. Hanson (1974), *Solving Least Squares Problems*, Prentice Hall, Englewood Cliffs, N. J.

Lay, T., C. J. Ammon, H. Kanamori, K. D. Koper, O. Sufri, and A. R. Hutko (2010), Teleseismic inversion for rupture process of the 27 February 2010 Chile (Mw 8.8) earthquake, *Geophys. Res. Lett.*, 37, L13301, doi:10.1029/2010GL043379.

Lay, T., C. J. Ammon, H. Kanamori, M. J. Kim and L. Xue (2011), Outer trench-slope faulting and the 2011 M(w) 9.0 off the Pacific coast of Tohoku Earthquake. *Earth Planets Space* 63, 713.

Lay, T., H. Kanamori, C. J. Ammon, K. D. Koper, A. R. Hutko, L. Ye, H. Yue, and T. M. Rushing (2012), Depth-varying rupture properties of subduction zone megathrust faults, J. Geophys. Res., 117, B04311, doi:10.1029/2011JB009133.

Lee, S. J., B. S. Huang, M. Ando, H. C. Chiu, and J. H. Wang (2011), Evidence of large scale repeating slip during the 2011 Tohoku-Oki earthquake, Geophys Res Lett, 38, doi 10.1029/2011gl049580.

Leonard, M. (2010), Earthquake Fault Scaling: Self-Consistent Relating of Rupture Length, Width, Average Displacement, and Moment Release, B. Seismol. Soc. Am., 100(5A), 1971-1988.

Ma, S. (2012), A self-consistent mechanism for slow dynamic deformation and tsunami generation for earthquakes in the shallow subduction zone, *Geophys. Res. Lett.*, 39, L11310, doi:10.1029/2012GL051854.

Madariaga, R. (1977), High-frequency radiation from crack (stress drop) models of earthquake faulting, *Geophys. J. R. Astron. Soc.*, *51*(3), 625–651, doi:10.1111/j.1365-246X.1977.tb04211.x.

Madariaga, R. (1983), High-frequency radiation from dynamic earthquake fault models,*Ann. Geophys.*, *1*(1), 17–23.

McGuire, J., and G. C. Beroza (2012), A Rogue Earthquake Off Sumatra, *Science*, 336(6085).

McHugh, C. M., et al. (2011), Offshore sedimentary effects of the 12 January 2010 Haiti earthquake, *Geology*, *39*(8), 723–726, doi:10.1130/G31815.1.

Mendoza, C. (2005), Earthquake source-parameter estimation using regional waveforms: Implications for tsunami alerting in the Caribbean, *Geophys. Res. Lett.*, *32*, L24314, doi:10.1029/2005GL024435.

Meng, L., and J. P. Ampuero (2012), Slow rupture and weakly pressure-sensitive strength enables compressional branching: Dynamic rupture simulations of the 2012 Off-Sumatra earthquake. In preparation.

Meng, L., J. P. Ampuero, Y. Luo, W. Wu, S. Ni (2012), Mitigating Artifacts in Back-Projection Source Imaging with Implications on Frequency-Dependent Properties of the Tohoku-Oki Earthquake. *Earth, Planets and Space*, 10.5047/eps.2012.05.010.

Meng, L., J.-P. Ampuero, A. Sladen, and H. Rendon (2012), High-resolution backprojection at regional distance: Application to the HaitiM7.0 earthquake and comparisons with finite source studies, *J. Geophys. Res.*, 117, B04313, doi:10.1029/2011JB008702.

Meng, L., J. P. Ampuero, J. Stock, Z. Duputel, Y. Luo, and V. C. Tsai (2012), An earthquake in a maze: compressional rupture branching during the 11 April 2012 M8.6 off-Sumatra earthquake, Science, In press.

Meng, L., A. Inbal, and J.-P. Ampuero (2011), A window into the complexity of the dynamic rupture of the 2011 Mw 9 Tohoku-Oki earthquake, *Geophys. Res. Lett.*, 38, L00G07, doi:10.1029/2011GL048118.

Mercier de L épinay, B., et al. (2011), The 2010 Haiti earthquake: A complex fault pattern constrained by seismologic and tectonic observations, *Geophys. Res. Lett.*, *38*, L22305, doi:10.1029/2011GL049799.

Mestre, X., B. A. Johnson, and Y. I. Abramovich (2007), Source power estimation for array processing applications under low sample size constraints, *Int. Conf. Acoust. Spee.*, 897-900

Miura, S., N. Takahashi, A. Nakanishi, T. Tsuru, K. S., and Y. Kaneda (2005), Structural characteristics off Miyagi forearc region, the Japan Trench seismogenic zone, deduced from a wide-angle reflection and refraction study, *Tectonophysics*, 407, 165-188.

Miyake, H., Y. Yokota, H. Si, and K. Koketsu (2011), Earthquake Scenarios Generating Extreme Ground Motions: Application to the 2011 Tohoku Earthquake, AGU abstract, S 52B-07.

Mori, J. (2011), The Great 2011 Tohoku, Japan Earthquake (Mw9.0): An Unexpected Event, Southern California Earthquake Center Annual Meeting, Special Invited Talk.

Nakahara, H. (2008), Seismogram envelope inversion for high-frequency seismic energy radiation from moderate-to-large earthquakes, *Adv. Geophys.*, *50*, 401–426, doi:10.1016/S0065-2687(08)00015-0.

Nettles, M., and V. Hjorleifsdottir (2010), Earthquake source parameters for the 2010 January Haiti main shock and aftershock sequence, *Geophys. J. Int.*, *183*(1), 375–380, doi:10.1111/j.1365-246X.2010.04732.x.

Nielsen, S., J. Taddeucci, and S. Vinciguerra (2010), Experimental observation of stick-slip instability fronts, *Geophys. J. Int.*, *180*(2), 697–702, doi:10.1111/j.1365-246X.2009.04444.x.

Oglesby, D. D. (2005), The dynamics of strike-slip step-overs with linking dip-slip faults, *B Seismol. Soc. Am*, 95(5), 1604-1622.

Ohnaka, M., and Y. Kuwahara (1990), Characteristic features of local breakdown near a crack-tip in the transition zone from nucleation to unstable rupture during stick-slip shear failure, *Tectonophysics*, *175*(1–3), 197–220, doi:10.1016/0040-1951(90)90138-X.

Okubo, P. G., and J. H. Dieterich (1984), Effects of physical fault properties on frictional instabilities produced on simulated faults, *J. Geophys. Res.*, *89*(B7), 5817–5827.

Ozawa, S., T. Nishimura, H. Suito, T. Kobayashi, M. Tobita, and T. Imakiire (2011), Coseismic and postseismic slip of the 2011 magnitude-9 Tohoku-Oki earthquake, *Nature*, 475(7356), 373-U123.

Paterson, M. S., and T.-F. Wong (2005), Experimental Rock Deformation - The Brittle Field, Springer.

Perfettini, H., J.P. Avouac, H. Tavera, A. Kositsky, J.M. Nocquet, F. Bondoux, M. Chlieh, A. Sladen, L. Audin, D.L. Farber, and P. Soler (2010), Seismic and aseismic slip on the Central Peru megathrust, *Nature*, 465, doi:10.1038/nature09062.

Poliakov, A. N. B., R. Dmowska, and J. R. Rice (2002), Dynamic shear rupture interactions with fault bends and off-axis secondary faulting, *J. Geophys. Res.*, 107, 2295, doi:10.1029/2001JB000572.

Prentice, C. S., P. Mann, A. J. Crone, R. D. Gold, K. W. Hudnut, R. W. Briggs, R. D. Koehler, and P. Jean (2010), Seismic hazard of the Enriquillo-Plantain Garden fault in Haiti inferred from palaeoseismology, *Nat. Geosci.*, *3*(11), 789–793, doi:10.1038/ngeo991.

Pulido, N., and L. A. Dalguer (2009), Estimation of the high-frequency radiation of the 2000 Tottori (Japan) earthquake based on a dynamic model of fault rupture: Application to the strong ground motion simulation, *Bull. Seismol. Soc. Am.*, *99*(4), 2305–2322, doi:10.1785/0120080165.

Ripperger, J., P. M. Mai and J.-P. Ampuero (2008),Variability of near-field ground motion from dynamic earthquake rupture simulations, Bull. Seism. Soc. Am., 98 (3), 1207-1228; doi:10.1785/0120070076

Robinson, D. P., C. Henry, S. Das, and J. H. Woodhouse (2001), Simultaneous rupture along two conjugate planes of the Wharton Basin earthquake. *Science* 292, 1145.

Rollins, J. C., and R. S. Stein (2010), Coulomb stress interactions among $M \geq 5.9$ earthquakes in the Gorda deformation zone and on the Mendocino Fault Zone, Cascadia subduction zone, and northern San Andreas Fault, *J. Geophys. Res.*, *115*, B12306, doi:10.1029/2009JB007117.

Rosakis, A. J. (2002), Intersonic shear cracks and fault ruptures, *Adv. Phys.*, *51*(4), 1189–1257, doi:10.1080/00018730210122328.

Rost, S., and C. Thomas (2002), Array seismology: Methods and applications, *Rev. Geophys.*, *40*(3), 1008, doi:10.1029/2000RG000100.

Roten, D., H. Miyake, and K. Koketsu (2011), A Rayleigh wave back-projection method applied to the 2011 Tohoku earthquake, *Geophys Res Lett*, Doi:10.1029/2011GL050183.

Sager, W. W., C. F. Paul, K. S. Krishna, M. Pringle, A. E. Eisin, F. A. Frey, D. Gopala Rao, and O. Levchenko (2010), Large fault fabric of the Ninetyeast Ridge implies near-spreading ridge formation, *Geophys. Res. Lett.*, *37*, L17304, doi:10.1029/2010GL044347.

Sato, H., and M. C. Fehler (1998), *Seismic Wave Propagation and Scattering in the Heterogeneous Earth*, Springer-Verlag and American Institute of Physics Press.

Sato, M., T. Ishikawa, N. Ujihara, S. Yoshida, M. Fujita, M. Mochizuki, and A. Asada (2011), Displacement Above the Hypocenter of the 2011 Tohoku-Oki Earthquake, *Science*, 332(6036), 1395-1395, DOI 10.1126/science.1207401.

Satriano, C., E. Kiraly, P. Bernard, and J.-P. Vilotte (2012), The 2012 Mw 8.6 Sumatra earthquake: evidence of westward sequential seismic ruptures associated to the reactivation of a N-S ocean fabric, *Geophys. Res. Lett.*, doi:10.1029/2012GL052387, in press.

Schmidt, R. O. (1986), Multiple Emitter Location and Signal Parameter-Estimation, *IEEE Trans. Antennas Propag.*, *34*(3), 276–280, doi:10.1109/TAP.1986.1143830.

Shao, G., X. Li, C. Ji, and T. Maeda (2011), Focal mechanism and slip history of the 2011 Mw 9.1 off the Pacific coast of Tohoku Earthquake, constrained with teleseismic body and surface waves, Earth Planets Space, 63(7), 559-564, doi: 10.5047/eps.2011.06.028, 2011.

Shibazaki, B., Y. Yoshida, M. Nakamura, M. Nakamura, and H. Katao (2002), Rupture nucleations in the 1995 Hyogo-ken Nanbu earthquake and its large aftershocks, *Geophys. J. Int.*, *149*(3), 572–588, doi:10.1046/j.1365-246X.2002.01601.x.

Simons, M., et al. (2011), The 2011 magnitude 9.0 Tohoku-Oki Earthquake: Mosaicking the megathrust from seconds to centuries, *Science*, *332*, 1421–1425, doi:10.1126 science.1206731.

Snoke, J. A. (2009), Traveltime tables for *iasp91* and *ak135*, *Seismol. Res. Lett.*, *80*(2), 260–262, doi:10.1785/gssrl.80.2.260.

Spudich, P., and E. Cranswick (1984), Direct observation of rupture propagation during the 1979 Imperial Valley earthquake using a short baseline accelerometer array, *Bull. Seismol. Soc. Am.*, *74*(6), 2083–2114.

Spudich, P., and L. N. Frazer (1984), Use of ray theory to calculate high-frequency radiation from earthquake sources having spatially-variable rupture velocity and stress drop,*Bull. Seismol. Soc. Am.*, *74*(6), 2061–2082.

Therrien C.W. (1992), *Discrete Random Signals and Statistical Signal Processing*, Englewood Cliffs, NJ: PrenticeHall

Takahashi, N., S. Kodaira, T. Tsuru, J. O. Park, Y. Kaneda, K. Suyehiro, H. Kinoshita, S. Abe, M. Nishino, and R. Hino (2004), Seismic structure and seismogenesis off Sanriku region, northeastern Japan, *Geophys. J. Int.*, *159*(1), 129–145, doi:10.1111/j.1365-246X.2004.02350.x.

Tanioka, Y. and K. Satake (1996), Tsunami generation by horizontal displacement of ocean bottom, *Geophys. Res. Lett.*, *23*(8), 861–864, doi:10.1029/96GL00736.

Thomson, D. J. (1982), Spectrum estimation and harmonic-analysis, *Proc. IEEE*, *70*(9), 1055–1096, doi:10.1109/PROC.1982.12433.

Tromp, J., D. Komatitsch, and Q. Y. Liu (2008), Spectral-element and adjoint methods in seismology, *Commun. Comput. Phys.*, *3*(1), 1–32.

Uchide, T., and S. Ide (2007), Development of multiscale slip inversion method and its application to the 2004 mid-Niigata Prefecture earthquake, *J. Geophys. Res.*, *112*, B06313, doi:10.1029/2006JB004528.

Ulmer, P., and V. Trommsdorff (1995), Serpentine stability to mantle depths and subduction-related magmatism, *Science*, 268(5212), 858-861.

Vallée, M., M. Landes, N. M. Shapiro, and Y. Klinger (2008), The 14 November 2001 Kokoxili (Tibet) earthquake: High-frequency seismic radiation originating from the transitions between sub-Rayleigh and supershear rupture velocity regimes, *J. Geophys. Res.*, *113*, B07305, doi:10.1029/2007JB005520.

Vandecar, J. C., and R. S. Crosson (1990), Determination of teleseismic relative phase arrival times using multi-channel cross-correlation and least-squares, *Bull. Seismol. Soc. Am.*, *80*(1), 150–169.

Viesca, R. C., E. L. Templeton, and J. R. Rice (2008), Off-fault plasticity and earthquake rupture dynamics: 2. Effects of fluid saturation, *J. Geophys. Res.*, 113, B09307, doi:10.1029/2007JB005530.

Walker, K. T., and P. Shearer (2009), Illuminating the near-sonic rupture velocities of the intracontinental Kokoxili Mw 7.8 and Denali Mw 7.9 strike-slip earthquakes with global P-wave back projection imaging, *J. Geophys. Res.*, 114, doi:10.1029/2008JB005738.

Wang, D., and J. Mori (2011), Rupture process of the 2011 off the Pacific coast of Tohoku earthquake (Mw 9.0) as imaged with back-projection of teleseismic P-waves, *Earth Planets Space*, 63(7), 603-607, Doi: 10.5047/eps.2011.05.029.

Wei, S., Graves, R., Helmberger, D., Avouac, J. P., Jiang, J. (2012), Sources of shaking and flooding during the Tohoku-Oki earthquake: A mixture of rupture styles, *Earth and Planetary Science Letters*, 333–334, 91–100.

Wei, S., Z. Zhan, Y. Luo, S. Ni, Y. Chen, and D. V. Helmberger (2009), Rapid regional centroid solutions, *Eos Trans. AGU*, *90*(52), Fall Meet. Suppl., Abstract S13A-1734.

Wells, D. L., and K. J. Coppersmith (1994), New empirical relationships among magnitude, rupture length, rupture width, rupture area, and surface displacement, *Bull. Seismol. Soc. Am.*, *84*(4), 974–1002.

Wesnousky, S. G. Predicting the endpoints of earthquake ruptures. *Nature*, 444, 358 (2006).

Wesnousky, S. G., and G. P. Biasi (2011), The length to which an earthquake will go to rupture, B Seismol. Soc. Am., 101(4), 1948-1950.

Wiens, D. A. and S. Stein (1983), Age dependence of oceanic intraplate seismicity and implications for lithospheric evolution. *J. Geophys. Res.* 88, (B8), 6455.

Xu, Y., K. D. Koper, O. Sufri, and L. Zhu (2009), Rupture imaging of the Mw 7.9 12 May 2008 Wenchuan earthquake from back projection of teleseismic P waves, *Geochemistry Geophysics Geosystems*, 10, Q04006, Doi:10.1029/2008GC002335.

Yao, H. J., P. Gerstoft, P. M. Shearer, and C. Mecklenbrauker (2011), Compressive sensing of the Tohoku-Oki Mw 9.0 earthquake: Frequency-dependent rupture modes, *Geophys Res Lett*, 38, Doi 10.1029/2011gl049223.

Yao, H. J., P. Shearer, and P. Gerstoft (2012), Subevent location and rupture imaging using iterative backprojection for the 2011 Tohoku Mw 9.0 earthquake, *Geophys J Int*, in press.

Yue, H., and T. Lay (2011), Inversion of high-rate (1 sps) GPS data for rupture process of the 11 March 2011 Tohoku earthquake (M(w) 9.1), *Geophys Res Lett*, 38, Doi 10.1029/2011gl048700.

Zerva, A., and V. Zervas (2002), Spatial variation of seismic ground motions, Applied *Mechanics Reviews*, 55(3), 271-297.

Zhang, H., Z. Ge and L. Ding (2011), Three sub-events composing the 2011 off the Pacific coast of Tohoku Earthquake (Mw 9.0) inferred from rupture imaging by back-projecting teleseismic P waves, *Earth Planets Space*, Vol. 63 (No. 7), pp. 595-598.

Zhu, L. P., and D. V. Helmberger (1996), Advancement in source estimation techniques using broadband regional seismograms, *Bull. Seismol. Soc. Am.*, *86*(5), 1634–1641.

Zhu, L. P., and L. A. Rivera (2002), A note on the dynamic and static displacements from a point source in multilayered media, *Geophys. J. Int.*, *148*(3), 619–627, doi:10.1046/j.1365-246X.2002.01610.x.